UNIVERSITY OF CALIFORNIA, SAN DIEGO

Inhibitory Circuits of the Cortex:

Control of Rhythmic and Stimulus Evoked Activity

A dissertation submitted in partial satisfaction of the

requirements for the degree Doctor of Philosophy

in

Neurosciences
with a Specialization in Computational Neurosciences

by

Bassam V. Atallah

Committee in charge:

Professor Massimo Scanziani, Chair
Professor Edward M. Callaway
Professor Jeffry S. Isaacson
Professor William B. Kristan Jr.
Professor Roberto Malinow

2011

The Dissertation of Bassam V. Atallah is approved, and it is acceptable in quality and form for publication on microfilm and electronically:

_____

_____

_____

_____

_____

Chair

University of California, San Diego

2011

Table of Contents

List of Figures

Chapter 1

Chapter 2

Chapter 3

Chapter 4

Acknowledgments

My deepest gratitude goes to:

Massimo Scanziani for being a conscientious articulate mentor, leading by example, keeping a constant positive outlook, treating me as an equal partner in science, providing endless inspiration and enthusiasm, tirelessly push himself and me to overachieve, while still being a thoughtful friend.

Jeffry Isaacson for his generosity, wisdom and encouragement as a second advisor and wonderful friend.

Lindsey Glickfeld for brightening-up the lab, being a constant intellectual stimulus, and an example of an excellent electrophysiologist.

Hillel Adesnik for encouragement, selflessly sharing knowledge and demonstrating a fearless approach to science.

Shawn Olsen for support, and providing an example of practical, organized, efficient scientific approach.

All the members of the Isaacson and Scanziani labs past and present for making it a joy for me to be in lab.

Cindy Poo for delicious lab snacks, endless emotional sustenance, patience, and love, and exemplifying an excellent experimentalist.

Chapter one contains reprinted material as it appears Input normalization by global feedforward inhibition expands cortical dynamic range Pouille F, Marin-Burgin A, Adesnik H, Atallah BV, Scanziani M, Nat Neurosci. 2009

Dec;12(12):1577-85. The dissertation author was an author for this material contributing analysis and designed the model. Experiments were performed by authors F. Pouille, A. Marin-Burgin and H. Adesnik. Permission reprint of material is granted by all original authors.

Chapter two contains reprinted material as it appears Supralinear increase of recurrent inhibition during sparse activity in the somatosensory cortex, Kapfer C, Glickfeld LL, Atallah BV & Scanziani M, Nature Neuroscience 2007 Jun;10(6), 743 - 753 . The dissertation author was an author for this material performing analysis and designing the model. Experiments were performed by authors C Kapfer, L L Glickfeld, & M Scanziani. Permission reprint of material is granted by all original authors.

Chapter three is a reprint of the material as it appears in Instantaneous modulation of gamma oscillation frequency by balancing excitation with inhibition. Atallah BV, Scanziani M, Neuron. 2009 May 28;62(4):566-77. The dissertation author was the primary author of this material.

Chapter four consists of material in preparation for publication. All experiments and analysis were performed by the dissertation author.

Vita

2000 B.S., Physics, B.A. Mathematics Hope College, Holland, MI

2000-04 Junior Research Scientist, Princeton Optronics, Princeton, NJ

2011 Ph.D., Neurosciences, Univ. of California, San Diego, La Jolla, CA

Publications

Atallah B, Scanziani M, The impact of parvalbumin expressing interneurons on visual processing *(2011, In Preparation)*

Pouille F, Marin-Burgin A, Adesnik H, **Atallah B**, Scanziani M, Input normalization by global feedforward inhibition expands cortical dynamic range. *Nat Neurosci*. 2009 Dec. 12(12):1577-85

Atallah B, Scanziani M, Instantaneous modulation of gamma oscillation frequency by balancing excitation and inhibition *Neuron* 2009 May 28. 62(4):566-77

Glickfeld LL, **Atallah B**, Scanziani M, Complementary modulation of somatic inhibition by opioids and cannabinoids, *J. Neurosci*, 2008 20; 28(8):1824-32

Kapfer C, **Atallah B**, Glickfeld LL, Scanziani M, Supralinear Increase in Recurrent Inhibition during Sparse Activity in the Somatosensory Cortex. *Nat Neurosci*. 2007 Jun 10(6), 743 - 753

Awards

2010 Leon Thal Award for Excellence in Graduate Research

2008-10 Ruth L. Kirschstein National Research Service Award (NRSA), NIMH

2004-06 NSF Fellowship

ABSTRACT OF THE DISSERTATION

Inhibitory Circuits of the Cortex:

Control of Rhythmic and Stimulus Evoked Activity

by

Bassam V. Atallah

Doctor of Philosophy in Neurosciences

with a Specialization in Computational Neurosciences

University of California, San Diego, 2011

Professor Massimo Scanziani, Chair

We are surrounded by a world, which makes sense, only because we make sense of it. At every instant in our waking life we estimate the state of the world based on sensory data, then we reshape the world to meet our goals. How are these sensations encoded, goals represented and action computed? To answer these questions we dissect the biological circuitry in our brains that seamlessly performs these computations.

To study the dynamics of neural circuits, we specifically focus on the role inhibition in shaping signal processing. This work examines how inhibitory circuits process increasingly complex forms of afferent input:

First, we characterize and model local circuit responses to brief impulses of afferent activity. We find that local circuits generate feedforward inhibition in

the first few milliseconds after an afferent impulse. This inhibition adjusts the excitability of the local population normalizing it to the afferent excitation level. Then, in the next few milliseconds, as individual local pyramidal cells spike they immediately recruit a distinct recurrent inhibitory circuit. This feedback circuit is extremely sensitive responding with negative feedback when even a single local pyramidal cell is active. By modeling the circuit dynamics during these stages in cortical processing we quantitatively demonstrate that the feedforward and feedback inhibitory circuits are tuned to be both sensitive to sparse activity and yet maintain fidelity with which a cortical circuit represents inputs at high activity levels.

Next, the role inhibition during spontaneous rhythmic activity is dissected. Our results demonstrate that by rapidly balancing excitation with inhibition, cortical networks can swiftly modulate rhythms over a wide band of frequencies.

Finally, we investigate the role of a distinct type of inhibitory interneuron during the first stage of cortical visual processing. Using optogenetics to either enhance or suppress parvalbumin positive interneurons spiking, we demonstrate that these neurons play a key role in modulating the selectivity of responses in primary visual cortex.

Together, these results demonstrate the multifaceted role inhibitory circuits play in signal processing and shaping cortical computation; adding to our communal effort to develop a complete picture of how neural circuitry performs computations and encodes sensation.

Introduction

From the moment we are born, before we can coordinate our hands, eyes, tongue, or even synthesize permanent memories, our brain is hard at work setting the ground work for us to learn and function as intelligent beings. What explains the unique human capacity for complexity, abstraction and reasoning.

We are privileged in that we are no longer constrained to speculate as to the nature of thought. Instead we can use psychophysics and electrophysiology to quantify our behavior and neural activity. This enables us to apply the same methods of scientific reductionism that have been fruitful in the physical sciences. An initial goal of this approach is to identify the basic *neural modules* that together coordinate these complex computations.

What are the modules of neural computation?

Consider man-made computers, arguably the brain's closest relative in terms of complexity and function, for an analogy. A modern PC consists of computational modules on several different scales. On the largest scale, there are specific processors tackling problems like graphics and sound. Similarly, we know that in the brain, both cortex and subcortical areas are segregated into modality specific regions such as vision or audition (Jasper and Penfield 1954).

On an intermediate scale, computer processors are made up from logic gates (*computational modules* that perform basic operations such as NOT, AND, NAND, etc) that are repeated identically no matter whether they are part of a graphics or sound processor. At the finest scale these computational modules are all built from the same basic components: transistors, resistors and capacitors.

It has been suggest that the brain also consists of repeated modular-like stuctures of "columns" (Mountcastle, 1978, Mountcastle, 1997). This is because, the functional properties of within the cortex change depending on a neuron's position on the rostral-caudal or medial-lateral axes, but these properties are largely conserved independent of a neuron's depth along the radial axis within the cortex. Anatomical and developmental data appear to support the idea that neurons along this "column" or radial axis may have a unique relationship (Rakic, 1971). However, the precise definition of columns and whether they are distinct *computational modules* remains unclear. This is because, while much is known about the cellular and synaptic nature of the brain's basic components: neurons[1], we have a poor understanding of the intermediate scale, at the circuit level, i.e. between a functional column and a neuron, where neurons operate as groups.

[1] Though subcellular compartments are certainly important for neuronal computation (London & Häusser 2005).

Since bridging this gaping hole in our knowledge of neural computation is crucial, we chose to study how circuits process signals and perform computations.

Inhibitory circuits

A critical part of neural circuitry are GABAergic inhibitory interneurons. Inhibitory function within the nervous system was first described by Sherrington (Sherrington et al 1906), as part of muscle contraction. It was his student John Eccles however, who first recorded intracellularly from motor neurons and observed inhibitory post-synaptic potentials (Brock et al 1952). In a subsequent set of experiments, he established that inhibition was caused by a specific set of cells that ubiquitously inhibited their targets (and not by differential action of the same axons on different postsynaptic targets) (Bradley et al 1953). In the next two decades, GABA and glycine were established as the inhibitory neurotransmitters (Krnjevic et al 1967, Curtis et al 1968). This work established the existence of inhibitory neurons, and that they are distinct from their excitatory counter parts.

GABAergic interneurons make up a major portion of all neurons in the brain (20-30%). Inhibitory synaptic transmission is crucial for healthy neurophysiology and information processing. Since cortical circuits are recurrent, imbalances between excitation and inhibition, even if small, can result in aberrant cortical activity. In fact, disruptions of this balance results in sedated states when inhibition is pharmacologically enhanced and epileptic states when

inhibition is reduced pathophysiologically (Traub & Wong 1982, Prince 1978, Miles & Wong 1987).

Maintaining the balance of excitation and inhibition is a dynamic process. Levels of excitation in cortical networks change as a function of both the state of the extrinsic sensory world and the intrinsic state of cortical excitability. Variations in the nature of sensory stimuli are accompanied by large changes in the amount of both excitation and inhibition received by neurons. Studies quantifying this balance suggest that changes in synaptic excitation are often accompanied by changes in synaptic inhibition (Wehr & Zador 2003, Wilent & Contreras 2004, Anderson et al 2000). Together, these two conductances determine the computations performed by cortical neurons. In sensory cortices, for example, this precise balance defines the receptive-fields of neurons (Dykes et al 1984, Kyriazi et al 1996, Rao et al 2000, also see chapter 4).

Overview

In the following four chapters, we describe how inhibitory circuits dynamically balance excitation:

Chapter one is the product of a collaboration: Frédéric Pouille and Antonia Marin-Burgin show experimentally that the excitability of a local cortical network is almost instantaneously normalized to the strength of afferent input by feedforward inhibition. I designed a model to test whether this normalization quantitatively determines how the local network of principal cells is recruited by afferent input. Together we demonstrate that this normalization plays a crucial

role in expanding the range of afferent input a neural population can faithfully represent.

Chapter two focuses on what happens after principal cells in a local population are recruited. We address how many local principal neurons must be active to recruit feedback inhibition. In this collaboration, Christoph Kapfer found that feedback inhibition is recruited by the spiking of just one or two principal neurons. Using a model, I demonstrate that the distribution of excitatory input amplitudes onto inhibitory neurons is critical for setting sensitivity and dynamic range of the recurrent inhibitory circuit. Both the sensitivity and the wide dynamic range depend on the shape of the excitatory postsynaptic potentials (EPSPs) distribution onto inhibitory neurons. The few large-amplitude EPSPs ensure that even the activity of a single pyramidal cell will activate a fraction of the interneuron population, thus providing sensitivity to the circuit. On the other hand, a small the EPSP distribution's low average insures that the recruitment of inhibition does not saturate, but can reliably counters excitation if pyramidal cell activity increases.

In the third chapter we focus on the role of inhibition during fast rhythmic activity, a ubiquitous feature of neural activity. Here we use a combination of *in vivo, in vitro* electrophysiology and modeling to demonstrate that inhibition instantaneously balances excitation and plays a key role in determining the precise frequency of each oscillation cycle.

Finally, in the last chapter, we determine the impact inhibition has in shaping sensory responses in primary visual cortex. Here, we use optogenetics

to inactivate or activate a specific sub-type of interneuron, perisomatic targeting, parvalbumin expressing cells, during visual processing. We find that the inhibition evoked by these neurons plays a key role in determining the selectivity of principal neurons for orientation and direction.

Together, our data reveal the multifaceted role inhibitory circuits play in shaping cortical computation by regulating gain, imposing synchrony and modulating sensory encoding. In addition to demonstrating specific functions for neural circuits, our work illustrates the progress that can be made by systematically dissecting functional modules in the brain.

References

1. Anderson, J. S., Carandini, M. & Ferster, D. Orientation tuning of input conductance, excitation, and inhibition in cat primary visual cortex. J Neurophysiol 84, 926 (2000).

2. Bradley K, Easton DM, Eccles JC. An investigation of primary or direct inhibition, J Physiol. 1953 Dec 29;122(3):474-88.

3. Brock LG, Coombs JS, & Eccles JC, The recording of potentials from motoneurones with an intracellular electrode, J. Physiol. (Lond.) 117 (1952), pp. 431–460.

4. Curtis D.R., Hosli L., Johnston G.A. A pharmacological study of the depression of spinal neurones by glycine and related amino acids. Exp. Brain Res. 1968

5. Dykes, R. W., Landry, P., Metherate, R. & Hicks, T. P. Functional role of GABA in cat primary somatosensory cortex: shaping receptive fields of cortical neurons. J Neurophysiol 52, 1093 (1984).

6. Krnjevic K., Schwartz S. The action of γ-aminobutyric acid on cortical neurones. Exp. Brain Res. 1967; 3:320–326

7. Kyriazi, H. T., Carvell, G. E., Brumberg, J. C. & Simons, D. J. Quantitative effects of GABA and bicuculline methiodide on receptive field properties of neurons in real and simulated whisker barrels. J Neurophysiol 75, 560 (1996).

8. London M & Häusser M, Dendritic computation.. Annu Rev Neurosci. 2005; 28:503-32.

9. Miles, R. & Wong, R. K. Latent synaptic pathways revealed after tetanic stimulation in the hippocampus. Nature 329, 726 (1987).

10. Mountcastle VB, An organizing principle for cerebral function: the unit model and the distributed system, In The Mindful Brain,1978

11. Mountcastle VB, The columnar organization of the neocortex. Brain. 1997 Apr; 120 (Pt 4):701-22.

12. Penfield & Jasper. Epilepsy and the Functional Anatomy of the Human Brain,1954

13. Prince, D. A. Neurophysiology of epilepsy. Annu Rev Neurosci 1, 415 (1978).

14. Rakic P. , Guidance of neurons migrating to the fetal monkey neocortex. Brain Res. 1971 Oct 29;33(2):471-6.

15. Rao, S. G., Williams, G. V. & Goldman-Rakic, P. S. Destruction and creation of spatial tuning by disinhibition: GABA(A) blockade of prefrontal cortical neurons engaged by working memory. J Neurosci 20, 494 (2000)

16. Sherrington,The Integrative Action of the Nervous System, 1906

17. Traub, R. & Wong, R. Cellular mechanism of neuronal synchronization in epilepsy. Science 216, 747 (1982).

18. Wehr, M. & Zador, A. Balanced inhibition underlies tuning and sharpens spike timing in auditory cortex. Nature 426, 446 (2003).

19. Wilent, W. B. & Contreras, D. Synaptic responses to whisker deflections in rat barrel cortex as a function of cortical layer and stimulus intensity. J Neurosci 24, 3998 (2004).

Chapter 1. Input normalization by global feedforward inhibition expands cortical dynamic range

Abstract

The cortex is sensitive to weak stimuli, but responds to stronger inputs without saturating. The mechanisms that enable this wide range of operation are not fully understood. We found that the amplitude of excitatory synaptic currents necessary to fire rodent pyramidal cells, the threshold excitatory current, increased with stimulus strength. Consequently, the relative contribution of individual afferents in firing a neuron was inversely proportional to the total number of active afferents. Feedforward inhibition, acting homogeneously across pyramidal cells, ensured that threshold excitatory currents increased with stimulus strength. A simple model quantitatively demonstrates that this increase in threshold as a function of stimulus strength is a mechanism that expands the range of afferent input strengths that neuronal populations can represent.

Introduction

A characteristic of cortical excitatory neurons is their widely divergent axonal projection. This property enables cortical neurons to contact a large number of postsynaptic cells and allows each postsynaptic cell to receive inputs from many presynaptic neurons. In a circuit constructed with this excitatory divergence alone, the number of active presynaptic neurons (input strength)

that is sufficient to recruit all neurons in the postsynaptic population is only slightly larger than the input strength required to recruit any postsynaptic neuron at all. In other words, the input range that can be faithfully represented by the postsynaptic population is restricted. For example, if presynaptic neurons connect to a postsynaptic population with a probability of 15% (Lefort et al, 2009) and each postsynaptic cell requires 40 active inputs to be recruited (Otmakhov et al 1993), then 2% of the postsynaptic cells would be recruited by the activity of 200 presynaptic neurons and almost all (>99%) would be recruited by simply doubling the number of active presynaptic neurons (as determined by binomial statistics). Thus, in the absence of control mechanisms, small fluctuations in the fraction of presynaptically active neurons results in all-or-none recruitment of the postsynaptic population (Marr et al 1969, Vogels & Abbott 2005, Shadlen and Newsome 1998, Diesmann et al 1999) (this all-or-none behavior is qualitatively similar for a wide range of connectivity values and number of inputs necessary to reach threshold). However, both spontaneous and sensory-evoked cortical activity involves large fluctuations in the fraction of active neurons (for example, refs.7,8,9). What mechanisms does the cortex use to expand the range of input strengths over which it faithfully responds? One could imagine at least two distinct mechanisms. Reducing the gain of individual neurons (that is, the change in spiking probability as a function of input strength) would allow each neuron in the population to respond over a wider range of input strengths; this gain modulation could be achieved through GABAAreceptor–mediated conductances (Shu et al 2003, Mitchell & Silver

2003, Chance et al 2002, Carvalho & Buonomano 2009). Alternatively, staggering the recruitment of individual neurons over a wide range of input strengths would allow the population as a whole, rather than individual neurons, to represent a wider input range. This could be achieved by varying the amplitude of the excitatory postsynaptic currents (EPSCs) necessary to reach threshold for spike generation as a function of input strength.

We found that hippocampal and neocortical feedforward inhibitory circuits staggered the recruitment of individual pyramidal cells over a wide range of input strengths. Feedforward inhibition (FFI) acted homogeneously across the postsynaptic population of pyramidal cells to rapidly adjust their excitability to the strength of incoming presynaptic activity. As a result, the amplitude of the EPSC necessary for a pyramidal cell to reach spike threshold was dynamic and varied with the strength of the input. Heterogeneities in the amplitudes of EPSCs across the postsynaptic population determined the specific subset of pyramidal cells that would spike in response to the presynaptic input. A quantitative model of pyramidal cell recruitment demonstrates that this coordinated action of direct excitation and FFI(by effectively increasing distance from spike threshold) , enable the neuron population to remain sensitive to weak inputs, but not saturate in response to stronger activity.

Results

EPSC necessary to spike pyramidal cell is dynamic

We established the range of stimulus strengths over which the CA1 pyramidal cell population responds, that is, the dynamic range. We recorded from individual pyramidal cells in the loose-patch configuration and stimulated Schaffer collaterals over a range of intensities, from those that failed to trigger any spike to those that triggered spikes on every trial (Fig. 1.1a). The relationship between spiking probability of individual pyramidal cells and input strength (input strength is proportional to the number of activated Schaffer collateral; for details see Experimental Procedures and Appendix) was fitted with a sigmoid to interpolate the threshold input strength, where pyramidal cells spiked in 50% of the trials (Fig. 1.1a). The cumulative distribution of threshold input strengths for all recorded pyramidal cells (n = 39) represents the fractional recruitment of the CA1 pyramidal cell population, or activation curve (Fig. 1.1a). The dynamic range of the pyramidal cell population (that is, the ratio of the input strength necessary to activate 95% versus 5% of the pyramidal cell population) was approximately 34 (Fig. 1.1a), meaning that the pyramidal cell population can differentially represent a 34-fold increase in the number of active Schaffer collateral inputs before saturating. This is much larger than the dynamic range of an individual pyramidal cell (1.6 ± 0.7, n = 37; Fig. 1.1a; invariant between pyramidal cells recruited at different input strengths, $R^2 = 0.034$, $P = 0.27$) and is the result of staggered recruitment of CA1 pyramidal cells over a wide range of stimulus strengths (Fig. 1.1a).

Why are some pyramidal cells recruited at low input strength, whereas others require much stronger stimuli? We compared the excitatory postsynaptic

conductance (EPSG) evoked at threshold input strength (Otmakhov et al 1993) of pyramidal cells recruited over the range of input strengths (EPSGT refers to the EPSG evoked at threshold). Figure 1b illustrates an example of two pyramidal cells, simultaneously recorded in the loose-patch configuration, that required different stimulus strengths to spike. Whole-cell, voltage-clamp recording from the same two cells showed that the EPSGT in the pyramidal cell recruited by the stronger stimulus was much larger than in the pyramidal cell recruited with weaker stimulus (Fig. 1.1b). Over all of the experiments, we observed a steep increase in EPSGTs with increasing input strength (0.3-nS increase per percentile input strength, n = 32, P = 0.0024; Fig. 1.1b).

Are differences in EPSGT amplitudes the results of variability in intrinsic pyramidal cell properties? Input resistance, membrane time constant, resting potential and threshold potential did not significantly differ between pyramidal cells recruited at different input strengths. To further rule out the influence of intrinsic variability between pyramidal cells, we compared EPSGTs between two independent Schaffer collateral inputs converging onto a single pyramidal cell (Fig. 1.1c). EPSGTs were uncorrelated between the two inputs (Fig. 1.1c). Furthermore, in an individual pyramidal cell, the EPSGT evoked by the stronger input was invariably larger than the EPSGT evoked by the weaker input (1.5 ± 0.2–fold larger; P = 0.002, n = 19; Fig. 1.1c). Finally, there was no significant difference in the rise and decay kinetics of EPSGTs evoked by the weak and strong inputs

The increase in EPSGT implies that the contribution of each individual afferent in firing the neuron decreases with increasing input strength. By how much does this decrease? Over the range of input strengths from 0 to 0.5, the amplitude of the EPSGT increased approximately linearly (Fig. 1.1b; see model below) such that

$$EPSG_{\mathrm{TN}} = Nk + EPSG_{\mathrm{T0}}$$

where N is the number of active afferents, EPSGTN is the EPSGT when Nafferents are active, EPSGT0 is the EPSG necessary to reach threshold at minimal input strength (under our condition, it was ~ 6 nS; Fig. 1.1b) and kis the proportionality factor. Given g, the synaptic conductance produced by an individual afferent, the relative contribution of each afferent toward firing a cell, $\left(\frac{g}{EPSG_{\mathrm{TN}}}\right)$, is $\frac{g}{(Nk + EPSG_{\mathrm{T0}})}$. Thus, the relative contribution of individual afferents in firing a cell is normalized by the number of active afferents.

FFI expands population's dynamic range

What determines the amplitude of the EPSGT and why does it vary with input strength? Stimulation of Schaffer collaterals triggers powerful FFI in CA1 pyramidal cells through the recruitment of GABAergic interneurons (Pouille & Scanziani 2001, Buzsáki 1984, Alger & Nicoll 1982). There was a strong correlation between the amplitude of the EPSGT and the amplitude of the concomitantly triggered feedforward inhibitory postsynaptic conductance (IPSG; Fig. 1.2a; see Experimental Procedures). Furthermore, consistent with the

correlation between EPSGT and input strength (Fig. 1.1b), FFI increased with input strength, before saturating at input values above 0.5 (Fig. 1.2a). These data suggest that EPSGT may vary with input strength because of a parallel increase of FFI. We directly tested this possibility by either abolishing GABAergic transmission or by imposing a fixed amount of inhibition (Fig. 1.2b). Abolishing FFI with the GABAA receptor antagonist gabazine eliminated the increase in EPSGT with input strength (nonsignificant increase of 0.07 nS per percentile input strength, n = 30, P= 0.22; Fig. 1.2b), demonstrating a crucial role of GABAA receptors.

Model

Is the observed change in EPSGT sufficient to account for the expansion of the range of inputs the pyramidal cell population responds to? We created a simple quantitative model of Schaffer collateral excitation onto a population of CA1 pyramidal cells (Fig. 1.3; see Experimental Procedures). Schaffer collateral inputs contacted pyramidal cells with a probability of 0.06 (Sayer et al 1990). We computed the fraction of recruited pyramidal cells as a function of the number of stimulated Schaffer collateral and compared the resulting activation curves under two conditions: with either a fixed or a dynamic EPSGT (Fig. 1.3a). The threshold to recruit a pyramidal cell was set at 100 Schaffer collateral inputs2 and remained constant in the fixed EPSGT condition. In the dynamic EPSGT condition, the number of Schaffer collaterals necessary to recruit a pyramidal cell increased linearly with increasing number of stimulated Schaffer

collaterals, up to approximately threefold, and then remained constant to simulate experimental observation (Fig. 1.3b). The exact increment of the modeled dynamic EPSGT was chosen to yield an activation curve that best approximated the experimentally observed activation curve (Fig. 1.3c). With a fixed EPSGT, the activation curve was steep and had a narrow dynamic range (Fig. 1.3c). With a dynamic EPSGT, on the other hand, the activation curve had an onset similar to the fixed threshold activation curve, but rose much less steeply, resulting in a wider dynamic range (Fig. 1.3c; the sensitivity of the slope of the activation curve to the rate of increase of the dynamic EPSGT is illustrated in Fig. 1.4).

The dynamic EPSGT activation curve (Fig. 1.3c) is the synthesis of a family of fixed EPSGT activation curves, each having progressively larger EPSGT (a subset are illustrated in Fig. 1.3c). An intersection occurs at the specific input strength at which dynamic and fixed EPSGT activation curves have equal EPSGT.

This simple model captures the basic experimental finding, namely that the dynamic EPSGT expands the range of inputs that the CA1 pyramidal cell population responds to by maintaining sensitivity to weak inputs and preventing saturation to stronger stimuli. It should be noted, however, that the modeled fixed and dynamic EPSGT activation curves both fail to fully account for the experimentally observed activation curves, where more than ~ 80% of pyramidal cells are active (see Discussion).

Discussion

Our data suggest that the EPSC amplitude necessary to reach spike threshold in hippocampal and neocortical pyramidal cells is dynamic and increases when the number of active neurons in the presynaptic layer increases. Accordingly, the fractional contribution of an individual afferent input in firing a neuron is not fixed, but instead is continuously normalized by the total number of active afferents. Through this simple mechanism, the pyramidal cell population can smoothly operate over a wide range of stimulus strengths. This mechanism is probably important for enabling cortical structures such as the hippocampus to be responsive to weak stimuli, but remain sparsely active even when confronted with stronger inputs. Although FFI sets a global threshold for recruitment of pyramidal cells, local differences in afferent excitation determine which pyramidal cell is recruited.

The fraction of neurons active at any given moment in cortical areas strongly fluctuates as a result of either varying sensory stimuli or ongoing intrinsic activity. Activity levels in the hippocampus can vary from sparse activity in the exploring animal8 to synchronous activation of a large fraction of neurons during ripples (Csicsvari et al 2000). As a consequence, downstream targets of these neuronal populations experiences substantial fluctuations in the fraction of afferents that are active at any given time point. The connectivity patterns of cortical excitatory projections, however, are ill-suited to allow postsynaptic populations of neurons to operate over a wide range of afferent activity5; afferent axons typically form very divergent projections to contact a large

number of postsynaptic targets through relatively weak contacts, such that the simultaneous activity of several afferents is necessary to recruit a target neuron (Otmakhov et al 1993, Bruno & Sakmann 2006). Because of this divergence, gradual increases in the number of active afferents produce very steep, or explosive, increases in the fraction of recruited targets5, resulting in a limited range of input strengths that can be differentially represented by the postsynaptic population.

Our data indicate that cortical circuits expand the range of afferent input strengths that the cells can respond to by ensuring that, when the input is strong, pyramidal cells necessitate larger EPSCs to reach thresholds. The dynamic range of the population is several-fold wider than the dynamic range of an individual pyramidal cell (34 versus 2). Neither the dynamic range nor the gain (slope of the sigmoidal fit, $R2 = 0.046$, $P = 0.2$) of individual pyramidal cells varied between pyramidal cells recruited along the entire input range. Thus, although GABAA receptor–mediated conductances can regulate the gain of individual neurons (Shu et al 2003, Mitchell & Silver 2003, Chance et al 2002) our data suggest that pyramidal cell populations can function over a wide range of afferent intensities without requiring gain changes in individual neurons.

Individual excitatory afferent inputs to cortical areas diverge to contact fast-spiking basket cells and principal neurons. Only those pyramidal cells that received large enough EPSCs to overcome the concomitantly occurring inhibition reached spike threshold. With increasing stimulus strength, the amplitude of FFI increased (Fig. 1.2a) and larger EPSCs became necessary for

pyramidal cells to reach spike threshold. The onset of inhibition before spike generation in pyramidal cells also means that this early phase of inhibition is unlikely to be of feedback origin, as feedback inhibition is a consequence of pyramidal cell spiking. The control of the amplitude of the EPSC necessary to reach threshold by FFI is likely to be even more marked in response to repetitive, burst-like14or asynchronous afferent activity, as a result of the large temporal overlap between afferent excitation and FFI generated by the previous stimulus.

Our model captures the initial 80% of the activation curve; that is, until the EPSGT plateaus above input strength of ~ 0.5. At these greater input strengths, the EPSGT is fixed and the model predicts that the activation curve behaves accordingly. However, the top 20% of the experimentally determined activation curve extends beyond this prediction. It is possible that the observed onset of the plateau is inaccurate because of an error in measurement (for example, the lack of proper voltage clamp) and that the real EPSGT continues to grow with increasing input strength. Alternatively, a small portion of pyramidal cells may receive Schaffer collateral inputs with very low probability as compared with the rest of the population (resulting from heterogeneity in the population or damage to their dendrites) such that they necessitate a much larger stimulus strength to be recruited. Our model also illustrates the fact that the activation curve is sensitive to how steeply the EPSGT varies with input strength. Because the increase in EPSGT is, at least in part, determined by the increase in FFI, any parameter that controls the excitability of GABAergic

interneurons, such as neuromodulators, will probably affect the slope of the activation curve, and thus the range of input strength that can be represented by the postsynaptic pyramidal cell population.

The model also illustrates that the trajectory activation curve is sensitive to the precise manner in which EPSGT evolves as a function of input strength. If EPSGT plateaus at a lower input strength then the activation curve saturates soon. If, on the other hand, EPSGT plateaus at higher input strength the slope of the activation curve will be decreased and hence the dynamic range substantially increased. So FFI may play a crucial role in shaping the precise transformation of input into activation of pyramidal cell population. Furthermore, our model indicates that subtle changes in EPSGT as a function of input strength result in substantial reshaping of pyramidal cell activation (Fig 4). Thus, the exact balance feed-forward excitation and inhibition is likely tightly regulated in order to maintain the precise transformation of input into pyramidal cell output.

In summary, because the EPSGT is controlled in a feedforward manner, the sensitivity of pyramidal cells is virtually instantaneously adjusted to match the strength of the afferent stimulus. This instantaneous adjustment differs from adaptation because it does not rely on the previous history of the network through a negative feedback mechanism, such as feedback inhibition, spike adaptation, synaptic depression or presynaptic inhibition. The presence of feedforward inhibitory circuits along several major excitatory pathways in the brain suggests that the expansion of the dynamic range by instantaneously

varying the amplitude of the EPSC necessary to reach threshold may not be unique to hippocampus cortex.

Experimental Procedures

Slice preparation.

Acute hippocampal slices (400 m) were prepared from 4–5-week-old male Wistar rats and incubated for 45 min in an interface chamber at 34 °C in normal artificial cerebrospinal fluid (ACSF) containing 119 mM NaCl, 2.5 mM KCl, 1.3 mM NaH2PO4, 1.3 mM MgCl2, 2.5 mM CaCl2, 26 mM NaHCO3 and 11 mM glucose (equilibrated with 95% O2 and 5% CO2). The slices were kept at room temperature (20–25 °C) for 0 to 6 h before being placed in a submerged chamber for recording at 31–33 °C.

Coronal slices (400 m) from somatosensory cortex were prepared from postnatal day 15–25 ICR white mice in modified ACSF containing 83 mM NaCl, 2.5 mM KCl, 1.0 mM NaH2PO4, 3.3 mM MgSO4, 0.5 mM CaCl2, 26.2 mM NaHCO3, 72 mM sucrose and 22 mM glucose (equilibrated with 95% O2 and 5% CO2). The slices were incubated for 45 min in a submerged chamber at 34 °C containing the modified ACSF and kept in the same chamber at room temperature (20–25 °C) for 0 to 6 h before being placed in a recording chamber with normal ACSF at 31–33 °C.

Electrophysiology and analysis.

Recorded neurons were visually identified using infrared differential interference contrast videomicroscopy. Unless stated otherwise, all whole-cell recordings were performed with patch pipettes (2–4 M) filled with 150 mM potassium gluconate, 1.5 mM MgCl2, 5 mM HEPES buffer, 1.1 mM EGTA and 10 mM phosphocreatine (pH = 7.25, 280–290 mOsm); biocytin (0.2% wt/vol) and 2 mM Mg-ATP were added in the recording solution for interneurons. When recording with a cesium-based intracellular solution, the composition was 115 mM cesium methanesulphonate, 8 mM NaCl, 10 mM HEPES, 0.3 mM Na3-GTP, 4 mM Mg-ATP, 0.3 mM EGTA, 5 mM QX-314-Cl and 10 mM BAPTA tetracesium (pH = 7.4, 290 mOsm). Series resistance was not compensated but was monitored continuously with negative voltage steps, and recordings with series resistances larger than 12 MOhm were not included in the estimation of EPSGT in control conditions or after gabazine treatment. None of the additional recordings in the study had series resistances larger than 20 MOhm. Voltage measurements were not corrected for the experimentally determined junction potential (-11.7 +/- 1.0 mV, n = 3). Experiments in the hippocampus were performed in the presence of the GABAB receptor antagonist CGP54626 (1–2 M) and the NMDA receptor antagonist R-(–)-3-(2-carboxypiperazine-4-yl)-propyl-1-phosphonic acid (RS-CPP, 25–50 M). The presence of the GABAB and NMDA receptor antagonists had no significant effect on the probability of eliciting a spike in pyramidal cells in response to threshold stimulation of Schaffer collaterals (CPP, 110.1 +/- 11.9%; CGP54626, 119.8 +/- 50.2%; P = 0.84 and 0.43, respectively).

Schaffer collaterals were stimulated (100 s) with constant current (range of 10–900 A) using a steel monopolar electrodes placed in the stratum radiatum of CA1. CA1 was isolated from CA3 and the subiculum by two radial cuts to prevent propagation of epileptiform activity.

Loose-patch recordings were performed with ACSF-filled patch pipettes (8–10 M). Field recordings were performed using patch pipettes (2–4 M) filled with 3 M NaCl. Data were recorded with Axopatch 200A, Axopatch 200B or Multiclamp 700A amplifiers (Axon Instruments); acquisition (5–10-kHz digitization) and analysis was performed with pCLAMP 9.2 software (Molecular Devices). Average values are expressed as means s.e.m. Student's t test was used for statistical comparisons. We used 2,3-dihydroxy-6-nitro-7-sulfamoyl-benzo[f]quinoxaline-2,3-dione (NBQX), SR95531 (gabazine), CGP54626, RS-CPP, DAMGO, CTAP and muscimol (Tocris Cookson).

Calibrating input strength.

The input strength is proportional to the number of activated Schaffer collaterals and varies from 0 to 1. It is a measure that allows comparison of stimulus intensities across slices. To estimate input strength, we used two experimentally determined parameters: the slope of the field EPSP (fEPSP), which is proportional to the number of activated Schaffer collaterals (Vaillend et al 2002, Nakamura et al 2007, Winegar & MacIver et al 2006, Steiger et al 1980), and the amplitude of the population spike. Accordingly, all experiments

in which the input strength is reported were performed in the presence of two field-potential recording electrodes, one placed in the stratum radiatum of CA1 (for fEPSPs) and one in the stratum pyramidale (for population spikes). The fEPSP was calibrated with respect to the simultaneously recorded population spike. Specifically, the slope of the fEPSP elicited at any given stimulus intensity was normalized by the slope of the fEPSP evoked at a stimulus intensity that evoked a population spike of 95% of its maximal amplitude. This normalization was done because even if the same number of Schaffer collaterals were recruited in two different slices, the absolute value of the slope of the fEPSP may vary (for example, as a result of a different positioning or depth of the recording electrode). The value of such normalized fEPSP is the input strength. Thus, the input strength is 1 when the number of stimulated Schaffer collateral triggers a population spike of 95% of its maximal amplitude and is 0.1 when the number of stimulated Schaffer collaterals is a tenth of the number it takes to trigger 95% population spike. For each slice, the input strength was always determined in control conditions. Thus, the number of Schaffer collaterals stimulated in control conditions or in gabazine is the same for a given input strength. In a subset of experiments, fEPSP was recorded in the stratum pyramidale. Experiments were only started once the amplitude of the population spike remained stable over a period of at least 10 min.

Threshold stimulation, activation curves and the measure of EPSCs and IPSCs peak amplitude, conductance and charge.

Neurons were recorded in the loose-patch configuration and the Schaffer collaterals stimulated at increasing intensities until about 50% of the trials elicited a spike in the recorded cells. Neurons recorded in the loose-patch configuration were subsequently re-patched with a pipette containing standard internal solution (see above) to gain whole-cell access. In a subset of the recording reported in Figures 1 and 2 (see legends), we determined threshold input strength using whole-cell recordings; the distribution of EPSGT with input strength did not differ significantly from the one obtained when threshold input strengths was determined in the loose-patch configuration (linear regressions, ANCOVA test on slopes, P = 0.13; intercepts, P = 0.1). The data were thus pooled.

The activation curve of a population of neurons (Figs. 1a) is the cumulative distribution of the input strengths that elicit 50% spiking probability in the neurons of that population. The 50% spiking probability of individual neurons was interpolated by fitting their spiking probability plotted against stimulus strength (Fig. 1.1a) with the sigmoid function $Y = \frac{100}{1+10^{p(x_0-x)}}$, where x0 is the input strength at 50% spiking probability and p is the slope at x0.

The increase in feedforward inhibition with input strength (Fig. 1.2a) was fitted with the Boltzmann equation $Y = A - \frac{A}{1+e^{\frac{(x-x_0)}{p}}}$, where A is the asymptote, x0 is the input strength at half maximal feedforward IPSG and p is the slope at x0.

Correlation analysis of EPSC and IPSC amplitudes.

The homogeneity of excitation (and inhibition) across the population of recorded neurons was accessed by correlating the average amplitude of EPSCs (or IPSCs) simultaneously recorded in cell pairs (Appendix). These paired data can yield a range of different correlation values depending on whether each pair of amplitudes, A and B, is plotted as (A,B) (that is, A on the x axis and B on the y axis) or (B,A). To account for this, we repeatedly calculated the correlation where the dataset was the same, but each pair of amplitudes was randomly assigned to be (A,B) or (B,A). The mean correlation values from this process were $R = 0.3$ for EPSC pairs and $R = 0.8$ for IPSC pairs. The correlation between IPSCs was significantly larger ($P < 0.02$), assessed using one-tail test of correlation for dependent variables44.

Computational model

We sought to design a simple model constrained by experimentally determined parameters (anatomical connectivity and average number of inputs required to reach threshold) to establish whether the experimentally measured increase in EPSGT can, in principle, account for the observed dynamic range of the activation curve. Our model predicts the fraction of pyramidal cells activated as a function of the number of active Schaffer collaterals, given a connectivity p of Schaffer collaterals onto pyramidal cells. We assume that all Schaffer collateral-pyramidal cell synapses have the same strength. Thus, the

distribution of inputs strengths onto the pyramidal cell population is given by the binomial probability distribution.

Accordingly the fraction A of active pyramidal cells given N active Schaffer collateral is

$$A_N = 1 - \sum_{i=0}^{T} \binom{N}{i} p^i (1-p)^{N-i}$$

where N is the number of Schaffer collaterals, and T is threshold of excitation expressed in terms of the number of active presynaptic inputs i. p is taken as 0.06 (ref. 25), and the fixed EPSGT activation curve was simulated using a constant threshold, T = 100 (Otmakhov et al 1993). To simulate the dynamic EPSGT activation curve, the threshold was 100 Schaffer collaterals initially, but changed as a function of input strength, T(N), optimized to minimize the distance between the simulated and experiment activation curves. This optimization was constrained by our experimental finding such that it increased by threefold, reaching a plateau when 65% of the pyramidal cells were active (Matlab, Mathworks).

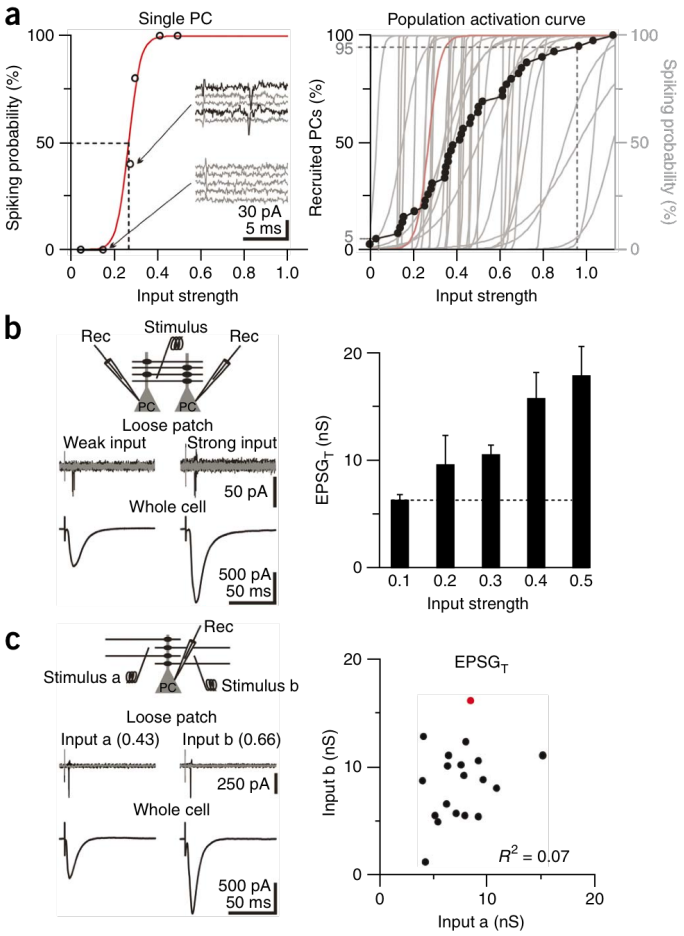

Fig. 1.1 The stronger the stimulus, the larger the excitation necessary to recruit a pyramidal cell.

(A) Left, spiking probability plotted against input strength for one CA1 pyramidal cell (PC, sigmoidal fit, dashed lines indicate 50% spiking probability). Inset, loose-patch recording at two different input strengths, five consecutive sweeps. Successes are shown in black and failures in gray. Right, black data points represent the activation curve (that is, the cumulative distribution of input strengths eliciting 50% spiking, n = 39). Dashed lines represent the input strengths recruiting 5% and 95% of the pyramidal cell population. Gray sigmoids indicate the spiking probability of the 39 pyramidal cells making up the activation curve. Their recruitment was staggered along the range of input strengths. Red sigmoid indicates the experiment shown on the left.

(B) Top left, recording configuration. Rec, recording electrode. Top traces represent the responses of two CA1 pyramidal cells simultaneously recorded in loose-patch to threshold stimulation of Schaffer collateral inputs (five superimposed sweeps; successes are shown in black, failures in gray). The pyramidal cell on the left was recruited at weaker stimulus than the pyramidal cell on the right. Bottom traces represent threshold EPSCs (that is, EPSCs evoked at threshold input strength, average of ten traces) recorded in the same two cells voltage clamped at -80 mV. The pyramidal cell on the left necessitated less excitation to reach threshold. Right, summary graph of $EPSG_T$s (black, n = 32, spike threshold determined in loose patch for n = 15 cells and in whole-cell current clamp for n = 17 cells) plotted against input strength at threshold (bin width 0.1). Dashed line represents the average $EPSG_T$ for the 0–0.1 bin. Error bars are s.e.m.

(C) Top left, recording configuration. Top traces represent the response of a single CA1 pyramidal cell recorded in loose patch to threshold stimulation of two different Schaffer collateral inputs (stimuli a and b, five superimposed sweeps each). Bottom traces represent threshold EPSCs (average of ten traces) recorded in the same cell voltage clamped at -90 mV. The difference in amplitude of the two threshold EPSCs should be noted. Right, summary graph (n = 19). There was no correlation between $EPSG_T$s evoked by input a and input b (linear regression, R^2 = 0.07; spike threshold determined in loose patch for all cells, red data point indicates the experiment shown on the left)

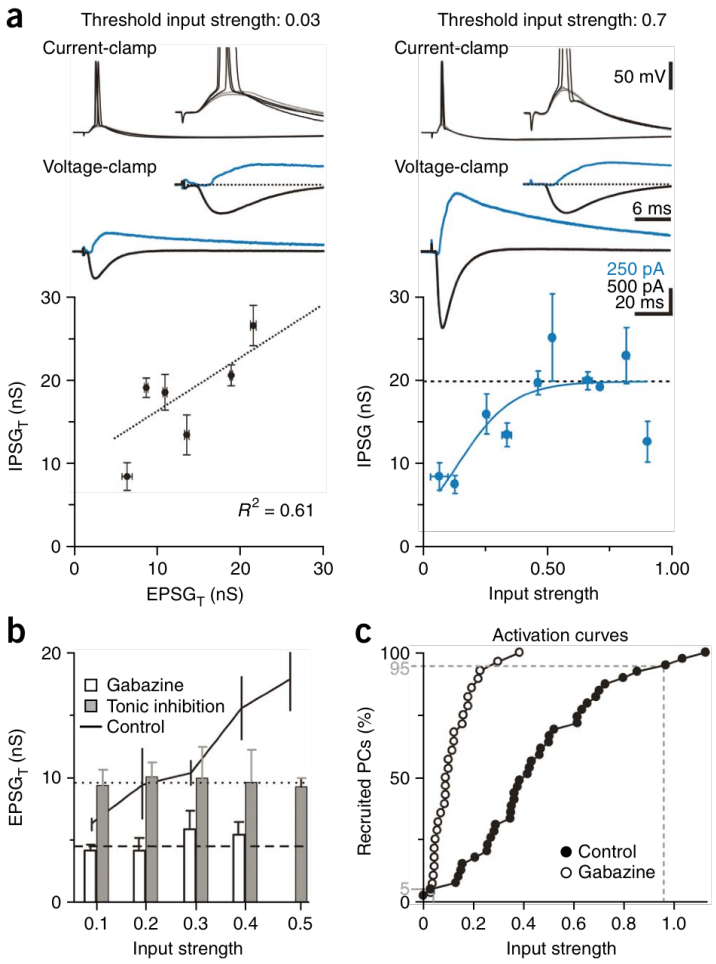

Fig. 1.2 Feedforward inhibition expands the dynamic range of the pyramidal cell population.

(A) Top traces represent whole-cell current-clamp recording from two CA1 pyramidal cells recruited at threshold by weak (left) or strong (right) Schaffer collateral stimulation (five superimposed sweeps; black indicates successes and gray indicates failures to trigger a spike). Bottom traces, represent threshold EPSC (black, average of five traces recorded in the voltage clamp, -88 and -92 mV for left and right, respectively) and concomitantly evoked feedforward IPSC (blue, recorded at -52 and -59 mV for left and right, respectively, and isolated by subtraction from average of ten sweeps). Insets represent expanded timescale of the sweeps. The size of the two insets has been scaled to match EPSC amplitudes. Bottom left, threshold feedforward IPSG (IPSGT) plotted against EPSGT (bin width of 2.5 nS, n = 30, spike threshold determined in loose patch for n = 19 cells and in whole-cell current clamp for n = 11 cells, dotted line is the linear regression fit of the binned data, R2 = 0.61, slope of 0.82). Bottom right, feedforward IPSG plotted against input strength (bin width of 0.1, n = 50, continuous blue line is a Boltzmann fit of the binned data). Error bars are s.e.m.

(B) Summary graph of EPSGTs plotted against input strength in the presence of gabazine (6 M, n = 30, spike threshold determined in loose patch for n = 20 cells and in whole-cell current clamp for n = 10 cells) or under tonic inhibition (1 M muscimol and 0.5–1 M DAMGO, n = 14, spike threshold determined in loose-patch for n = 11 cells and in whole-cell current clamp for n = 3 cells). Dotted and dashed horizontal lines represent the average EPSGT during tonic inhibition or gabazine treatment, respectively. In contrast with control conditions (black line from Fig. 1b), the EPSGT recorded in gabazine or tonic inhibition changed little with increasing input strength. For all input strengths, the EPSGT during tonic inhibition was larger than during gabazine treatment.

(C) Activation curves (cumulative distribution of input strengths eliciting 50% spiking) in control conditions (black symbols from Fig. 1a) and after gabazine treatment (n = 28, spike threshold determined in loose patch for all cells). Dashed lines indicate input strengths recruiting 5% and 95% of the pyramidal cell population. Error bars are s.e.m.

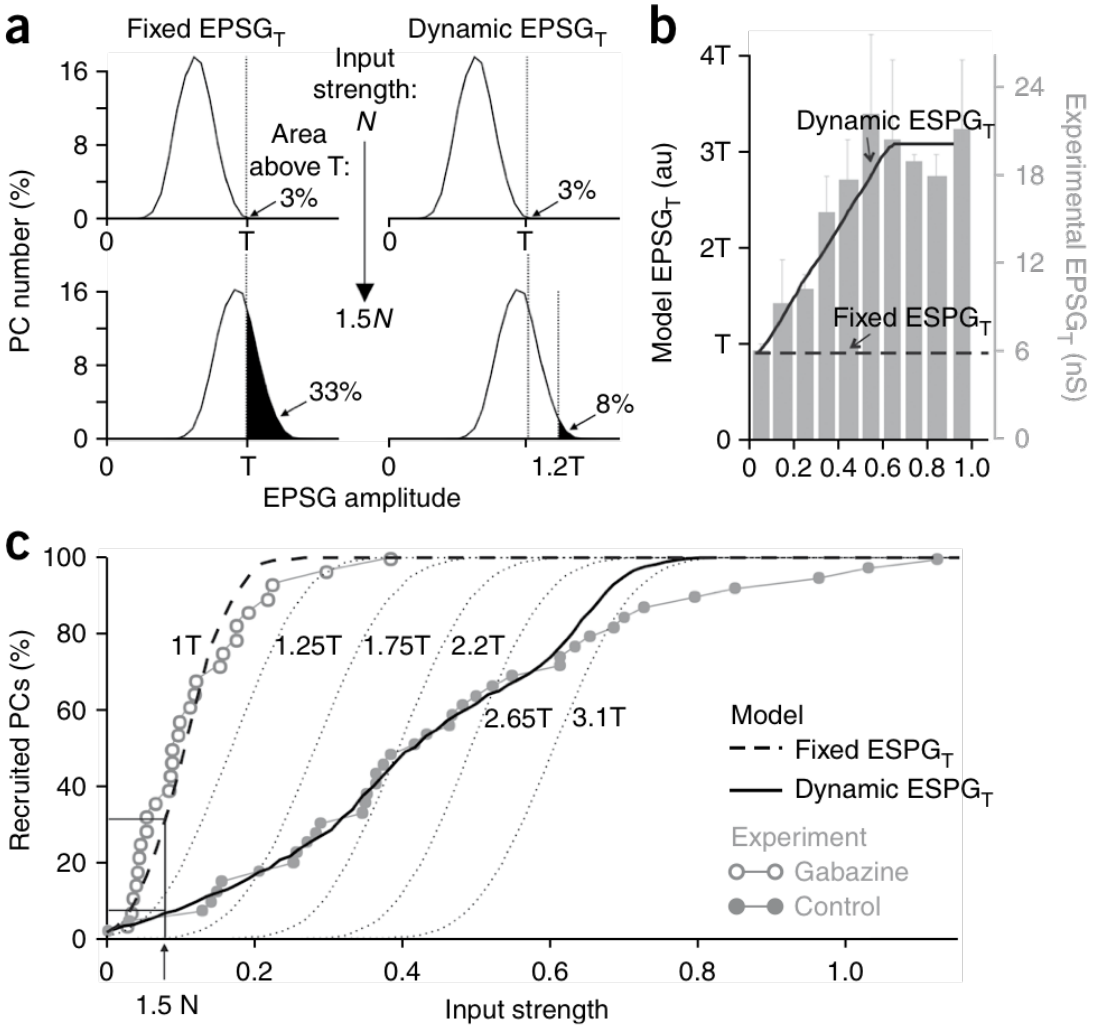

Fig. 1.3 Model of activation curve with dynamic EPSGT.

(A) Modeled distribution of EPSG amplitudes in the population of pyramidal cells when *N* (top row) and 1.5*N* (bottom) afferent fibers are active. The area above spike threshold T, under the curve (black shaded), is the fraction of pyramidal cells recruited with either fixed (left column) or dynamic (right) $EPSG_T$. For dynamic $EPSG_T$, a smaller fraction of pyramidal cells was recruited when increasing the number of active afferent fibers from *N* to 1.5*N*.

(B) $EPSG_T$ as a function of input strength used in the model; dynamic (continuous line), fixed (dashed line) and experimentally measured dynamic $EPSG_T$ (gray columns, same data as in Fig. 1 but for the entire range of stimulus strengths) are shown.

(C) Modeled pyramidal cell activation curves with fixed or dynamic $EPSG_T$. Experimentally measured activation curve in gabazine and control conditions are superimposed. Dotted gray lines represent a set of fixed $EPSG_T$ activation curves (for each activation curve, the threshold is given in multiples of T, the threshold at minimal input strength). The dynamic $EPSG_T$ activation curve intersects each of the fixed $EPSG_T$ activation curves at the specific input strength at which the threshold of the two curves matches. The dynamic $EPSG_T$activation curve thus results from the synthesis of a family of fixed $EPSG_T$ activation curves.

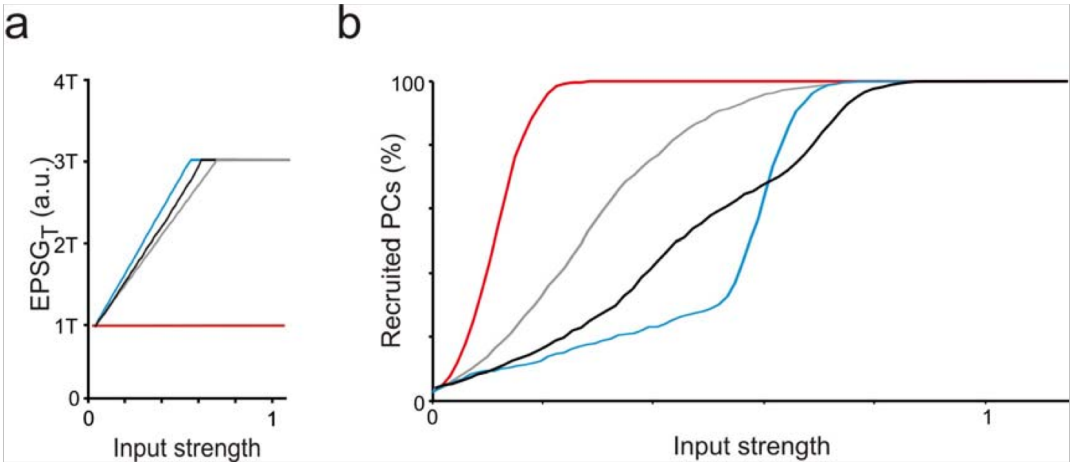

Fig. 1.4 Model activation curve sensitivity to different EPSGT functions

(A) EPSGT as a function of input strength used in the model. Dynamic-(black) and fixed-(red) EPSGT functions are the same as figure 6. Blue and gray curves illustrate an increase and decrease of the rate of increase of the EPSGT as a function of input strength by ~ 15% respectively.

(B) Activation curves generated using EPSGT functions in panel a. Note that an increase in the rate of EPSGT increase decreases the initial slope of the activation curve slope whereas a decrease in the rate of EPSGT increase has the opposite effect.

Appendix

Heterogeneous excitation and homogeneous inhibition

What determines which pyramidal cells in the population are recruited in response to Schaffer collateral stimulation? We recorded from two neighboring pyramidal cells simultaneously (somata separated by <50 um) and increased the number of activated Schaffer collaterals until one of the two cells spiked. We then compared the EPSGs and feedforward IPSGs in the two cells. Although the EPSG was, on average, 1.6 +/- 0.1–fold larger in the cell that spiked ($P = 0.001$, $n = 15$), the IPSG was, on average, not significantly different between the two neurons (1.1 +/- 0.1–fold difference, $P = 0.3$, $n = 15$;). Furthermore, the latency of the feedforward IPSC (with respect to the onset of the EPSC) did not differ significantly between spiking (1.75 +/- 0.09 ms) and nonspiking neurons (1.59 +/- 0.06 ms, $P = 0.09$, $n = 15$). Thus, differences in the amplitude of synaptic excitation, rather than in the amplitude or timing of inhibition, govern which neuron will spike in response to Schaffer collateral stimulation.

To determine whether inhibition is more homogeneously distributed across pyramidal cells as compared with excitation, we calculated how well the amplitude of inhibition in one cell correlated with the amplitude of inhibition in its neighbor and did the same for excitation. For this, we used the same paired values as described above, but we randomly allocated the spiking cell to either

one of the two axes. This randomization removes the correlation bias caused by systematically having the larger amplitude on the same axis. The correlation between IPSGs (RIn = 0.79) was significantly larger than the correlation between EPSGs (REx = 0.30, $P < 0.02$, see Experimental Procedures). These results indicate that, although FFI is relatively homogenous across the pyramidal cell population, and thus sets a global threshold for pyramidal cell recruitment by Schaffer collaterals, heterogeneities in excitation determine which pyramidal cells in the population overcome this threshold.

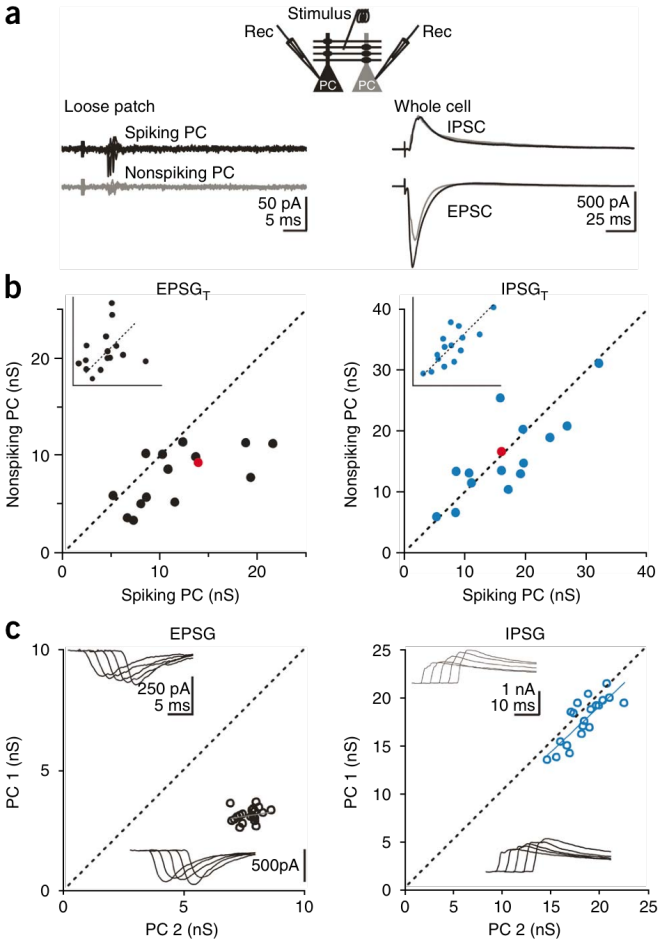

Fig. 1.A Homogeneous inhibition and heterogeneous excitation control the recruitment of pyramidal cells.

(A) Top, recording configuration. Left traces represent simultaneous loose-patch recording from two neighboring CA1 pyramidal cells. Schaffer collaterals stimulation was sufficiently strong to reach threshold in one cell (black traces, five superimposed sweeps), but not in the other (gray traces). Right traces represent whole-cell voltage-clamp recording from the same two neurons (top, feedforward IPSCs recorded at -60 mV and isolated by subtraction from average of ten traces; bottom, EPSCs recorded at -80 mV, average of ten traces). The amplitude of the feedforward IPSC was similar in both cells, whereas the EPSC was larger in the cell that spiked.

(B) Left, summary graph of 15 similar experiments in which the EPSG in the nonspiking cell is plotted against the EPSG in the spiking cell. The majority of the data points are below the unity line (red data point indicates the experiment shown on top). Right, summary graph of the same 15 experiments in which the feedforward IPSG in the nonspiking cell is plotted against the feedforward IPSG in the spiking cell. In contrast with the EPSG, all of the data points are scattered around the unity line (spike threshold determined in loose patch for n = 8 pairs and in whole-cell current clamp for n = 7 pairs; red data point indicates experiment shown in (A); Error bars are s.e.m. Insets have the same data points as are shown in the main graphs, but the spiking cell is randomly allocated to either one of the two axes. Note the larger spread of EPSGs as compared with IPSGs.

(C) Trial-by-trial fluctuation of EPSGs (left) and IPSGs (right) simultaneously recorded in two pyramidal cells (PC 1 and PC 2) voltage clamped at the reversal potential of IPSCs (left) or EPSCs (right, same Schaffer collateral stimulation intensity for both holding potentials, cesium internal). Left, single-trial EPSGs recorded in PC 1 are plotted against the EPSGs recorded simultaneously in PC 2. Upper traces are five example EPSCs recorded in PC 1 ordered according to amplitude. Lower traces are the corresponding five EPSCs recorded simultaneously in PC 2. Right, single-trial IPSGs recorded in PC 1 are plotted against the IPSGs recorded simultaneously in PC 2. Upper traces are five example IPSCs recorded in PC 1 ordered according to amplitude. Lower traces are the corresponding five IPSCs recorded simultaneously in PC 2. Note the marked covariation in amplitude of IPSGs recorded in the two pyramidal cells as compared with EPSGs.

Acknowledgements

This chapter contains a reprinted material as it appears Input normalization by global feedforward inhibition expands cortical dynamic range Pouille F, Marin-Burgin A, Adesnik H, Atallah BV, Scanziani M. Nat Neurosci. 2009 Dec;12(12):1577-85.

The dissertation author was an author for this material contributing analysis and designed the model. Experiments were performed by authors F. Pouille, A. Marin-Burgin and H. Adesnik. Permission reprint of material is granted by all original authors.

References

1. Lefort, S., Tomm, C., Floyd Sarria, J.C. & Petersen, C.C. The excitatory neuronal network of the C2 barrel column in mouse primary somatosensory cortex. Neuron 61, 301–316 (2009).

2. Otmakhov, N., Shirke, A.M. & Malinow, R. Measuring the impact of probabilistic transmission on neuronal output. Neuron 10, 1101–1111 (1993).

3. Marr, D. A theory of cerebellar cortex. J. Physiol. (Lond.) 202, 437–470 (1969).

4. Vogels, T.P. & Abbott, L.F. Signal propagation and logic gating in networks of integrate-and-fire neurons. J. Neurosci. 25, 10786–10795 (2005).

5. Shadlen, M.N. & Newsome, W.T. The variable discharge of cortical neurons: implications for connectivity, computation and information coding. J. Neurosci. 18, 3870–3896 (1998).

6. Diesmann, M., Gewaltig, M.O. & Aertsen, A. Stable propagation of synchronous spiking in cortical neural networks. Nature 402, 529–533 (1999).

7. Arabzadeh, E., Zorzin, E. & Diamond, M.E. Neuronal encoding of texture in the whisker sensory pathway. PLoS Biol. 3, e17 (2005).

8.Wilson, M.A. & McNaughton, B.L. Dynamics of the hippocampal ensemble code for space. Science 261, 1055–1058 (1993).

9. Csicsvari, J., Hirase, H., Mamiya, A. & Buzsaki, G. Ensemble patterns of hippocampal CA3–CA1 neurons during sharp wave–associated population events. Neuron 28,585–594 (2000).

10. Shu, Y., Hasenstaub, A., Badoual, M., Bal, T. & McCormick, D.A. Barrages of synaptic activity control the gain and sensitivity of cortical neurons. J. Neurosci.23, 10388–10401 (2003).

11. Mitchell, S.J. & Silver, R.A. Shunting inhibition modulates neuronal gain during synaptic excitation. Neuron 38, 433–445 (2003).

12. Chance, F.S., Abbott, L.F. & Reyes, A.D. Gain modulation from background synaptic input. Neuron 35, 773–782 (2002).

13. Carvalho, T.P. & Buonomano, D.V. Differential effects of excitatory and inhibitory plasticity on synaptically driven neuronal input-output functions. Neuron 61, 774–785 (2009).

14. Tropp Sneider, J., Chrobak, J.J., Quirk, M.C., Oler, J.A. & Markus, E.J. Differential behavioral state-dependence in the burst properties of CA3 and CA1 neurons. Neuroscience 141, 1665–1677 (2006).

15. Pouille, F. & Scanziani, M. Enforcement of temporal fidelity in pyramidal cells by somatic feedforward inhibition. Science 293, 1159–1163 (2001).

16. Buzsáki, G. Feed-forward inhibition in the hippocampal formation. Prog. Neurobiol. 22, 131–153 (1984).

17.Alger, B.E. & Nicoll, R.A. Feed-forward dendritic inhibition in rat hippocampal pyramidal cells studied in vitro. J. Physiol. (Lond.) 328, 105–123 (1982).

18. Nicoll, R.A., Alger, B.E. & Jahr, C.E. Enkephalin blocks inhibitory pathways in the vertebrate CNS. Nature 287, 22–25 (1980).

19. Somogyi, P. & Klausberger, T. Defined types of cortical interneurone structure space and spike timing in the hippocampus. J. Physiol. (Lond.) 562, 9–26 (2005).

20.Freund, T.F. & Buzsáki, G. Interneurons of the hippocampus. Hippocampus 6, 347–470 (1996).

21. Glickfeld, L.L. & Scanziani, M. Distinct timing in the activity of cannabinoid-sensitive and cannabinoid-insensitive basket cells. Nat. Neurosci. 9, 807–815 (2006).

22. Maccaferri, G. & Dingledine, R. Control of feedforward dendritic inhibition by NMDA receptor–dependent spike timing in hippocampal interneurons. J. Neurosci. 22, 5462–5472 (2002).

23. Geiger, J.R., Lubke, J., Roth, A., Frotscher, M. & Jonas, P. Submillisecond AMPA receptor–mediated signaling at a principal neuron-interneuron synapse. Neuron 18,1009–1023 (1997).

24. Cruikshank, S.J., Lewis, T.J. & Connors, B.W. Synaptic basis for intensethalamocortical activation of feedforward inhibitory cells in neocortex. Nat. Neurosci.10, 462–468 (2007).

25. Sayer, R.J., Friedlander, M.J. & Redman, S.J. The time course and amplitude ofEPSPs evoked at synapses between pairs of CA3/CA1 neurons in the hippocampalslice. J. Neurosci. 10, 826–836 (1990).

26.Gabernet, L., Jadhav, S.P., Feldman, D.E., Carandini, M. & Scanziani,M. Somatosensory integration controlled by dynamic thalamocortical feed-forward inhibition. Neuron 48, 315–327 (2005).

27. Helmstaedter, M., Staiger, J.F., Sakmann, B. & Feldmeyer, D. Efficient recruitment of layer 2/3 interneurons by layer 4 input in single columns of rat somatosensory cortex. J. Neurosci. 28, 8273–8284 (2008).

28. Daw, M.I., Ashby, M.C. & Isaac, J.T. Coordinated developmental recruitment of latent fast spiking interneurons in layer IV barrel cortex. Nat. Neurosci. 10, 453–461 (2007).

29. Mittmann, W., Koch, U. & Hausser, M. Feed-forward inhibition shapes the spike output of cerebellar Purkinje cells. J. Physiol. (Lond.) 563, 369–378 (2005).

30. Saito, T. & Nakatsuji, N. Efficient gene transfer into the embryonic mouse brain using in vivo electroporation. Dev. Biol. 240, 237–246 (2001).

31. Petreanu, L., Huber, D., Sobczyk, A. & Svoboda, K. Channelrhodopsin-2–assisted circuit mapping of long-range callosal projections. Nat. Neurosci. 10, 663–668 (2007).

32. Bruno, R.M. & Sakmann, B. Cortex is driven by weak, but synchronously active, thalamocortical synapses. Science 312, 1622–1627 (2006).

33. Porter, J.T., Johnson, C.K. & Agmon, A. Diverse types of interneurons generate thalamus-evoked feedforward inhibition in the mouse barrel cortex. J. Neurosci. 21, 2699–2710 (2001).

34. Poo, C. & Isaacson, J.S. Odor representations in olfactory cortex: “sparse” coding, global inhibition and oscillations. Neuron 62, 850–861 (2009).

35. Holmgren, C., Harkany, T., Svennenfors, B. & Zilberter, Y. Pyramidal cell communication within local networks in layer 2/3 of rat neocortex. J. Physiol. (Lond.) 551, 139–153 (2003).

36. Beierlein, M., Gibson, J.R. & Connors, B.W. Two dynamically distinct inhibitory networks in layer 4 of the neocortex. J. Neurophysiol. 90, 2987–3000 (2003).

37. Thomson, A.M., West, D.C., Wang, Y. & Bannister, A.P. Synaptic connections and small circuits involving excitatory and inhibitory neurons in layers 2–5 of adult rat and cat neocortex: triple intracellular recordings and biocytin labeling in vitro. Cereb.Cortex 12, 936–953 (2002).

38. Buhl, E.H., Halasy, K. & Somogyi, P. Diverse sources of hippocampal unitary inhibitory postsynaptic potentials and the number of synaptic release sites. Nature 368, 823–828 (1994).

39. Blitz, D.M. & Regehr, W.G. Timing and specificity of feed-forward inhibition within the LGN. Neuron 45, 917–928 (2005).

40. Agmon, A. & Connors, B.W. Thalamocortical responses of mouse somatosensory (barrel) cortex in vitro. Neuroscience 41, 365–379 (1991).

41. Vaillend, C., Mason, S.E., Cuttle, M.F. & Alger, B.E. Mechanisms of neuronal hyperexcitability caused by partial inhibition of Na+-K+-ATPases in the rat CA1 hippocampal region. J. Neurophysiol. 88, 2963–2978 (2002).

42. Nakamura, M., Sekino, Y. & Manabe, T. GABAergic interneurons facilitate mossy fiber excitability in the developing hippocampus. J. Neurosci. 27, 1365–1373 (2007).

43. Winegar, B.D. & MacIver, M.B. Isoflurane depresses hippocampal CA1 glutamate nerve terminals without inhibiting fiber volleys. BMC Neurosci. 7, 5 (2006).

44. Steiger, J.H. Tests for comparing elements of a correlation matrix. Psychol. Bull. 87, 245–251 (1980).

Chapter 2. Supralinear increase of recurrent inhibition during sparse activity in the somatosensory cortex

Abstract

The balance between excitation and inhibition in the cortex is crucial in determining sensory processing. Because the amount of excitation varies, maintaining this balance is a dynamic process; yet the underlying mechanisms are poorly understood. We show here that the activity of even a single layer 2/3 pyramidal cell in the somatosensory cortex of the rat generates widespread inhibition that increases disproportionately with the number of active pyramidal neurons. This supralinear increase of inhibition results from the incremental recruitment of somatostatin-expressing inhibitory interneurons located in layers 2/3 and 5. The recruitment of these interneurons increases tenfold when they are excited by two pyramidal cells. A simple model demonstrates that the distribution of excitatory input amplitudes onto inhibitory neurons influences the sensitivity and dynamic range of the recurrent circuit. These data show that through a highly sensitive recurrent inhibitory circuit, cortical excitability can be modulated by one pyramidal cell

Introduction

Sensory stimuli both excite and inhibit cortical neurons (Ferster & Jagadeesh 1992, Wehr & Zador 2003, Zhu & Connors 1999, Wilent & Contreras 2004, Douglas et al 1991, Anderson et al 2000). The fraction of cortical neurons that respond to a sensory stimulus, and the timing of these neuronal responses, depend on the relative amount of synaptic excitation and inhibition they receive (Wehr & Zador 2003, Anderson et al 2000, Wilent & Contreras 2005, Gabernet et al 2005). Disrupting this balance, for example through pharmacological manipulations, interferes with the response of cortical neurons to several properties of the stimulus, including orientation, contrast and the receptive field size (Dykes et al 1984, Kyriazi et al 1996, Sillito 1975).

Maintaining a balance between excitation and inhibition is a dynamic process. Variations in stimulus intensity are accompanied by large changes in the amount of excitation received by cortical neurons. These changes in excitation are rapidly countered by changes in synaptic inhibition within several primary sensory areas (Wehr & Zador 2003, Wilent & Contreras 2004, Anderson et al 2000). However, the mechanisms by which cortical circuits vary the strength of inhibition during ongoing changes in excitation are not well understood. Although recurrent inhibitory circuits seem to be well suited to provide this dynamic regulation (Pouille & Scanziani 2004, Shu et al 2003, Carandini & Heeger 1997) their specific contribution to the inhibition of primary sensory areas is not known. Furthermore, the relative proportion of excitation

and inhibition experienced by cortical neurons in response to sensory stimuli is still debated. Although some data indicate that inhibition increases linearly with the amount of excitation received by cortical neurons (Wehr & Zador 2003, Wilent & Contreras 2004, Anderson et al 2000), other results and theoretical considerations suggest that a nonlinear increase of inhibition may better account for the observed cortical responses to sensory stimuli (Pinto et al 2003).

The somatosensory 'barrel' cortex of the rat receives sensory information from the whiskers. The number of cortical neurons excited by whisker deflection increases with the velocity of the deflection (Pinto et al 2000). However, even strong stimuli trigger spikes in only a very small fraction of synaptically excited cortical neurons (Brecht et al 2003). Whether this small fraction is sufficient to recruit inhibition and how inhibition increases with increasing number of activated neurons are unknown.

Here we show that even very sparse excitation triggers widespread synaptic inhibition in layer 2/3 cortical neurons by recruiting intra- and translaminar recurrent inhibitory circuits. Furthermore, this inhibition increases disproportionately with increases in excitation. A simple model based on experimentally determined parameters captures the essential properties of this behavior and illustrates the cellular mechanism affecting the scaling between excitation and inhibition in response to the spiking of a few pyramidal cells. Together, these findings suggest common principles of operation of elementary circuits across cortical layers.

Results

Recurrent inhibition triggered by a single pyramidal cell

To determine the minimal conditions (Kozloski et al 2001) required to generate inhibition in the somatosensory cortex, we performed double or triple recordings from pyramidal cells in layer 2/3 of slices of rat somatosensory cortex (distance between cell bodies <50 um; 194 pairs tested in 305 directions; each double recording corresponds to one pair that can be tested in maximally two directions, and each triple recording corresponds to three pairs that can be tested in maximally six directions). In 12.5% of all directions tested (38 of 305), a train of ten action potentials at 100–125 Hz triggered in an individual pyramidal cell elicited an outward current in the simultaneously recorded 'target' pyramidal cell (voltage clamped at -40 mV; Fig 2.1a). The onset of the outward current occurred, on average, between the fourth and the fifth action potential in the train (4.9 +/- 0.31, n = 38), and its peak amplitude was 15.5 +/- 2.1 pA (n = 38; Fig 2.1b). When the target cell was recorded in current clamp (Vm = -50.2 +/- 1.0 mV, n = 9), the resulting synaptic hyperpolarization averaged 1.1 +/- 0.2 mV (n = 9; Fig 2.1c). The outward current was blocked by the GABAA receptor antagonist gabazine and was evoked in the presence of the GABAB receptor antagonist CGP54626. Furthermore, the outward current was abolished by the glutamate receptor antagonist NBQX (10 uM; n = 12;Fig 2.1d), indicating that it resulted from synaptic recruitment of GABAergic interneurons rather than from monosynaptic GABA release between two recorded neurons. These results

demonstrate that, under the present conditions, recurrent inhibitory circuits in layer 2/3 of the somatosensory cortex can be recruited by as few as four action potentials in a single pyramidal cell.

To determine the fraction of neighboring pyramidal cells inhibited by these unitary recurrent inhibitory circuits, we first assessed the activation of recurrent inhibitory circuits on a target pyramidal cell in response to the spiking of a neighboring pyramidal cell and then established the probability of observing inhibition on a second target pyramidal cell. For this we recorded from three pyramidal cells (either as sequential pairs or as simultaneous triples): two in the voltage-clamp configuration to monitor synaptic currents and one in current clamp to elicit action potentials. In 20.4% (21 of 103) of all recordings, inhibition could be confirmed in at least one of the two voltage-clamped target cells. If inhibition was confirmed in one of the pyramidal cells, the chance of observing inhibition in the other was 38.1% (8 of 21; Fig 2.1e).

These results demonstrate that, through the activation of recurrent inhibitory circuits, a single layer 2/3 pyramidal cell of the somatosensory cortex can inhibit about 40% of its neighbors.

To determine the fraction of neighboring pyramidal cells inhibited by these unitary recurrent inhibitory circuits, we first assessed the activation of recurrent inhibitory circuits on a target pyramidal cell in response to the spiking of a neighboring pyramidal cell and then established the probability of observing inhibition on a second target pyramidal cell. For this we recorded from three pyramidal cells (either as sequential pairs or as simultaneous triples): two in the

voltage-clamp configuration to monitor synaptic currents and one in current clamp to elicit action potentials. In 20.4% (21 of 103) of all recordings, inhibition could be confirmed in at least one of the two voltage-clamped target cells. If inhibition was confirmed in one of the pyramidal cells, the chance of observing inhibition in the other was 38.1% (8 of 21; Fig 2.1e).

These results demonstrate that, through the activation of recurrent inhibitory circuits, a single layer 2/3 pyramidal cell of the somatosensory cortex can inhibit about 40% of its neighbors.

Supralinear increase of recurrent inhibition

To determine whether inhibition increases when more pyramidal cells are synchronously active, we next performed simultaneous triple recordings and triggered trains of action potentials in two pyramidal cells while monitoring inhibition in a third voltage-clamped target pyramidal cell.

When two pyramidal cells were activated together, the probability of triggering inhibition in a target pyramidal cell was much higher than what would be expected if the two pyramidal cells were activating independent inhibitory circuits. Whereas the probability (p) of eliciting inhibition in a target pyramidal cell with spikes triggered in a single pyramidal cell was 0.125 (that is, 12.5%, 38 of 305, see above), the probability increased to 0.477 (56 of 120) when two pyramidal cells were spiking simultaneously (Fig 2.2a). This is about twice the expected probability ((1 - (1 - p)2) = 0.234) if each individual pyramidal cell

recruited independent inhibitory circuits, suggesting that pyramidal cells cooperate in the recruitment of recurrent inhibition.

We next determined whether the inhibition evoked in a target pyramidal cell (PC1) in response to the simultaneous activity of two pyramidal cells (PC2 and PC3) was merely the sum of inhibition triggered when either PC2 or PC3 were active independently or whether inhibition increased in a nonlinear manner (Fig 2.2b,c). Trains of action potentials evoked simultaneously in PC2 and PC3 elicited an inhibitory current in PC1 whose integral (the inhibitory charge) was three times larger (see below) than the sum of the inhibitory charges elicited in PC1 by independently spiking PC2 and PC3. To quantify the increase of inhibition, we computed the nonlinearity index NL as $(I_{PC2PC3} - (I_{PC2} + I_{PC3}))/I_{PC2PC3}$, where I_{PC2} and I_{PC3} are the inhibitory charges recorded in PC1 in response to the spiking of either PC2 or PC3, respectively, and I_{PC2PC3} is the inhibitory charge recorded in PC1 when PC2 and PC3 are active simultaneously. NL is 1 when supralinearity is maximal (that is, $I_{PC2} = 0$, $I_{PC3} = 0$ and $I_{PC2PC3} > 0$; for example, Fig 2.2a), 0 when inhibition sums linearly (that is, $I_{PC2} + I_{PC3} = I_{PC2PC3}$), and negative for sublinearity (that is, $I_{PC2}+I_{PC3} > I_{PC2PC3}$). The NL averaged 0.68 +/- 0.06 (n = 38; Fig 2.2c; and thus I_{PC2PC3} 3 x $(I_{PC2} + I_{PC3})$), indicating that there was a strong supralinear increase of inhibition when PC2 and PC3 were spiking together. These results indicate that, as the number of spiking pyramidal cells increases, both the probability and the amount of recurrent inhibition generated in layer 2/3 of the somatosensory cortex increase supralinearly; furthermore, the onset of inhibition occurs earlier.

A tenfold increase in the recruitment of SOM interneurons

After identifying the type of interneuron that generates recurrent inhibition in response to sparse activity in layer 2/3 (see Appendix where we demonstrated that somatostatin, SOM, expressing interneurons are responsible for this inhibition) we can now determine the mechanism underlying the observed supralinear increase in inhibition. Toward this end, we first estimated the increase in the average number of recruited SOM interneurons when two pyramidal cells are active, as compared to one. Then we determined the increase in the probability of recruiting SOM interneurons that receive input from both active pyramidal cells (Fig 2.3).

As shown above, when the number of active pyramidal cells increases from 1 to 2, the chance of a neighboring pyramidal cell being inhibited increases from 0.125 (P_{inh1}) to 0.477 (P_{inh2}). Can we use this information to deduce the increase in the average number of recruited SOM interneurons? Unfortunately, we do not know how many SOM interneurons participate in the inhibition of a pyramidal cell. However, in the cases where no inhibition is observed ($1 - P_{inh1}$), none of the recruited interneurons contacts the recorded pyramidal cell. Thus, given the connectivity of an SOM interneuron to a pyramidal cell (PIP), we can determine the number of SOM interneurons recruited, N1 and N2, when one or two pyramidal cells are active, respectively: $(1 - P_{inh1}) = (1 - P_{IP})^{N1}$; $(1 - P_{inh2}) = (1 - P_{IP})^{N2}$.

By applying the experimentally determined P_{IP} (0.49; 19 connections out of 39 pairs; see Methods), we can solve for N1 and N2 (N1 = 0.2; N2 = 0.96; Fig 2.5b). Thus, increasing the number of pyramidal cells spiking from 1 to 2 increases the average number of recruited SOM interneurons by a factor of 5 (N2/N1 = 4.85; Fig 2.3b).

We can now estimate the increase in the probability of recruiting SOM interneurons in the subpopulation that receives convergent input from both active pyramidal cells. Because only the fraction $(P_{PI})^2$ of SOM interneurons receives convergent input from both pyramidal cells (where P_{PI} is the connectivity of a pyramidal cell to an SOM interneuron), only part of the fivefold increase is due to cooperative recruitment. We determined the probability P_{PI} that a layer 2/3 pyramidal cell excites an SOM interneuron (0.29; n = 29 pairs; see Methods). The probability of recruiting those SOM interneurons receiving convergent input from two active pyramidal cells increased 11.8 times (Fig 2.3c; see Experimental Procedures).

Thus, these results show that the supralinear increase in inhibition when two pyramidal cells are spiking is due to a fivefold increase in the number of recruited SOM interneurons. This increase in the number of active SOM interneurons mainly results from the fact that the recruitment of SOM interneurons contacted by two active pyramidal cells increases by an order of magnitude.

Range and sensitivity

How does the increase in inhibition progress when more than two pyramidal cells are active simultaneously? Based on the experimentally determined properties of the circuit, we first constructed a simple model that captures the observed increase in inhibition. We then used this model to predict the dynamic behavior of the circuit for a wider range of pyramidal cell activity (Fig 2.4).

The model incorporates three parameters: the probability of a layer 2/3 pyramidal cell exciting an SOM interneuron (P_{PI} = 0.29; n = 29 pairs, see above), the distribution of the peak amplitudes of the EPSPs recorded in SOM interneurons in response to ten action potentials in a pyramidal cell (mean, 3.3 mV; median, 2.8 mV; s.d., 2.7 mV; range, from <1 mV to >10 mV; n = 31; Fig 2.6), and the threshold for action potential generation in SOM interneurons (Wang et al 2004). The EPSP amplitude distribution used for the model, D1, was obtained by fitting the experimentally determined EPSP distribution with an alpha function (Fig 2.4a; see Methods). Using PPI, we then calculated the distribution of EPSP amplitudes, D2, received by the interneuron population when two pyramidal cells are spiking. With a threshold of 11.3 mV above resting membrane potential (see Methods), D2 leads to a fivefold increase in the fraction of interneurons that are active as compared to D1, indicating that our model captures the specific behavior of the recurrent inhibitory circuit onto layer 2/3 pyramidal cells (Fig 2.4b).

With the same parameters, we can now use the model to predict the evolution of inhibition when more than two pyramidal cells are simultaneously spiking. The activation curve (Fig 2.4b) shows that the recruitment of inhibitory interneurons begins with only one active pyramidal cell and increases supralinearly when up to about four pyramidal cells are simultaneously active. Inhibition then progresses linearly over a relatively wide range, and half-maximal activation of the interneuron population occurs when nine pyramidal cells are firing (Fig 2.4b).

What properties of the EPSP distribution between layer 2/3 pyramidal cells and SOM interneurons dictate this dynamic behavior? The distribution of EPSPs has a relatively small mean, yet is skewed toward larger amplitudes (see above; Fig 2.4a). These few large-amplitude EPSPs provide 'sensitivity' to the circuit because they allow the spiking of a single pyramidal cell to excite a fraction of its target SOM interneurons above threshold for spike generation. In fact, a hypothetical EPSP distribution with the same mean but no skew yields an activation curve with an onset shifted to the right; that is, more active pyramidal cells are needed before the first interneuron is recruited (Fig 2.4c, thin gray line). The relatively small mean of the EPSP distribution, on the other hand, allows the activation of SOM interneurons to progress over a relatively wide 'range' of activities in the pyramidal cell population. In fact, a hypothetical EPSP distribution in which the same fraction of EPSPs are above threshold, yet with a larger mean as compared to the experimentally observed distribution, yields an activation curve where the spiking of only five pyramidal cells is

necessary to recruit half of the SOM interneuron population. Furthermore, by increasing with a steeper slope, the function reaches saturation rather quickly (Fig 2.4c, thick gray line). Thus, the distribution of EPSPs onto SOM interneurons (with a small mean but skewed toward large amplitudes) provides both sensitivity and a broad dynamic range to recurrent inhibition of layer 2/3 pyramidal cells.

This model illustrates the progression in the recruitment of SOM interneurons with increasing numbers of simultaneously active pyramidal cells each firing ten action potentials. How does this progression change if pyramidal cells are firing only three action potentials (a situation that may be closer to the brief burst of spikes recorded in vivo in response to sensory stimulation Svoboda et al 1997, Svoboda et al 1999)? The distribution of EPSP amplitudes recorded in SOM interneurons in response to the third action potential in the presynaptic pyramidal cell can be directly extracted from our dataset (Appendix Fig 2.f). Unsurprisingly, the recruitment of SOM interneurons in response to three action potentials requires the activity of more active pyramidal cells (half-maximal activation 14; Fig 2.5). Further, the recruitment of SOM interneurons increases with a shallower slope, thereby covering a broader range.

Hence, even during very sparse activity in layer 2/3 of the somatosensory cortex, intra- and translaminar recurrent inhibitory circuits involving SOM interneurons are recruited, resulting in widespread inhibition of pyramidal cells. Because of the large increase in the probability of spiking of SOM interneurons, recurrent inhibition increases supralinearly with increases in

the number of active pyramidal cells. Our model shows that both the sensitivity of recurrent inhibition and its dynamic range result from the skewed distribution of EPSPs onto SOM interneurons.

Discussion

In the cortex, changes in excitation are continuously countered by corresponding changes in inhibition (Wehr & Zador 2003, Anderson et al 2000, Wilent & Contreras 2005, Gabernet et al 2005, Shu et al 2003, Haider et al 2006). The cellular mechanisms underlying this balancing are poorly understood. Neither the minimal conditions required to generate inhibition nor the dynamics of the increase of inhibition are known. Here we show that sparse excitatory activity in layer 2/3 of the somatosensory cortex specifically recruits a recurrent inhibitory circuit involving SOM interneurons that are located in layers 2/3 and 5. Through this circuit a single pyramidal cell can cause inhibition of almost 40% of its neighbors. Furthermore, when two pyramidal cells are spiking simultaneously, recurrent inhibition increases disproportionately owing to the tenfold increase in the recruitment of SOM interneurons receiving convergent inputs. A simple model, based on experimentally determined parameters, illustrates how the specific distribution and connectivity of excitation onto interneurons dictates the sensitivity and the dynamic range of the circuit.

Dynamics of recurrent inhibition in cortical layer 2/3

Not only do recurrent inhibitory circuits through SOM interneurons necessitate that little cortical activity be recruited, but their recruitment progresses supralinearly with slight increases in excitation. We show that the number of spiking interneurons increases fivefold (N1/N2 = 4.85) when a second pyramidal cell is engaged. Two key parameters determine the increase in the recruitment of inhibitory neurons with increasing number of active pyramidal cells: the distribution of the amplitudes of excitatory inputs onto SOM interneurons with respect to spike threshold and the convergence of pyramidal cells onto SOM interneurons. If, for example, layer 2/3 pyramidal cells evoked sufficiently large EPSPs to trigger a spike in all their target SOM interneurons, yet the probability of contacting an SOM interneuron were very low, the fraction of activated SOM interneurons would grow almost linearly with the number of active pyramidal cells. In contrast, if the probability of contacting SOM interneuron were high, the fraction of activated SOM interneurons would reach its maximum very quickly.

Our study shows that, in contrast to the above example, the distribution of unitary EPSPs onto SOM interneurons is skewed toward small values, such that only a fraction of interneurons receiving inputs from any given pyramidal cell will reach threshold for spike generation. However, because of the relatively large convergence of pyramidal cells onto SOM interneurons (0.3), about 10% (0.32) of the interneuron population will receive convergent inputs from any two active pyramidal cells. The recruitment of SOM interneurons increases by ten times for that population receiving convergent inputs from two active pyramidal

cells. Thus, the supralinear increase in inhibition can be accounted for by the tenfold increase in the recruitment of 10% of the SOM interneuron population.

By using a simple model that incorporates experimentally determined connectivity parameters, we can, at least qualitatively, predict the behavior of recurrent inhibition when many pyramidal cells are active. Our model shows that, after an early supralinear recruitment of interneurons, increases in inhibition become proportional to those of excitation over a relatively wide range. For a given connectivity between layer 2/3 pyramidal cells and SOM interneurons, both the early recruitment and the wide linear range of increase depend on the shape of the EPSP distribution. The few large-amplitude EPSPs ensure that even the activity of a single pyramidal cell will activate a fraction of the interneuron population, thus providing sensitivity to the circuit. Because of the skew of the distribution, large-amplitude EPSPs are likely to be under-sampled in our database, and hence the distribution used in our model is only an approximation of the real distribution. Furthermore, because of the cutting of axonal and dendritic processes during the slicing procedure, both the connectivity between neurons and the size of unitary EPSPs are probably underestimated. However, this underestimation is unlikely to qualitatively affect our conclusions, as larger amplitudes would further enhance the capacity of individual pyramidal cells to recruit SOM interneurons.

The small mean of the EPSP distribution ensures that during stronger cortical activity, recruitment of interneurons proceeds almost linearly over a wide range before reaching saturation. Notably, during relatively high levels of

excitation, linear changes in cortical inhibition have been observed both in vitro (Shu et al 2003) and in vivo (Wehr & Zador 2003, Anderson et al 2000, Haider et al 2006) suggesting that the distributions of EPSP amplitudes and the specific connectivity of the circuit may have a crucial role in correctly balancing excitation with inhibition in the cortex.

Besides activating only a small fraction of neurons in the somatosensory cortex (Brecht et al 2003), whisker deflections often evoke bursts of action potentials in layer 2/3 pyramidal cells (Svoboda et al 1997, Svoboda et al 1999). Our data show that high-frequency trains of action potentials in one or a few layer 2/3 pyramidal cells are ideally suited to recruit SOM interneurons. This suggests that in response to tactile stimuli, recurrent inhibitory circuits involving SOM interneurons may be specifically engaged in the balancing of cortical excitation, thereby contributing to the processing of sensory information.

Experimental Procedures

Slice preparation and recordings.

Parasagittal slices of primary somatosensory cortex (300–400 m) were prepared from Wistar rats 23 +/- 5 (mean +/- s.d.; n = 67) days of age. Animals were anesthetized in isoflurane or a mixture of ketamine and xylazine (4/1). Slices were cut with a Vibratome (DSK) in a chilled solution containing (in mM): 85 NaCl, 2.5 KCl, 1.25 NaH_2PO_4, 0.5 $CaCl_2$, 4 $MgCl_2$, 25 $NaHCO_3$, 75 sucrose, 25 glucose and 0.5 ascorbic acid (95% O_2, 5% CO_2) and incubated for 30 min at 34 °C in artificial cerebrospinal solution containing (in mM): 122

NaCl, 2.5 KCl, 1.25 NaH_2PO_4, 2 $CaCl_2$, 1 $MgCl_2$, 26 $NaHCO_3$, 25 glucose and 3 sodium pyruvate. Slices were stored in an interface chamber at room temperature until being placed in a submerged chamber for recordings at 32–34 °C.

Pyramidal cells in cortical layer 2/3 and interneurons in layers 2/3 and 5 were visually identified by infrared differential interference contrast videomicroscopy. Whole-cell patch-clamp recordings were performed using Multiclamp 700B and Axopatch 200A amplifiers (Axon Instruments) and digitized at 20 kHz. For recordings in pyramidal cells, pipettes (2–4 M) were filled with either (in mM) 122 potassium gluconate, 1 $MgCl_2$, 10 L-glutamic acid, 10 HEPES, 4 magnesium ATP, 0.3 sodium GTP, 10 sodium phosphocreatine and 5.5 biocytin (pH 7.25, 290 mOsm) 41 or 150 potassium gluconate, 1.5 $MgCl_2$, 5 HEPES, 1.1 EGTA, and 10 phosphocreatine (pH 7.25; 280–290 mOsm). For recordings in interneurons, internal solutions contained (in mM) 134 potassium gluconate, 1.5 $MgCl_2$, 10 HEPES, 0.1 EGTA, 3 magnesium ATP, 10 sodium phosphocreatine and 5.5 biocytin (pH 7.25, 290 mOsm). Trains of action potentials were elicited by somatic current injection (2 ms, 0.8–4 nA). Voltage measurements were not corrected for the experimentally determined liquid junction potential of 13 0.4 mV (n = 3). The drugs used were NBQX, gabazine (SR95531) and CGP54626 (all from Tocris Bioscience).

Data analysis

Amplitudes of recurrent IPSCs and inhibitory postsynaptic potentials were measured relative to baseline, over a window of 4–6-ms duration, 4 ms after the action potential, on averages of 6–100 sweeps. To determine the onset of recurrent IPSCs, a threshold criterion of 2 s.d. of the noise was applied to the averaged traces. To determine the shift in the onset of the recurrent IPSC when two pyramidal cells are spiking simultaneously, we compared the onset of the current recorded in PC1 when either PC2 or PC3 were spiking alone with the onset of the current recorded in PC1 when PC2 and PC3 were spiking simultaneously. Thus, this analysis does not include the set of triple recordings, in which neither the individual activity of PC2 nor of PC3 evoked a detectable inhibition of PC1.

Amplitudes of monosynaptic EPSCs and IPSCs in pyramidal cell–interneuron pairs were measured over a window of 0.5–2 ms around the peak of the averages of 5–50 sweeps. If the decay of the averaged response to the previous action potential in a train did not return to baseline, the decay of the previous signal was fitted with a single exponential and the baseline extrapolated.

Average values in the text and figures are expressed as mean s.e.m. unless stated otherwise. The Student's t-test was used for statistical comparisons. All traces are the average of more than ten sweeps, unless stated otherwise.

Connectivity

To determine P_{PI}, we first identified the recorded interneuron through the characteristic facilitating excitation it receives from a simultaneously recorded presynaptic pyramidal cell. Then, while keeping the identified interneuron, we recorded sequentially from additional pyramidal cells. Notably, P_{PI} was computed exclusively using the additional pairs—that is, it did not include the initial pair used to identify the interneuron.

Quantifying the recruitment of SOM interneurons.

We determined experimentally that when the number of active pyramidal cells increases from 1 to 2, the probability that a neighboring pyramidal cell is inhibited increases from 0.125 to 0.477. By assuming that SOM interneurons contact pyramidal cells statistically independently, we calculated that this increase in probability occurs because of a fivefold increase (N2/N1 = 4.85) in the number of SOM interneurons recruited. How much of this increase is contributed by cooperativity? To answer this question we determined the increase in probability of recruiting SOM interneurons receiving convergent excitation from two active pyramidal cells as compared to the probability of recruiting SOM interneurons receiving excitation from only one pyramidal cell as follows: assuming that pyramidal cells contact SOM interneurons statistically independently, we compute N1 and N2, the number of recruited SOM interneurons when one or two pyramidal cells are active, respectively, as

$$N_1 = F_1 P_{\mathrm{PI}} N$$

$$N_2 = [2F_1(P_{\mathrm{PI}} - (P_{\mathrm{PI}})^2) + F_{1\&2}(P_{\mathrm{PI}})^2]N$$

where F_1 is the probability of SOM interneurons being recruited in the subpopulation contacted by only one of the two pyramidal cells, and $F_{1\&2}$ is the probability of SOM interneurons being recruited in the subpopulation contacted by both pyramidal cells. P_{PI} is the probability that a pyramidal cell contacts a SOM interneuron (that is, connectivity) and is experimentally determined. N is the total number of SOM interneurons in the local circuit. Solving for $F_{1\&2}/F_1$ using N2/N1 (see above), we find that $F_{1\&2}/ F_1 = 11.83$.

The probability $F_{1\&2}$ consists of SOM interneurons that are contacted by both pyramidal cells but may be recruited by the independent activity of either pyramidal cell or the cooperative activity of both pyramidal cells; thus we subtract the fraction that is due to independent pyramidal cell activity $((F_{1\&2} - (2F_1 - (F_1)^2)/F_1)$. The probability of recruiting SOM interneurons through the cooperative activity of two pyramidal cells is approximately 9.8 times larger than if they were recruited by one pyramidal cell. This result is an underestimate because we approximated that the term $(F_1)^2$, which represents the probability of SOM interneurons recruited by both pyramidal cells independently, to be zero. Because $0 < F_1 \leq 1$, this underestimate is small.

Note that F_1 and $F_{1\&2}$ are the probabilities that an SOM interneuron is recruited at least once, given n trials. These probabilities are distinct from the

fraction of trials in which the spiking of a pyramidal cell recruits an SOM interneuron.

Model

We experimentally quantified the probability that pyramidal cells recruit inhibition onto neighboring 'target' pyramidal cells (see Results). This probability is a measure of the capacity of a pyramidal cell, given n trials, to at least once recruit at least one inhibitory circuit that impinges onto the target pyramidal cell. Note that this probability is distinct from the fraction of trials in which the spiking of a pyramidal cell evokes inhibition on a given target pyramidal cell.

Accordingly, the probability of recruiting an interneuron determined in the study is a measure of the capacity of a pyramidal cell, given n trials, to recruit an interneuron at least once, and not the fraction of trials in which the spiking of the pyramidal cell recruits a given interneuron.

Consequently, the activation curves (Fig 2.4) describe the maximal (not the average) fraction of interneurons that could be activated at any individual trial by the simultaneous spiking of n pyramidal cells.

We sought to design a simple model constrained by experimentally determined parameters (EPSP distribution and anatomical connectivity) for the purpose of (i) determining whether the experimentally observed increase in the probability of recruiting the SOM interneuron circuit can be explained based only on these parameters, and (ii) providing qualitative insight into how

connectivity, EPSP distribution and the number of active pyramidal cells affect the fraction of interneurons recruited.

Our model predicts the fraction of interneurons activated as a function of the number of spiking pyramidal cells. We created a distribution of EPSP amplitudes from paired recordings between connected pyramidal cells and SOM interneurons. The EPSP amplitude and standard deviation (s.d.) was measured after the third or tenth action potential. We then fit an alpha function ($B = xe^{-ax}$, $a = 0.58$) to this distribution of mean EPSP amplitudes (similar results were obtained using a Gaussian smoothed EPSP distribution). A fraction of these EPSP amplitudes are above threshold (as the activity of a single pyramidal cell is sufficient to recruit recurrent inhibition). This fraction is equal to the fraction of active interneurons. However, the distribution of average EPSP amplitudes does not take into account the trial-to-trial variability inherent in synaptic transmission. Namely, some EPSPs may fluctuate such that in only a minority of trials they are suprathreshold while their average remains subthreshold. To ensure that the model design accounted for a pyramidal cell's capacity for recruiting inhibition (rather then just the average behavior), the average EPSP s.d. (s.d. = 1.2 mV) was added to the distribution of EPSP amplitudes. Based on this shifted distribution, we obtained the maximum fraction of interneurons above threshold for any individual trial. To create D1 (see Fig 2.4b), the connectivity between pyramidal cells and interneurons was introduced into the distribution by adding zeros to B (that is, if $P_{PI} = 0.29$, then 0.71 of D1 must be zeros). Finally, the distribution of EPSP amplitudes when

two pyramidal cells are spiking (D2) was generated from the linear sum of two EPSPs picked randomly out of D1 (see gray trace in Fig 2.4b, left). We used the same method to generate D3–DN.

On the basis of our experiments, we deduced that two pyramidal cells have the capacity to recruit five times as many interneurons as one pyramidal cell can. These data can be used to determine the threshold (T) for interneuron activity in our model. The ratio of the integral of D2 > T to D1 > T (that is, $\sum_T^\infty$ D2 / $\sum_T^\infty$ D1) should equal 4.85. A threshold, T, of 11.3 mV above resting membrane potential is consistent with this fivefold increase (Fig 2.4b, left). This T is consistent with the range of experimentally measured thresholds for SOM interneurons30. We then used this threshold, together with D1–DN, to predict the fraction of interneurons recruited when more than two pyramidal cells are active (Fig 2.4b,c). Clearly, as more pyramidal cells simultaneously excite interneurons, reductions in driving force and membrane resistance will result in sublinear summation of EPSPs. So our model will underestimate the number of active pyramidal cells required to fully activate the interneuron population.

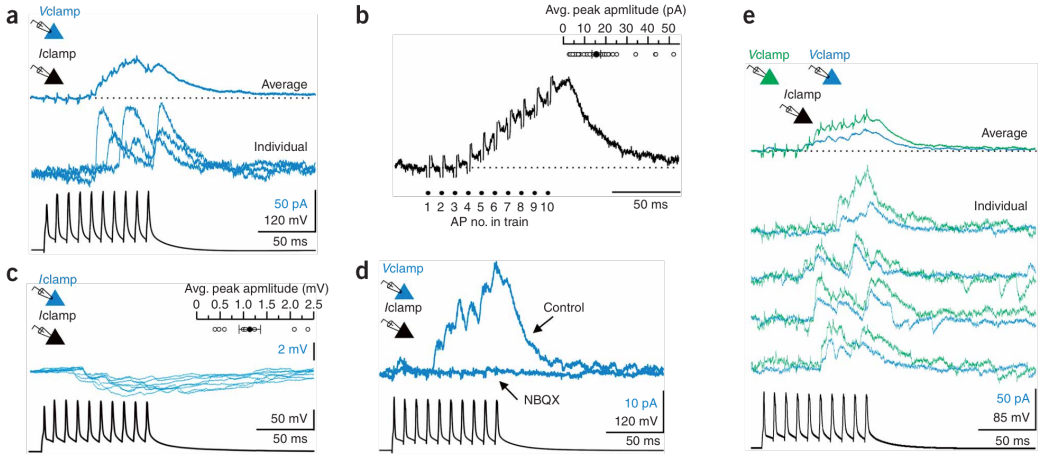

Fig 2.1 Unitary recurrent inhibitory circuits

(A) The spiking (ten action potentials at 100 Hz) of a layer 2/3 pyramidal cell (black trace) evokes outward currents in a simultaneously recorded target layer 2/3 pyramidal cell (blue traces; VH, -40 mV). The top trace is the average of 15 sweeps, 3 of which are shown superimposed in the middle. Upper left, schematic of the recording configuration. V clamp, voltage clamp; I clamp, current clamp.

(B) Summary current, averaged over all experiments (n = 38), recorded in layer 2/3 pyramidal cells in response to a train of action potential in a neighboring pyramidal cell (the dots indicate the time of the spikes). Individual currents were normalized by their peak amplitudes. Inset, peak current for each recurrent IPSC (n = 38; open symbols) and the averaged peak of all experiments (solid symbol). (C) Same configuration illustrated in a (different pair), except that target pyramidal cell is recorded in current clamp (blue traces; Vm = -52 mV). Inset, peak hyperpolarization for nine similar experiments (open symbols) and the average of all experiments (solid symbol).

(D) Same recording configuration illustrated in a (different pair). Application of the AMPA/kainate receptor antagonist NBQX (10 M) completely abolishes the outward current.

(E) Simultaneous recording from three layer 2/3 pyramidal cells. The spiking of one of the cells (black trace) evokes outward current in the two other pyramidal cells (blue and green traces; VH, -40 mV). The top traces are the average of 23 sweeps. Lower traces show four individual sweeps recorded simultaneously in the green and blue pyramidal cells. Black–blue pair same as in d.

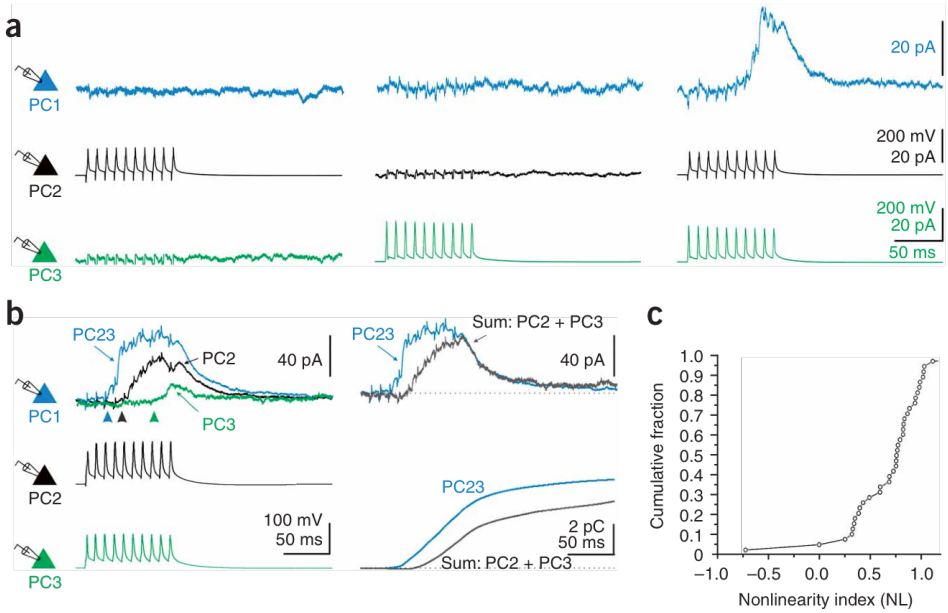

Fig 2.2 Supralinear increase of inhibition

(A) Simultaneous recording from three layer 2/3 pyramidal cells (PC1, blue; PC2, black; PC3, green). Left, a train of action potentials in PC2 elicits no current in PC1 nor PC3 (VH, -40 mV). Middle, a train of action potentials in PC3 elicits no current in PC1 or PC2 (VH, -40 mV). Right, simultaneous trains of action potentials in PC2 and PC3 elicit an outward current in PC1. All current traces are averages of multiple sweeps.

(B) Same recording configuration as in a (different cells). Left, the spiking of either PC2 or PC3 alone elicits outward currents in PC1. Note the earlier onset of inhibition in PC1 (blue trace) when PC2 and PC3 are spiking simultaneously (the PC2-PC1 pair is the same one as in Fig 2.1a). Right top, gray trace: algebraic sum of the currents elicited in PC1 in response to the spiking of PC2 and PC3 alone. Blue trace, outward current elicited in response to the simultaneous spiking of PC2 and PC3. Right bottom, running integral of the two currents illustrated on top. Note that the inhibitory charge in response to the simultaneous spiking of PC2 and PC3 is larger than the inhibitory charge of the algebraic sum of the responses of PC1 to the spiking of PC2 and PC3 alone. All current traces are averages of multiple sweeps.

(C) Cumulative distribution of the nonlinearity index (see Results for details) for 38 similar experiments. Note that most values are larger than 0, indicating supralinear increase in recurrent inhibition when PC2 and PC3 are spiking simultaneously.

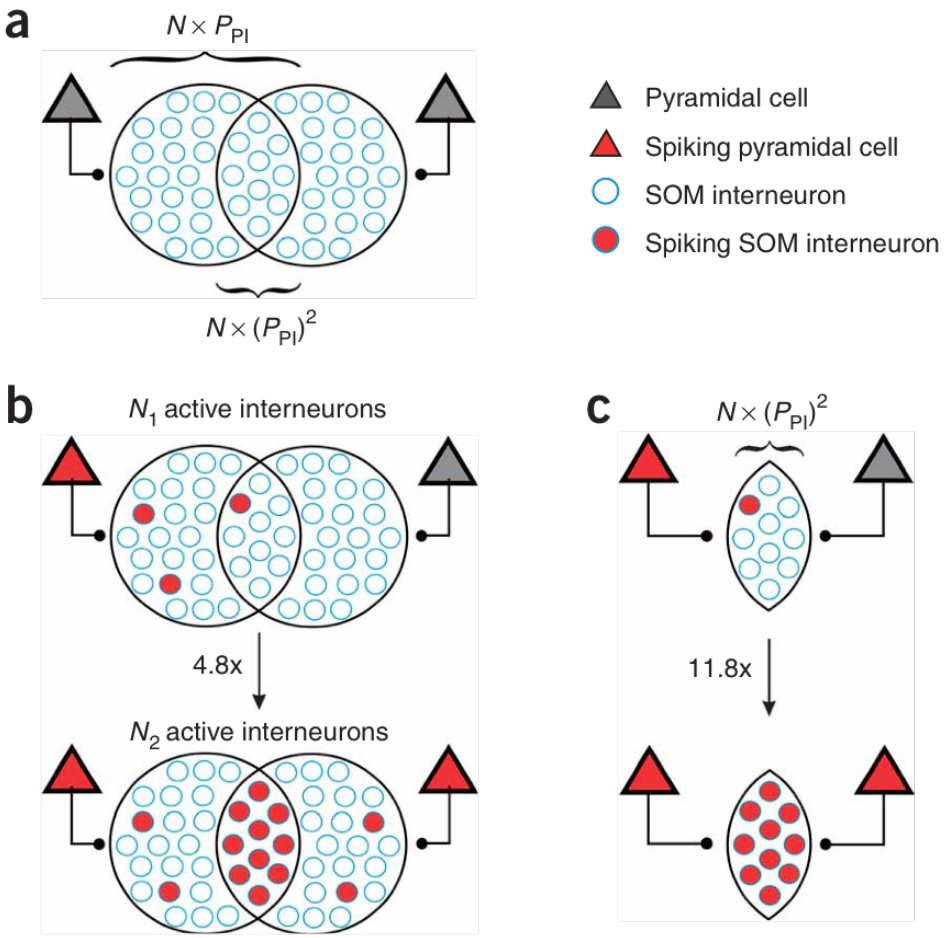

Fig 2.3 Increase in the recruitment of somatostatin-expressing interneurons

(A) Schematic of the projection of two pyramidal cells onto SOM interneurons. N is the total population of SOM interneurons; P_{PI} is the probability of a pyramidal cell contacting a SOM interneuron; NxP_{PI} is the population of SOM interneurons contacted by one layer 2/3 pyramidal cell; and $Nx(P_{PI})^2$ is the population of interneurons targeted by both pyramidal cells. The number of interneurons assigned to each population is for illustration purpose only.

(B) Top, when only one of the two pyramidal cells is spiking, the N1 SOM interneurons are recruited (filled red circles). Bottom, when two pyramidal cells are spiking, almost five times more interneurons (N2) are recruited.

(C) Within the population of interneurons receiving convergent input from two pyramidal cells ($Nx(P_{PI})^2$), the fraction that is recruited in response to the activity of two pyramidal cells (bottom) is 11.8 times larger than the one that is recruited by one pyramidal cell only (top; see Experimental Procedures).

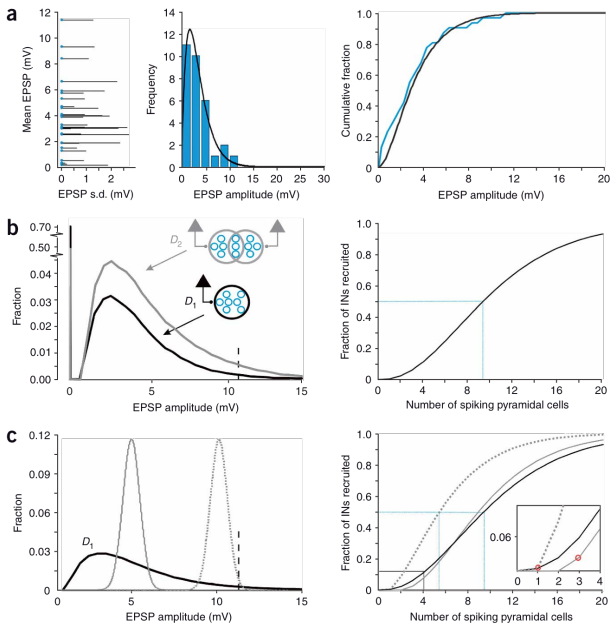

Fig 2.4 Model describing range and sensitivity of recurrent inhibition.

(A) Left, mean EPSP amplitude recorded in SOM interneurons after the tenth action potential evoked in the presynaptic pyramidal cell, plotted against the standard deviation (s.d.) of the EPSP, for each of the 31 unitary connections. Middle, distribution of EPSP amplitudes (blue bars) and alpha function (black curve) that fits the distribution. Right, cumulative distribution of EPSP amplitudes (blue line) and alpha function (black line).

(B) Left, distribution of EPSP amplitudes evoked by one pyramidal cell (D1: black line) or two pyramidal cells (D2: gray line) in the interneuron populations contacted by one pyramidal cell or by either of two pyramidal cells, respectively. Values at zero represent the fraction of unconnected interneurons (black: 1 - P_{PI}, gray: 1 - (1 - P_{PI})^2). The threshold for action potential generation (11.3 mV above resting potential) is shown by a dashed line. Right, prediction of the fraction of recruited SOM interneurons (INs) plotted against the number of active pyramidal cells (interneuron activation curve). The blue dotted lines illustrate half activation.

(C) Left: black line, D1 (same as in b; values at zero have been cut; mean 4.6 mV, s.d. 2.8 mV); continuous gray line, EPSP distribution with same mean but small s.d. (mean 4.6 mV; s.d. 0.5 mV); dotted gray line, EPSP distribution with large mean (mean 10.3 mV, s.d. 0.5 mV), yet same fraction of EPSPs above threshold as D1. Right: interneuron activation curves for the three EPSP distributions shown on the left (black trace same as in b). Note the faster saturation of the activation curve for the EPSP distribution with a large mean (dotted gray trace) and the right-shifted onset for the EPSP distribution with a small s.d. (continuous gray trace). The blue dotted lines illustrate half activation. Inset, the minimum number of pyramidal cells required to activate inhibitory circuit for experimental EPSP distribution is 1, as compared to 3 for the normal distribution of the same mean with a smaller s.d.

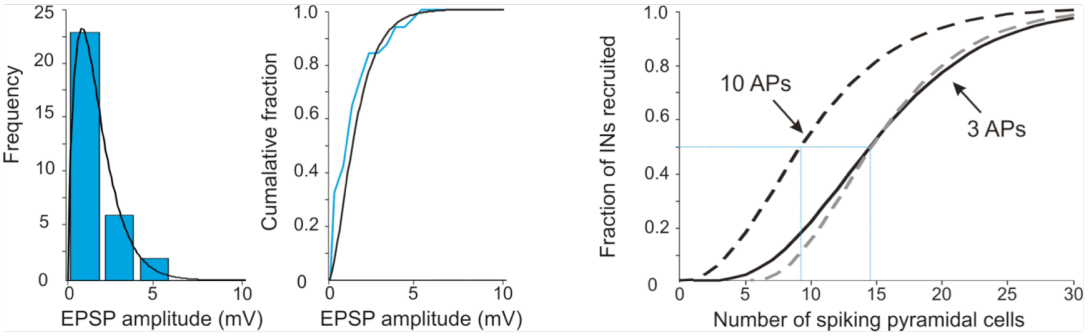

Fig 2.5 Model describing range and sensitivity of recurrent inhibition with 1, 3 or 10 action potentials.

Left: Distribution of EPSP amplitudes (blue bars) recorded in SOM interneurons after the 3rd action potential in the presynaptic pyramidal cell and alpha function (black curve) describing the distribution. Middle: Cumulative distribution of EPSP amplitudes (blue line) and alpha function (black line). Right: Prediction of the fraction of recruited SOM interneurons plotted against the number of active pyramidal cells (interneuron activation curve) when pyramidal cells are firing 3 action potentials (APs; continuous black line) or when they are firing 10 action potentials (dashed black line; from Fig 2.4b). The blue dotted line illustrates half activation. The gray dashed line illustrates the activation curve in response to 10 action potentials, shifted to match half maximal activation of the activation curve in response to three action potentials. Note the slight change

Appendix

Recurrent inhibition via somatostatin-expressing interneurons

Which type of inhibitory interneuron generates this recurrent inhibition in layer 2/3 in response to the activity of one or a few pyramidal cells? Any interneuron receiving excitatory inputs from and projecting back to layer 2/3 pyramidal cells could, in principle, participate in the observed recurrent inhibition. Through recordings from pairs of connected pyramidal cells and interneurons, we subdivided the interneuron population into two broad categories: those that received unitary EPSCs that depressed in response to a train of spikes in pyramidal cells and those that received facilitating EPSCs. Both categories of inhibitory neurons, those receiving facilitating inputs (fRS cells) and those receiving depressing excitatory inputs (fast spiking, FS and depressing-regular spiking dRS cells), formed inhibitory synapses with layer 2/3 pyramidal cells (average unitary IPSC amplitude mediated by fRS cells onto pyramidal cells, 19.14 16.4 pA, n = 31; average unitary IPSC amplitude mediated by FS and dRS cells (pooled) onto pyramidal cells, 44.4 10.1 pA, n = 21), confirming their potential involvement in the observed recurrent inhibition.

fRS cells receiving inputs from and projecting back to layer 2/3 pyramidal cells (not necessarily the same pyramidal cell they received input from) were found in both layers 2/3 and 5 (layer 2/3 pyramidal cells to layer 2/3 fRS cells, indicating that recurrent inhibitory circuits involving this category of interneurons can cross cortical layers. In contrast, FS and dRS cells receiving input from and projecting back to layer 2/3 pyramidal cells were found exclusively in layer 2/3.

fRS cells invariably expressed somatostatin (SOM; 10 of 10 processed neurons) Hence, we refer to fRS cells as SOM interneurons. SOM-positive labeling was never observed in FS and dRS cells.

To determine which of the two categories of interneurons mediates the observed recurrent inhibition, we reasoned as follows: the timing of spikes elicited in the interneuron in response to a train of action potentials in a pyramidal cell must account for the time course of the inhibitory current recorded in the target pyramidal cell. The suitability of the candidate interneuron category can thus be evaluated by convolving the distribution of spike times with the average unitary IPSC generated onto pyramidal cells. This convolution should match the time course of the observed recurrent inhibition.

Through paired recordings, we determined the distribution of spike times in the two interneuron categories in response to a train of action potentials in pyramidal cells (see Methods). The convolution of the distribution of spike times triggered in SOM interneurons (Fig 2.Aa,b) with the unitary IPSC (10–90% rise time of 2.3 0.2 ms, n = 19; decay time constant 12.12 1.9 ms, n = 20) that they generate onto pyramidal cells resulted in an outward current with a time course that was markedly similar to that of the inhibition observed in pyramidal cells in response to a train of action potentials triggered in a neighboring pyramidal cell (Fig 2.Ac). In contrast, the distribution of spike times of interneurons receiving depressing excitatory inputs peaked much earlier (Fig 2.Ad), indicating that they are recruited at the onset of a train of action potentials12. Accordingly, the convolution of this spike time distribution with the unitary IPSC that these

interneurons generate on layer 2/3 pyramidal cells (10–90% rise time 1.0 0.1 ms, n = 18; decay time 9.4 1.3 ms, n = 14) resulted in an outward current with a much earlier onset and peak than the observed one (Fig 2.Ae).

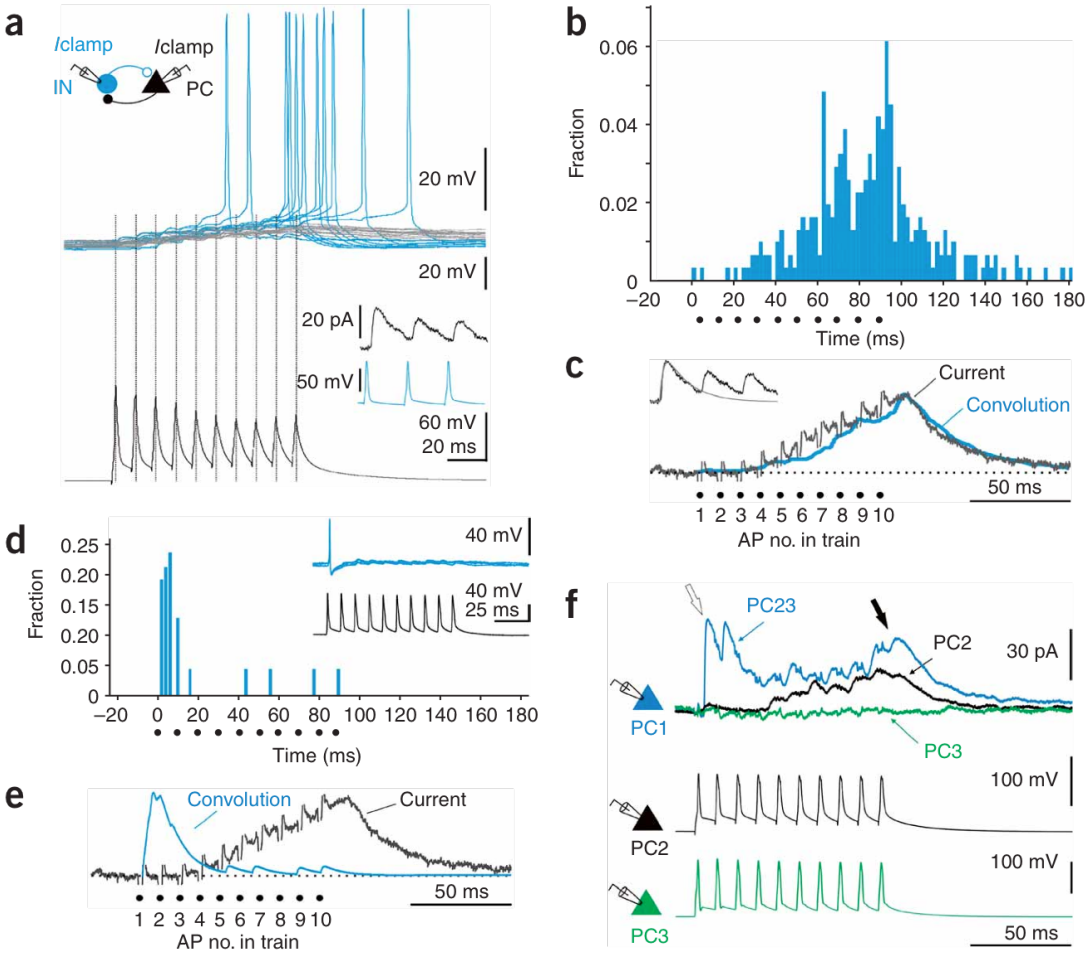

Fig 2.A Spike timing of somatostatin-positive interneurons determines the time course of recurrent inhibition.

(a) A train of spikes at 100 Hz in a layer 2/3 pyramidal cell (black trace) elicits action potentials in an SOM interneuron (threshold for action potential generation was achieved in some (blue races; 12 superimposed sweeps) but not all (gray traces, 14 superimposed sweeps) trials (Vm interneuron, -63 mV)). Inset, the interneuron was reciprocally connected with the pyramidal cell: spiking of the interneuron (blue trace) triggered outward currents in the pyramidal cell (black trace). (b) Summary graph of the distribution of spike times in SOM interneurons in response to trains of action potentials at 100Hz in the presynaptic pyramidal cells (n = 12). (c) The blue trace illustrates the result of the convolution of the spike time distribution (in b) with a fit to an average unitary IPSC (sum of two exponential functions; rise, 1.7 ms; decay, 11 ms). The convolution is superimposed onto the time course, averaged over all experiments, of the outward current elicited by the spiking of a single pyramidal cell onto a neighboring pyramidal cell (gray trace, from Fig 2.1b). Note the similarity of the rising and decaying phase of the two currents. Inset: gray trace, standard IPSC; black trace, unitary IPSC from a. (d) Summary graph of the distribution of spike times in interneurons receiving depressing inputs in response to trains of action potentials at 100 Hz in the presynaptic pyramidal cells (n = 2). Inset, a train of spikes at 100 Hz in a layer 2/3 pyramidal cell (black trace) elicits action potentials in an interneuron receiving depressing inputs (blue traces; five superimposed sweeps where threshold for action potential generation was achieved (Vm interneuron, -63 mV)). (e) Convolution (blue trace) of the spike distribution (in d) with the fit of an average IPSC (sum of two exponential functions; rise, 0.8 ms; decay, 9.4 ms). The convolution is superimposed onto the time course, averaged over all experiments, of the outward current elicited by the spiking of a single pyramidal cell onto a neighboring pyramidal cell (gray trace, from Fig 2.1b). Note the very different rising and decaying phases of the two currents. (f) Simultaneous recording from three layer 2/3 pyramidal cells (blue, PC1; black, PC2; green, PC3). A train of spikes in PC2 alone leads to inhibition with late onset in PC1 (VH, -40 mV; black traces), similar to that illustrated in Figures 1 and 2. A train of spikes in PC3 alone leads to no inhibition in PC1 (green traces). A simultaneous train of spikes in PC2 and PC3 leads to the appearance of an early component of inhibition (open arrow) followed by the late component (black arrow) in PC1 (blue trace).

Acknowledgements

This chapter contains reprinted material as it appears Supralinear increase of recurrent inhibition during sparse activity in the somatosensory cortex, Kapfer C, Glickfeld LL, Atallah BV & Scanziani M, Nature Neuroscience 2007 Jun;10(6), 743 - 753. The dissertation author was an author for this material contributing analysis and design the models. Experiments were performed by authors C Kapfer, L L Glickfeld, & M Scanziani. Permission reprint of material is granted by all original authors.

References

1. Ferster,D. & Jagadeesh,B.EPSP-IPSPinteractionsincatvisualcortexstudiedwithin vivo whole-cell patch recording. J. Neurosci. 12, 1262–1274 (1992).

2. Wehr,M. & Zador,A.M.Balancedinhibitionunderliestuningandsharpensspiketiming in auditory cortex. Nature 426, 442–446 (2003).

3. Zhu,J.J. & Connors,B.W.Intrinsicfiringpatternsandwhisker-evokedsynapticresponses of neurons in the rat barrel cortex. J. Neurophysiol. 81, 1171–1183 (1999).

4. Wilent, W.B. & Contreras, D. Synaptic responses to whisker deflections in rat barrel cortex as a function of cortical layer and stimulus intensity. J. Neurosci. 24, 3985–3998 (2004).

5. Douglas, R.J., Martin, K.A. & Whitteridge, D. An intracellular analysis of the visual responses of neurones in cat visual cortex. J. Physiol. (Lond.) 440, 659–696 (1991).

6. Anderson, J.S., Carandini, M. & Ferster, D. Orientation tuning of input conductance, excitation, and inhibition in cat primary visual cortex. J. Neurophysiol. 84, 909–926 (2000).

7. Wilent,W.B.&Contreras,D.Dynamicsofexcitationandinhibitionunderlyingstimulus selectivity in rat somatosensory cortex. Nat. Neurosci. 8, 1364–1370 (2005).

8. Gabernet,L.,Jadhav,S.P.,Feldman,D.E.,Carandini,M.&Scanziani,M.Somatosensory integration controlled by dynamic thalamocortical feed-forward inhibition. Neuron 48, 315–327 (2005).

9. Dykes, R.W., Landry, P., Metherate, R. & Hicks, T.P. Functional role of GABA in cat primary somatosensory cortex: shaping receptive fields of cortical neurons. J. Neuro- physiol. 52, 1066–1093 (1984).

10. Kyriazi, H.T., Carvell, G.E., Brumberg, J.C. & Simons, D.J. Quantitative effects of GABA and bicuculline methiodide on receptive field properties of neurons in real and simulated whisker barrels. J. Neurophysiol. 75, 547–560 (1996).

11. Sillito, A.M. The contribution of inhibitory mechanisms to the receptive field properties of neurones in the striate cortex of the cat. J. Physiol. (Lond.) 250, 305–329 (1975).

12. Pouille, F. & Scanziani, M. Routing of spike series by dynamic circuits in the hippocampus. Nature 429, 717–723 (2004).

13. Shu, Y., Hasenstaub, A. & McCormick, D.A. Turning on and off recurrent balanced cortical activity. Nature 423, 288–293 (2003).

14. Carandini, M., Heeger, D.J. & Movshon, J.A. Linearity and normalization in simple cells of the macaque primary visual cortex. J. Neurosci. 17, 8621–8644 (1997).

15. Douglas, R.J. & Martin, K.A. A functional microcircuit for cat visual cortex. J. Physiol. (Lond.) 440, 735–769 (1991).

16. Pinto, D.J., Hartings, J.A., Brumberg, J.C. & Simons, D.J. Cortical damping: analysis of thalamocortical response transformations in rodent barrel cortex. Cereb. Cortex 13, 33–44 (2003).

17. Pinto, D.J., Brumberg, J.C. & Simons, D.J. Circuit dynamics and coding strategies in rodent somatosensory cortex. J. Neurophysiol. 83, 1158–1166 (2000).

18. Brecht, M., Roth, A. & Sakmann, B. Dynamic receptive fields of reconstructed pyramidal cells in layers 3 and 2 of rat somatosensory barrel cortex. J. Physiol. (Lond.) 553, 243–265 (2003).

19. Kozloski, J., Hamzei-Sichani, F. & Yuste, R. Stereotyped position of local synaptic targets in neocortex. Science 293, 868–872 (2001).

20. Thomson, A.M. & Deuchars, J. Synaptic interactions in neocortical local circuits: dual intracellular recordings in vitro. Cereb. Cortex 7, 510–522 (1997).

21. Reyes, A. et al. Target-cell-specific facilitation and depression in neocortical circuits. Nat. Neurosci. 1, 279–285 (1998).

22. Galarreta, M., Erdelyi, F., Szabo, G. & Hestrin, S. Electrical coupling among irregular- spiking GABAergic interneurons expressing cannabinoid receptors. J. Neurosci. 24, 9770–9778 (2004).

23. Blatow, M. et al. A novel network of multipolar bursting interneurons generates theta frequency oscillations in neocortex. Neuron 38, 805–817 (2003).

24. Gupta, A., Wang, Y. & Markram, H. Organizing principles for a diversity of GABAergic interneurons and synapses in the neocortex. Science 287, 273–278 (2000).

25. McCormick, D.A., Connors, B.W., Lighthall, J.W. & Prince, D.A. Comparative electro- physiology of pyramidal and sparsely spiny stellate neurons of the neocortex. J. Neurophysiol. 54, 782–806 (1985).

26. Kawaguchi, Y. & Kubota, Y. GABAergic cell subtypes and their synaptic connections in rat frontal cortex. Cereb. Cortex 7, 476–486 (1997).

27. Beierlein, M., Gibson, J.R. & Connors, B.W. Two dynamically distinct inhibitory networks in layer 4 of the neocortex. J. Neurophysiol. 90, 2987–3000 (2003).

28. Gibson, J.R., Beierlein, M. & Connors, B.W. Two networks of electrically coupled inhibitory neurons in neocortex. Nature 402, 75–79 (1999).

29. Galarreta, M. & Hestrin, S. Frequency-dependent synaptic depression and the balance of excitation and inhibition in the neocortex. Nat. Neurosci. 1, 587–594 (1998).

30. Wang, Y. et al. Anatomical, physiological and molecular properties of Martinotti cells in the somatosensory cortex of the juvenile rat. J. Physiol. (Lond.) 561, 65–90 (2004).

31. Svoboda, K., Denk, W., Kleinfeld, D. & Tank, D.W. In vivo dendritic calcium dynamics in neocortical pyramidal neurons. Nature 385, 161–165 (1997).

32. Svoboda, K., Helmchen, F., Denk, W. & Tank, D.W. Spread of dendritic excitation in layer 2/3 pyramidal neurons in rat barrel cortex in vivo. Nat. Neurosci. 2, 65–73 (1999).

33. Haider, B., Duque, A., Hasenstaub, A.R. & McCormick, D.A. Neocortical network activity in vivo is generated through a dynamic balance of excitation and inhibition. J. Neurosci. 26, 4535–4545 (2006).

34. Chu, Z., Galarreta, M. & Hestrin, S. Synaptic interactions of late-spiking neocortical neurons in layer 1. J. Neurosci. 23, 96–102 (2003).

35. Yoshimura, Y. & Callaway, E.M. Fine-scale specificity of cortical networks depends on inhibitory cell type and connectivity. Nat. Neurosci. 8, 1552–1559 (2005).

36. Rozov, A., Jerecic, J., Sakmann, B. & Burnashev, N. AMPA receptor channels with long- lasting desensitization in bipolar interneurons contribute to synaptic depression in a novel feedback circuit in layer 2/3 of rat neocortex. J. Neurosci. 21, 8062–8071 (2001).

37. Thomson, A.M., West, D.C., Wang, Y. & Bannister, A.P. Synaptic connections and small circuits involving excitatory and inhibitory neurons in layers 2–5 of adult rat and cat neocortex: triple intracellular recordings and biocytin labelling in vitro. Cereb. Cortex 12, 936–953 (2002).

38. Ma, Y., Hu, H., Berrebi, A.S., Mathers, P.H. & Agmon, A. Distinct subtypes of somatostatin-containing neocortical interneurons revealed in transgenic mice. J. Neurosci. 26, 5069–5082 (2006).

39. Faire´ n, A., DeFelipe, J. & Regidor, J. Nonpyramidal neurons: general account. in Cellular Components of the Cerebral Cortex (eds. Peters, A. & Jones, E.G.) 201–254 (Plenum, New York, 1984).

40. Azouz, R. & Gray, C.M. Dynamic spike threshold reveals a mechanism for synaptic coincidence detection in cortical neurons in vivo. Proc. Natl. Acad. Sci. USA 97, 8110–8115 (2000).

41. Biro, A.A., Holderith, N.B. & Nusser, Z. Quantal size is independent of the release probability at hippocampal excitatory synapses. J. Neurosci. 25, 223–232 (2005).

Chapter 3. Instantaneous modulation of gamma oscillation frequency by balancing excitation with inhibition

Abstract

Neurons recruited for local computations exhibit rhythmic activity at gamma frequencies. The amplitude and frequency of these oscillations are continuously modulated depending on stimulus and behavioral state. This modulation is believed to crucially control information flow across cortical areas. Here we report that in the rat hippocampus gamma oscillation amplitude and frequency vary rapidly, from one cycle to the next. Strikingly, the amplitude of one oscillation predicts the interval to the next. Using in vivo and in vitro whole-cell recordings, we identify the underlying mechanism. We show that cycle-by-cycle fluctuations in amplitude reflect changes in synaptic excitation spanning over an order of magnitude. Despite these rapid variations, synaptic excitation is immediately and proportionally counterbalanced by inhibition. These rapid adjustments in inhibition instantaneously modulate oscillation frequency. So, by rapidly balancing excitation with inhibition, the hippocampal network is able to swiftly modulate gamma oscillations over a wide band of frequencies.

Introduction

One of the most prominent characteristics of cortical activity is the rhythmic fluctuation of large neuronal populations in synchrony. Such oscillations occur over a wide range of frequencies, from 0.1 Hz to >100 Hz depending on the behavioral state of the animals (Buzsaki, 2006; Steriade, 2006). Gamma oscillations are a particularly prominent form of rhythmic activity that results from the synchronous fluctuation of the membrane potential of cortical neurons at frequencies between 20 and 60 Hz (Jagadeesh et al., 1992; Penttonen et al., 1998; Soltesz and Deschênes, 1993). These gamma rhythms occur during wakefulness, attentive behavior (Bragin et al., 1995; Chrobak and Buzsaki, 1998; Fries et al., 2001; Womelsdorf et al., 2005) as well as in some anesthetized states (Gray and Singer, 1989; Jones and Barth, 1997; Neville and Haberly, 2003). They are evoked by external stimuli in sensory cortices (Gray and Singer, 1989; Jones and Barth, 1997; Neville and Haberly, 2003), by exploratory behavior in the hippocampus (Bragin et al., 1995), and precede motor responses in premotor areas (Pesaran et al., 2002).

Activity at gamma frequencies is thought to play a major role in the propagation of information across cortical areas (Engel et al., 2001; Sirota et al., 2008; Womelsdorf et al., 2007). By synchronizing the spiking activity of multiple neurons, gamma oscillations may allow these neurons to efficiently cooperate in the recruitment of their postsynaptic targets thereby facilitating the transmission of information (Bruno and Sakmann, 2006; Womelsdorf et al., 2005). Indeed, odor evoked oscillations triggered in the olfactory bulb are effectively

transmitted all the way through olfactory and entorhinal cortex to the hippocampus (Martin et al., 2007).

Synchronous spiking during gamma activity may also regulate the efficiency by which two distinct groups of neurons recruit a third group to which they both project, thereby contributing to the merger, or “binding,” of information originating from distinct regions (Engel et al., 2001). When two groups of neurons oscillate synchronously or in-phase, they can act synergistically to recruit target neurons by exciting them simultaneously. However, even subtle changes in the phase or frequency of the oscillations in one group with respect to the other may dramatically alter this synchrony and the subsequent recruitment of downstream target neurons (Fell et al., 2001; Schoffelen et al., 2005). The transmission of information during gamma oscillations is therefore a dynamic process that depends on the precise timing of the oscillation.

Even within a specific cortical location, the instantaneous frequency of gamma oscillations changes from one moment to the next (Bragin et al., 1995; Womelsdorf et al., 2007). This ongoing modulation in oscillation frequency (or phase) affects the precise timing of neuronal spiking within that cortical location, thereby altering the efficacy with which information is transmitted to downstream regions. In fact, a recent study has shown that the precise phase of oscillations can determine whether or not activity is effectively transmitted between cortical areas (Womelsdorf et al., 2007).

Despite the importance of frequency modulation in the transmission of information across cortical areas, little is known about the mechanisms that

drive rapid changes in oscillation frequency. Here we show that in the hippocampus the CA3 network maintains inhibition proportional to excitation during each oscillation cycle. This ongoing adjustment in the level of inhibition results in an instantaneous modulation of oscillation frequency. Thus, changes in inhibitory synaptic activity control the instantaneous oscillation frequency on a cycle-by-cycle basis.

Results

Oscillation Amplitude Predicts Instantaneous Oscillation Frequency

To determine how frequency and amplitude of hippocampal activity vary in vivo, we recorded the local field potential (LFP) in area CA3 of anesthetized rats (Fig 3.1). A prominent feature of the recorded activity was periodicity at gamma frequencies (Bragin et al., 1995; Csicsvari et al., 2003). We observed robust rhythmic activity ranging from 26 to 41 Hz (mean frequency = 34.8 Hz; sd = 5.3 Hz, n = 6 rats) corresponding to gamma oscillations. While this gamma rhythm was an ongoing feature of the LFP in CA3, its precise amplitude and frequency varied substantially from one oscillation cycle to the next (Fig 3.1A, B).

The interval between individual oscillation cycles (interevent interval, IEI) varied from 12 ms to over 40 ms, corresponding to instantaneous frequencies spanning a large frequency band (25-80 Hz). Strikingly however, the changes in amplitude and frequency were not independent. We observed a substantial decrease in the instantaneous frequency of rhythmic activity following large

oscillation cycles. The amplitude of an oscillation cycle was strongly correlated with the latency to the subsequent cycle ($r = 0.51 \pm 0.03$, $n = 6$ rats, Fig 3.1B). Consistent with oscillation amplitude predicting the latency to the next cycle the amplitude of an oscillation cycle was only weakly correlated with the latency to the previous cycle ($r = 0.18$, $n = 6$ rats, discussed further in Appendix). The correlation between amplitude and interval was not unique to activity recorded in anesthetized rats. In fact, a similar correlation existed during gamma activity recorded in area CA3 of the freely-moving rat ($r = 0.46$, Fig 3.6). These results demonstrate that the amplitude of an oscillation cycle predicts the instantaneous oscillation frequency.

In order to determine whether these rapid fluctuations in LFP amplitude and frequency reflect changes in the spike output of the CA3 network, we recorded multi-unit spiking activity via extracellular electrodes placed in the pyramidal cell layer of anesthetized rats. Fluctuations in LFP amplitude were accompanied by changes in spike rate (Fig 3.1E and 3.6). Spikes were precisely phase-locked to the LFP oscillation as demonstrated by the peri-oscillation time histogram (POTH, Fig 3.1D) (Bragin et al., 1995; Csicsvari et al., 2003; Tukker et al., 2007) and spike-LFP coherence (Fig 3.7). Furthermore, despite large ongoing changes in oscillation amplitude, the time window in which spikes occurred was equally narrow during both large and small amplitude cycles (full-width at half maximum, FWHM, of the POTH: 6.3 ± 1.0 ms for small cycles and 7.1 ± 1.4 ms for large cycles, $n = 6$ rats; Fig 3.1E). Taken together these data demonstrate that during gamma activity the correlated

fluctuations in amplitude and frequency of the LFP are precisely reported by the number and the timing, respectively, of spikes generated in the CA3 network.

What cellular mechanisms underlie the correlation between amplitude and instantaneous frequency of the LFP during gamma oscillations? To monitor synaptic events during gamma oscillations, we performed a series of experiments in acute hippocampal brain slices. First, we verified that oscillations generated in vitro also exhibited correlated changes in amplitude and frequency. Ongoing gamma oscillations were generated in area CA3 by bath application of low concentrations of kainic acid (100-500 nM) (Hájos et al., 2000) and recorded by placing a field electrode in the stratum radiatum of the CA3 region (Fig 3.2A). A distinct spectral peak in LFP activity occurred at frequencies between 25 Hz and 40 Hz (mean frequency = 29.8 Hz; sd = 2.4 Hz) as observed in vivo. Furthermore, rhythmic activity in vitro also exhibited large changes in both amplitude and frequency (Fig 3.2A). Finally, as observed in vivo, during rhythmic activity generated in vitro the amplitude of a cycle was a good predictor of the interval to the next cycle ($r = 0.69 \pm 0.02$, $n = 6$ slices; Fig 3.2B. This correlation was not the spurious result of constructive and destructive summation of individual LFP oscillations; see Appendix and Fig 3.8).

Balanced Fluctuations of Excitation and Inhibition Underlie Variation in Oscillation Amplitude

In order to determine what synaptic events underlie gamma oscillations we performed whole-cell voltage-clamp recordings from CA3 pyramidal cells

while monitoring the LFP with an electrode placed in the stratum radiatum. Pyramidal cells were voltage clamped at either the reversal potential for inhibition (VH ≈ -85 mV) or for excitation (VH ≈ 0 mV) to isolate excitatory postsynaptic currents (EPSCs) and inhibitory postsynaptic currents (IPSCs), respectively (Fig 3.9). Both excitatory and inhibitory synaptic currents occurred at gamma frequencies, as shown by their power spectra, and exhibited a pronounced peak in coherence with the simultaneously recorded LFP within the gamma frequency band (Fig 3.9). While the rise time of excitatory and inhibitory currents during each oscillation cycle (computed using an oscillation triggered average, Fig 2C) were similar (10-90% rise-time EPSC: 4.0 ± 0.5, IPSC 4.3 ± 0.6, t-test $p = 0.7$, $n = 6$) the decay time of IPSCs was ~ 50% longer then that of EPSCs (mono-exponential fit EPSC: 8.5 ± 1 ms, IPSC: 13.2 ± 2.5 ms, t-test $p < 0.003$; $n = 6$).

Importantly, the amplitude of both EPSCs and IPSCs exhibited large cycle-to-cycle fluctuations that were correlated with the LFP oscillation amplitude on a cycle-by-cycle basis ($r = 0.63 \pm 0.05$; $n = 8$ pairs and $r = 0.65 \pm 0.07$; $n = 8$ pairs respectively, Fig 3.9). This suggests that cycle-by-cycle variation in excitatory and inhibitory currents may not be unique to each cell but common across the population. To address this possibility, we recorded EPSCs simultaneously in two neighboring CA3 pyramidal cells (Fig 3.10). We found that a substantial fraction of variation in EPSC amplitude was common to both cells ($r = 0.54 \pm 0.10$; $n = 5$ pairs, Fig 3.10). Similarly when both pyramidal cells were voltage clamped at the reversal potential for excitation, we observed a

strong correlation between the amplitude of simultaneous IPSCs (r = 0.77 ± 0.07, n = 5 pairs, Fig 3.10). These data demonstrate that cycle-by-cycle fluctuations in the amplitude of excitatory and inhibitory currents are not cell specific but common across the population.

When the same approach was used to simultaneously record EPSCs and IPSCs (Fig 3.2C, by holding one of the pyramidal cells at the reversal potential for IPSCs and the other at the reversal potential for EPSCs) we were surprised to find that excitation and inhibition were exquisitely balanced during each cycle. That is, the amplitude of excitatory and inhibitory synaptic conductances (gE and gI, respectively), recorded simultaneously in two pyramidal cells, varied over an order of magnitude from cycle to cycle (e.g. gE: 0.5-8 nS; gI: 2-25 nS) yet strikingly remained proportional (r = 0.63 ± 0.04, slope = 5 ± 0.6, n = 8 pairs Fig 3.2E). Thus, independent of the amplitude changes, each excitatory synaptic event was almost instantaneously (Fig 3.2D, excitation led inhibition by 2.3 ± 0.3 ms, n = 8 cells; Fisahn et al., 1998) counterbalanced by an approximately five times larger inhibitory synaptic conductance (Fig 3.2E and 3.9C).

These results show that cycle-to-cycle fluctuations in the amplitude of the LFP reflect underlying fluctuations of both excitatory and inhibitory synaptic currents, yet excitation and inhibition remain proportional such that, during each oscillation cycle, inhibition is approximately 4 times larger than excitation.

A Simple Model Predicts the Correlation between Amplitude and Frequency

Can these large cycle-by-cycle fluctuations in synaptic conductances account for the observed changes in interval between gamma events? To test whether the observed relationship between excitation and inhibition may, at least in principle, account for the correlation between oscillation cycle amplitude and frequency we developed a simple model of CA3 recurrent circuitry. Pyramidal cells and inhibitory interneurons were modeled as single-compartment neurons where intrinsic properties were matched to experimental data (Appendix). The population of pyramidal cells was reciprocally connected with itself and with a population of inhibitory neurons using physiologically realistic probabilities of connection (Fig 3.11). When model pyramidal cells were depolarized the network intrinsically exhibited rhythmic oscillations at gamma frequencies (Fig 3.3). We imposed no rhythmic pattern of depolarization; oscillations resulted from intrinsic circuit dynamics as demonstrated by other models (Bartos et al., 2007; Traub et al., 1996; Wang and Buzsáki, 1996). From the point of view of a “voltage clamped” pyramidal cell within the simulated population, EPSCs generated by the spiking of pyramidal cells preceded IPSCs by ~3 ms similar to experimental results. Furthermore, during each oscillation cycle the fraction of spiking inhibitory neurons was proportional to that of pyramidal cells. Thus, the amplitude of the EPSC co-varied with the amplitude of the IPSC on a cycle-by-cycle basis (Fig 3.11B), as observed experimentally.

Importantly, the model captures the correlation between oscillation amplitude and frequency observed during gamma oscillations in vivo and in

vitro. That is, the larger the synaptic currents, the longer the interval to the next cycle, thereby giving rise to instantaneous frequencies ranging from 28 to 75 Hz (IEI ranging from 13 – 40 ms, Fig 3.3B). This variability in inter-event interval was not due to a change in the kinetics of synaptic conductance since in the model, as in the experiment, the kinetics of both excitatory and inhibitory synaptic currents remained constant despite large changes in the amplitude (Fig 3.12). Rather, larger inhibitory currents produced a more pronounced hyperpolarization of the modeled membrane potential. As a consequence the time required for the membrane potential to recover to the mean potential is increased and the start of the new oscillation cycle delayed accordingly (Fig 3.3C, D). Thus, the model suggests that network-wide fluctuations in the amplitude of inhibition impose a variable delay to the onset of the subsequent cycle.

To test whether, as predicted by the model, recovery from hyperpolarization is prolonged after large oscillations as compared to small ones, we recorded from CA3 pyramidal neurons in the current-clamp configuration while simultaneously monitoring oscillations with an LFP electrode placed in the stratum radiatum (Fig 3.4). Pyramidal neurons were systematically more hyperpolarized after larger amplitude oscillation cycles than smaller ones, as illustrated by the significant correlation between oscillation amplitude and membrane hyperpolarization ($r = 0.47 \pm 0.04$, $n = 11$ cells; Fig 3.4B). Furthermore, a significantly longer time was required for the membrane

potential to recover to the mean potential after large oscillations as compared to small ones (Fig 3.4B, C).

Can the entire range of oscillation intervals observed in the LFP be accounted for by changes in the time required for pyramidal cells to recover to their mean membrane potential after each oscillation cycle? To address this question we plotted the inter-event interval recorded in the LFP against the recovery time and fit the relationship with a linear function (Fig 3.4C). A slope of 1 implies that the recovery time of the membrane potential spans the same range as the inter-event interval in the LFP. The slope was not significantly different from unity (mean slope = 1.16; sd = 0.31, n = 11 cells, p = 0.12) indicating that changes in recovery time from hyperpolarization can indeed account for the entire range of oscillation intervals. These results indicate that cycle-by-cycle fluctuations in the amplitude of inhibition are likely to play an important role in setting the interval between consecutive gamma cycles.

Synaptic Activity during Gamma Oscillations In Vivo

To determine whether the amplitude of the IPSC predicts the interval to the next gamma oscillation cycle in vivo, as established in vitro, we performed whole-cell voltage-clamp recording from hippocampal CA3 neurons in anesthetized rats. We simultaneously monitored gamma oscillation with an LFP electrode, the tip of which was placed ~500 μm from the patch electrode, in the stratum radiatum (Fig 3.5). Both excitatory and inhibitory synaptic currents coincided with each gamma oscillation cycle, as illustrated by the coherence of

EPSCs and IPSCs with the LFP in the gamma band and the oscillation triggered average (7/8 cells exhibited significant coherence at gamma frequencies and were included in further analysis; Fig 3.5B, C), consistent with what we observed in vitro (Fig 3.2D and 3.9B). The rise and decay times of excitatory and inhibitory currents during each oscillation cycle were also similar to those recorded in vitro (10-90% rise-time EPSC: 4.7 ± 0.4, IPSC 4.3 ± 0.3; mono-exponential decay EPSC: 9.6 ± 1.1 ms, IPSC: 13.9 ± 3.3 ms, n = 7). The relative amplitudes and timing of EPSCs and IPSCs in oscillating cells also matched in vitro synaptic activity, reported above. Specifically, IPSCs recorded during gamma oscillations in vivo were on average 5 times larger (Fig 3.5D, E) and followed EPSCs by approximately 2 ms (Fig 3.5C). Furthermore, both EPSC and IPSC amplitudes varied over a wide range from one cycle to the yet were significantly correlated with the amplitude of the simultaneously recorded LFP ($r = 0.22 \pm 0.04$, and $r = 0.33 \pm 0.02$, respectively, $p < 0.009$ n = 7 cells for excitation and inhibition). We next addressed whether excitation and inhibition underlying gamma oscillations in vivo also fluctuate in a proportional manner. Since whole-cell recordings were made from single cells in vivo, EPSCs and IPSCs could only be recorded sequentially. In order to directly relate the two synaptic currents we made use of the simultaneously recorded LFP oscillation amplitude. That is, we subdivided LFP oscillations in separate bins according to amplitude and, for each bin averaged the simultaneously recorded EPSC or IPSCs (Fig 3.5D). A graph of EPSC amplitudes plotted against IPSC amplitudes, from corresponding bins, illustrates the proportional increase of the

two synaptic currents (Fig 3.5E). These results demonstrate that, despite large fluctuations in their amplitudes, EPSCs and IPSCs on average remain proportional during gamma oscillations in vivo. Finally, as predicted by the model and observed in vitro, the amplitude of the IPSC during each cycle was correlated with the interval to the next gamma cycle, with larger IPSCs predicting longer intervals (Fig 3.5F, $r = 0.31 \pm 0.04$, $p < 0.001$, 6/7 cells; remaining cell, $r = 0.13$ $p < 0.06$).

Discussion

We report that gamma oscillations in the CA3 region of the hippocampus undergo rapid variability in amplitude and that, the amplitude of each oscillation cycle predicts the interval to the next cycle. Consistent with a causal relationship between amplitude and the interval to the next cycle, the amplitude of an oscillation was not a strong predictor of the interval to the previous cycle (Appendix). Using a combination of whole-cell voltage-clamp recordings in vivo and in vitro, we show that synaptic inhibition remains proportional to synaptic excitation during each cycle, despite large cycle-by-cycle fluctuations in the amplitude of excitation. These rapid adjustments in inhibition result in instantaneous changes in the oscillation interval.

Inhibition's Role in Rapidly Changing Oscillation Phase

Inhibition has long been held to play a role in generating fast rhythmic activity (Horowitz, 1972; Leung, 1982; Leung, 1992). Not only do interneurons

participate in these fast oscillations (Buzsaki et al., 1983; Hasenstaub et al., 2005; Tukker et al., 2007) but, experimental and modeling studies have demonstrated that inhibition also plays a critical role in synchronizing neuronal activity (Cobb et al., 1995; Lytton and Sejnowski, 1991), pacing the average oscillation period (Traub et al., 1996; Whittington et al., 1995) and maintaining coherent oscillations (Mann et al., 2005; Van Vreeswijk et al., 1994; Vida et al., 2006; Wang and Rinzel, 1992; Wang and Buzsáki, 1996). Our results indicate that inhibition rapidly modulates the phase or frequency of oscillations on a cycle-to-cycle basis.

We observe that cycle-by-cycle fluctuations in the amount of synaptic inhibition are not specific to individual neurons but, on the contrary, strongly correlate among neighboring pyramidal cells within the CA3 population. The homogeneity of this gamma-modulated inhibition is thus likely to have a strong impact on the excitability of the local population on a moment-to-moment basis. (Because both the spatial coherence of gamma activity and interneuron axonal arbors span only a few hundred microns i.e. local (Glickfeld and Scanziani, 2006; Katzner et al., 2009; Sirota et al., 2008), the correlation between inhibitory synaptic activity, and the correlation between the LFP and synaptic currents is likely to decrease on a similar spatial scale). Indeed, we report that one of the most direct consequences of the ongoing fluctuations in the amount of synaptic inhibition generated at each cycle is the modulation of the interval to the next cycle. We provide a mechanistic explanation for this phenomenon by showing that larger inhibitory conductances produce a correspondingly larger

and longer lasting hyperpolarization of the membrane potential (Fig 3.4). In fact, the time it takes to recover from the hyperpolarization mediated by each cycle of synaptic inhibition not only strongly correlates with the interval to the subsequent cycle but can, in principle, completely account for the duration of the interval. What role could shunting play in modulating the interevent interval? Synaptic conductance decays with a time constant of approximately 15 ms, thus shunting inhibition is likely to play a role in determining the minimal interval between oscillation events (~ 12 ms). Interevent intervals, however, can be as long as 45 ms (average ~ 33 ms). So pyramidal cell excitability during oscillation cycles longer than 15 ms is likely determined by membrane hyperpolarization rather than shunting. These findings do not exclude the possibility that other negative feedback mechanisms, like inhibition of transmitter release via presynaptic glutamate or GABA receptor activation, may also contribute to the observed fluctuations in interevent interval.

Proportional Excitation and Inhibition during Gamma Oscillations

What causes cycle-by-cycle fluctuations in the amount of synaptic inhibition? We observe that during each gamma oscillation cycle, synaptic excitation is almost instantaneously counteracted by inhibition and that the amount of inhibition is proportional to the quantity of excitation recorded at the soma. Inhibition recorded in vivo is on average 4-5 times larger than excitation at the soma (and 3-6 times larger when recorded in vitro, consistent with Oren et al., 2006). Strikingly, this proportionality is maintained on a cycle-by-cycle

basis over a range of synaptic conductances spanning more than one order of magnitude, from less than 1 nS to approximately 10 nS. Thus, the CA3 network is able to maintain a balance between excitation and inhibition despite rapidly changing activity levels.

How is balance over such a wide range achieved? It has been shown that even small changes in the number of active excitatory neurons can directly affect the number of active local inhibitory interneurons (Csicsvari et al., 1998; Kapfer et al., 2007; Miles and Wong, 1984; Silberberg and Markram, 2007). Thus inhibition during each oscillation cycle is likely to be recruited by recurrent excitation in proportion to the number of active excitatory neurons thereby providing a rapid balance in each cycle. In fact, we find that even a simple model of a local recurrent network, with realistic anatomical and physiological parameters and random connectivity between pyramidal cells and interneurons, results in a proportional activation of excitatory and inhibitory conductances over a relatively wide range.

Consistent with the idea that recurrent networks balance excitation with inhibition, proportional changes in these two conductances have also been observed in the neocortex during non-rhythmic spontaneous activity (Okun and Lampl, 2008), high conductance states (Haider et al., 2006) and sensory evoked activity (Anderson et al., 2000; Wehr and Zador, 2003). Because both somatic and dendritic targeting interneurons participate in gamma oscillations (Bartos et al., 2007; Hajos et al., 2004; Hasenstaub et al., 2005; Mann et al.,

2005; Tukker et al., 2007), both forms of inhibition may contribute to the observed proportionality.

Given the relatively constant relationship between excitatory and inhibitory conductances, why is the membrane potential of pyramidal cells more hyperpolarized after large amplitude oscillation cycles? One would expect that, despite large cycle-by-cycle fluctuations in synaptic conductances, the balance between excitation and inhibition may maintain the trajectory of a cell's membrane potential relatively constant. The dynamics of these two opposing synaptic currents differ however such that IPSCs occur ~2 ms later and decay slower than EPSCs. These kinetic differences tip the balance towards hyperpolarization during the late phase of each oscillation cycle. These observations underscore the critical role of the fine temporal structure of excitatory and inhibitory events in controlling the membrane potential (Pouille and Scanziani, 2001) and hence the interval between oscillation cycles.

Importantly, although excitatory and inhibitory synaptic activity is proportional on a cycle-by-cycle basis these two opposing synaptic conductances are not perfectly correlated. Similarly, in neighboring neurons despite substantial co-variation of inhibition (and also of excitation) cell-to-cell variability remains. Differences in connectivity between pyramidal cells and interneurons as well as stochastic synaptic properties such as probability of release are likely to contribute to this variability. This cycle-by-cycle and cell-to-cell variability in the relative magnitude and timing of excitation and inhibition

must be critical in determining the identity of cells that spike during each oscillation cycle.

So, the hippocampal circuitry tightly links the amplitude of gamma oscillation with instantaneous frequency: ongoing fluctuations in the number of active excitatory neurons are instantaneously counterbalanced by proportional changes in the number of active inhibitory neurons and the resulting inhibition is translated into variability in interevent interval or oscillation phase. The tight link between amplitude and phase is highlighted by the fact that gamma oscillations recorded under conditions ranging from acute slices to awake behaving animals, all show this fundamental relationship. Thus the hippocampal circuit constrains oscillatory dynamics such that the active number of neurons and the frequency are inextricably linked.

Synchronous spiking of neurons is an effective means to transfer information between cortical areas (Bruno and Sakmann, 2006; Womelsdorf et al., 2005). It is believed that oscillations play a role in dynamically modulating synchronous activity to facilitate routing of information across cortical areas in a behaviorally relevant manner (Destexhe and Sejnowski, 2001; Engel et al., 2001; Womelsdorf et al., 2007). That is, distinct groups of oscillating neurons can be phase-locked at specific times and cooperatively drive postsynaptic targets, or be incoherent at other times depending on the nature of sensory stimuli, attentional state and behavior goals. In fact, the coherence between neuronal activity recorded in various sub-regions of the hippocampus undergoes rapid changes during exploratory behavior and spatial tasks (Bragin

et al., 1995; Chrobak and Buzsaki, 1998; Montgomery and Buzsáki, 2007). So it is critical to our understanding of how information is routed across different cortical areas to establish how changes in coherence are regulated. This involves determining both the cellular mechanisms that implement phase shifts within a network and how afferent projections drive these changes. We focused on the former in this study. Our results demonstrate that oscillation phase is determined on a moment-by-moment basis by inhibitory activity. We show that as oscillations fluctuate in amplitude, inhibition is adjusted to be proportional to excitation leading to rapid changes in instantaneous oscillation frequency. It will be important for future studies to identify what mechanisms underlie cycle-to-cycle fluctuations in the amplitude of excitation. Phase shifts generated by these fluctuations, by increasing or decreasing coherence between groups of oscillating neurons, may be crucial in differentially routing information to distinct hippocampal areas.

Experimental Procedures

Surgical Procedures

All animal experiments were performed in strict accordance with the guidelines of the National Institutes of Health and the University of California Institutional Animal Care and Use Committee. In vivo experiments were performed in 6–8 week-old rats anesthetized with urethane (1.8 g/kg), and supplemented with ketamine (0.3 g/kg) and xylazine (0.03 g/kg) delivered i.p. The depth of anesthesia was assessed by toe pinch. Skin incisions were infused with lidocaine. Body temperature was monitored and maintained at 35–37 °C using a heating pad. Animals were head-fixed using Kopf rat adapter and 18o ear-bars mounted on a custom stereotaxic fixture. After removing a section of the temporomandibular muscle a square (~4 mm2) craniotomy was performed. The craniotomy was located 4 mm caudal to the bregma and 7 mm ventrolateral to the sagittal suture along the surface of the skull (i.e. the craniotomy was located on top of the parietal-temporal suture). Two small duratomies were performed using a 30 G needle (<0.5 mm in diameter, one for the extracellular recording electrode and one for the patch pipette), separated by approximately 1 mm along the rostral-caudal axis.

Slice Preparation

Hippocampal slices (400 μm) were prepared from 4-7 week-old Wistar rats and incubated for one hour in an interface chamber at 34°C in oxygenated

artificial cerebrospinal fluid (ACSF) containing (in mM): 119 NaCl, 2.5 KCl, 1.3 Na2HPO4, 1.3 MgCl2, 2.5 CaCl2, 26 NaHCO3, and 11 glucose. The slices were kept at room temperature before being placed in a submerged chamber superfused (6 ml/min in a ~1.5 ml bath) with oxygenated artificial cerebrospinal fluid at 32-34ºC for recordings. Gamma oscillations were induced by bath application of 100-500 nM of kainate (Hájos et al., 2000). In a subset of experiments area CA3 was severed from the dentate and CA1. Under these circumstances rhythmic activity was observed in CA3 but not in the dentate or CA1 indicating that the CA3 network alone is capable of generating gamma oscillations (Bragin et al., 1995; Csicsvari et al., 2003; Fisahn et al., 1998).

Electrophysiology

In vivo recordings: Whole-cell recordings were made with patch pipettes (3-5 MΩ) filled with (in mM): 130 Cs-Methylsulfonate, 3 CsCl, 10 HEPES, 1 EGTA, 10 phosphocreatine, 2 Mg-ATP (7.25 pH; 280-290 mOsm) and 0.2% biocytin. Extracellular recordings were performed using tungsten electrodes (~ 1 MΩ, FHC). Two extracellular electrodes were lowered into the hippocampus. One electrode (rostral duratomy) was inserted perpendicular to the pia and used to locate the CA3 pyramidal cell layer. The other (caudal duratomy) was inserted at a slight angle and advanced into the stratum radiatum such that the tip of the two electrodes, in their final positions, were separated by approximately 500 μm. The electrophysiological signature of area CA3 consisted of robust gamma oscillations in the stratum oriens followed by unit

activity in the pyramidal cell layer at a depth of -2.5 to -2.8 mm from the pial surface. Gamma oscillations reversed sign in the stratum radiatum. After locating the pyramidal cell layer the rostral extracellular electrode was retracted and replaced with a patch pipette. Whole-cell recordings were obtained using the "blind" patch-clamp approach (Cang and Isaacson, 2003; Ferster and Jagadeesh, 1992; Margrie et al., 2002). Post-hoc histology was used to verify that recordings were made in CA3 pyramidal cell layer. Recordings were made at approximately 3.8 mm posterior to the bregma and lateral 4.0 mm to the midline.

In vitro recordings: Whole-cell voltage-clamp recordings were made with patch pipettes (3-5 MΩ) containing (in mM): 130 Cs-Methylsulfonate, 3 CsCl, 10 HEPES, 1 EGTA, 10 phosphocreatine, 2 Mg-ATP (7.25 pH; 280-290 mOsm) and 0.2% biocytin. Whole-cell current-clamp recordings were performed with pipettes (3-5 MΩ) filled with (in mM) 150 K-gluconate, 1.5 MgCl2, 5 HEPES, 1.1 EGTA, 10 phosphocreatine (pH 7.25; 280–290 mOsm) and 0.2% biocytin. Voltages were corrected for the experimentally determined junction potential (9.8 ± 0.2 mV; n = 3). Extracellular recordings were performed with tungsten, ni-chrome electrodes or glass pipettes (containing 1M NaCl) placed in the stratum radiatum of the CA3 region. Whole cell recordings were obtained from visually identified CA3 pyramidal cells using infrared videomicroscopy.

Recordings from Awake Freely-moving Rat

Data Acquisition: Recordings from freely-moving rat were made using tetrodes placed in CA3 as described in Leutgeb et al., 2007. The LFP was recorded in the 1-450 Hz frequency band and digitized at 2 kHz. Data Analysis: LFP was filtered using moving average filter (40 ms window) this procedure removed theta band activity. Data was then analyzed using the methods described in the main text.

Data Acquisition

Whole cell and extracellular recordings, performed in vitro and in vivo anesthetized rats, were carried out using MultiClamp 700B amplifiers and digitized at 20 kHz. Whole-cell recordings were low-pass filtered (2 kHz) and extracellular recordings band-pass filtered (0.1-2 kHz). EPSC were recorded at -87 ± 0.5 mV (n = 12 cells) in vitro and -94 ± 1 mV (n = 12 cells) in vivo. IPSCs were recorded at -1 ± 4 mV (n = 7 cells) in vitro and 22 ± 4 mV (n = 7 cells) in vivo. Excitatory and inhibitory synaptic conductances (gE and gI respectively) were computed assuming that EPSCs were recorded at the reversal potential for inhibition, and that IPSCs were recorded at the reversal potential for excitation. Series resistance, assessed using an instantaneous voltage step in voltage-clamp configuration, was 12 ± 2 MΩ (n = 13 cells) for cells recorded in vitro and 11 ± 2 MΩ (n = 7 cells) in vivo; we compensated for pipette capacitance in cell-attached mode before whole-cell access. When multi-unit recordings were performed in the stratum pyramidale, the sign of the LFP was inverted to be consistent with LFP recorded in the stratum radiatum.

Data Analysis

All analysis was performed with custom routines utilizing Matlab (MathWorks). In order to analyze oscillation events, time periods when the LFP recording exhibited gamma activity were identified. A spectrogram of the broadband recording was constructed from 100 ms windows in 25 ms steps. For analysis we used time periods of at least 100 ms when greater than average power (root mean square) in gamma-band activity was recorded. The extracellular recording was then band-pass filtered (5-100 Hz). Individual oscillation cycles were identified as a peak in the LFP (as illustrated in Fig 3.1). The oscillation cycle amplitude was defined as the peak-to-trough amplitude i.e. the difference between the peak of a given cycle to the subsequent trough of the same cycle (Fig 3.1). The onset of each oscillation event was defined as the time, after the peak, at which the LFP reached 10% of the oscillation cycle amplitude. The interevent interval of oscillation events was computed as the time between the onset of consequent cycles. Events with very low amplitude, less than 0.25 of the standard deviation in oscillation amplitude, were considered to be noise and omitted (these events made up only a small fraction of all events (<5%) when we reanalyzed the data including these events the results were not significantly difference).

The amplitudes of EPSCs and IPSCs during an oscillation cycle were calculated, in a similar manner, i.e. as the difference between the minimum and maximum current within a given cycle (Fig 3.2C, D).

In order to extract multi-unit spiking activity, extracellular recordings were band-pass filtered (0.3-2 kHz), and a threshold applied. A peri-oscillation time histogram (POTH) was then constructed time locked to the onset of gamma oscillation events. The POTH was then fit with a local linear regression (Chronux) in order to extract the full-width at half maximum (FWHM).

Correlation, r, was computed using Pearson's correlation, Spearman's rank correlation yielded quantitatively similar results. All individual r values in the reported averages were highly significant ($p<0.0001$) unless otherwise stated. For further description of correlation methods see Appendix.

The average time course of EPSCs, IPSCs and intracellular membrane potential during an oscillation cycle (i.e. oscillation triggered average) was determined by using a method similar to a spike-triggered average. In this case, however, the average was triggered by the onset of an oscillation cycle recorded in the LFP.

The latency between EPSCs and IPSCs was computed for each individual cell by using the LFP as a time stamp. We used two different approaches to calculate this latency: first, the time lag between the trough (i.e. $dI/dt = 0$) of the oscillation triggered average IPSC and inverted EPSC (Fig 3.2 & 5), and second, the time lag between the peak in the cross-correlation of the LFP-EPSC and LFP-IPSC. Additionally, in paired recordings we also computed the latency between EPSCs and IPSCs simultaneously recorded measured in two different cells. The results of the three methods were not significantly different.

To determine the relationship between sequentially recorded excitatory and inhibitory currents recorded in vivo, we evenly subdivided the LFP oscillations according to amplitude into 8 to 10 separate bins each contained at least 3 cycles (range: 3-220). Within each cell, we compared the amplitudes of EPSCs and IPSCs belonging to the same bin (Fig 3.5D).

Power and coherence spectra as well as confidence intervals were computed using multitapered methods (Mitra and Pesaran, 1999), the Chronux package (NIMH) and custom Matlab routines. All spectral analysis were performed on broadband recordings unless otherwise stated.

Statistical analysis was performed using the t-test and fisher transform where appropriate. Variability reported a standard error of the mean, unless stated to be standard deviation (sd).

Model

The local recurrent CA3 circuit was simulated using a model consisting of 400 pyramidal cells and 80 interneurons. Each cell was modeled as single compartment, integrate-and-fire neuron with the following parameters. Parameters were chosen to match the range of intrinsic properties and synaptic connectivity patterns experimentally observed in the hippocampus. Excitatory and inhibitory synaptic conductances were modeled with instantaneous rise-times and exponential decays (τ = 5 and 8 ms respectively). Stochasticity was included in the model by the probability of release at excitatory synapses (PR = 0.5) and background synaptic activity introduced as Gaussian noise (s.d. = 50

pA). Modeled pyramidal neurons received no extrinsic rhythmic depolarization. Instead neurons' resting potential was near threshold (similar to the experimentally recorded mean resting potential of -51.4 ± 1mV, n = 6 of pyramidal cells in vitro) and spiking activity was initiated by the stochastic background synaptic activity. The resulting rhythmic activity was a result of the network dynamics.

Although not directly imposed, the simple model exhibited several key characteristics of real oscillations in the CA3 network: the network spiked rhythmically at intervals of 28-75 ms, excitation led inhibition by ~3 ms during each oscillation cycle, excitation and inhibition were proportional during each oscillation cycle despite large changes in excitatory conductance and finally the interval between cycles was correlated with the magnitude of inhibitory conductance during the previous cycle.

	PYR	IN	References
Membrane Resistance (MΩ)	60	40	(Glickfeld and Scanziani, 2006)
Capacitance (pF)	100	100	
Prob. of connection to PYR	0.15	0.4	(Sik et al., 1995; Traub et al., 1997)
Prob. of connection to IN	0.4	0.4	
Mean unitary synaptic conductance (nS) onto PYR	0.15	1	(Glickfeld and Scanziani, 2006; Miles, 1990; Miles and Wong, 1986)
Mean unitary synaptic conductance (nS) onto IN	2	1	(Bartos et al., 2002; Glickfeld and Scanziani, 2006)
V_{rest} (mV)	-55	-62	See below
g_I reversal (mV)	-75	-55	(Glickfeld et al., 2009; Vida et al., 2006)
g_E reversal (mV)	0	0	

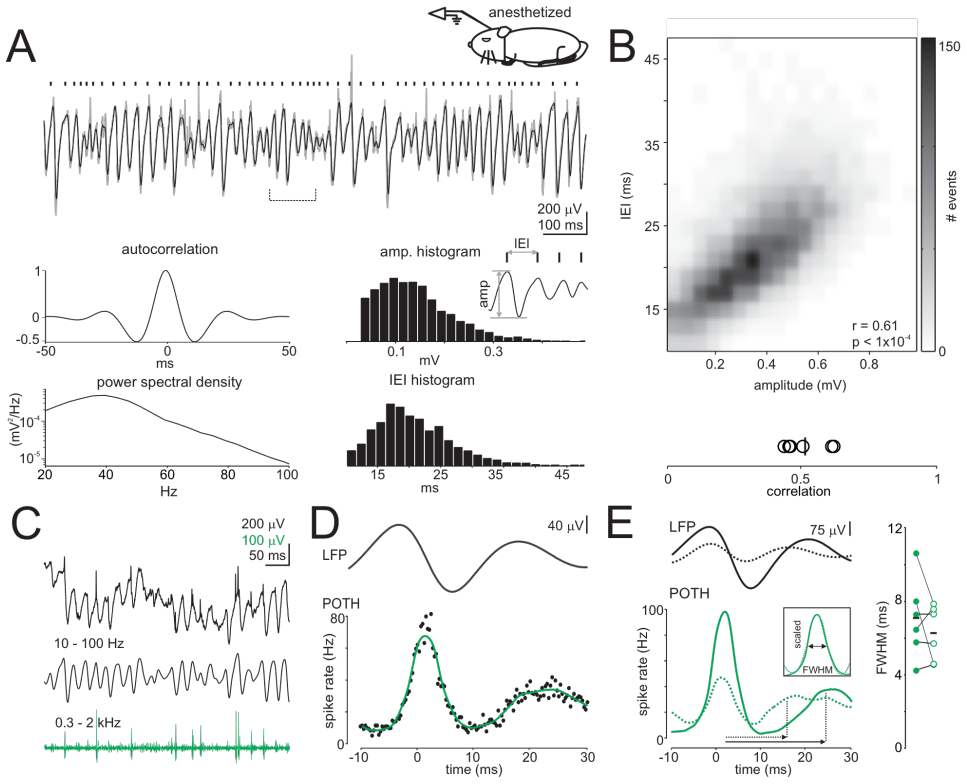

Fig. 3.1 Gamma Oscillation Amplitude Predicts Latency to Next Oscillation Cycle

(A) (Top) Broadband (gray) and gamma-band filtered local field potential (LFP, 5-100 Hz) recorded in the stratum radiatum of area CA3 of an anesthetized rat. Raster plot marks the peak of each oscillation cycle. (Bottom, left) Autocorrelation of LFP and power spectral density of gamma-band LFP. (Bottom, right) Histograms of oscillation amplitude and interevent interval (IEI). (Inset) LFP recording illustrating the measurement of peak-to-peak amplitude and IEI (expansion of the recording marked by a horizontal bracket in the top panel). Positivity is up.

(B) (Top) IEI correlated against amplitude of the previous cycle illustrated in histogram. Note the correlation between oscillation amplitude and IEI. (Bottom) summary of correlations, n = 6 rats. Vertical bar is average.

(C) Broadband extracellular recording (top), gamma-band LFP (middle, 5-100 Hz band-pass), multi-unit spiking (green, 0.2-2 kHz) from stratum pyramidale of area CA3. Negativity is up.

(D) Oscillation triggered average of LFP, peri-oscillation spike-time histogram (POTH), and local linear fit to POTH (green).

(E) (Left) Average LFP and POTH fit calculated separately for large (mean amplitude = 313 μV) and small (99 μV, dotted) oscillation cycles. Arrows illustrate the increased latency between spiking events after large amplitude cycles. (Inset) Small POTH scaled to the peak of the large POTH. (Right) Summary of full-width at half maximum (FWHM) of POTH for large (solid) and small (open) oscillation cycles (n = 6 rats). Averages are illustrated with horizontal bars. Note that spiking occurs in a narrow time-window during each oscillation cycle independent of oscillation amplitude.

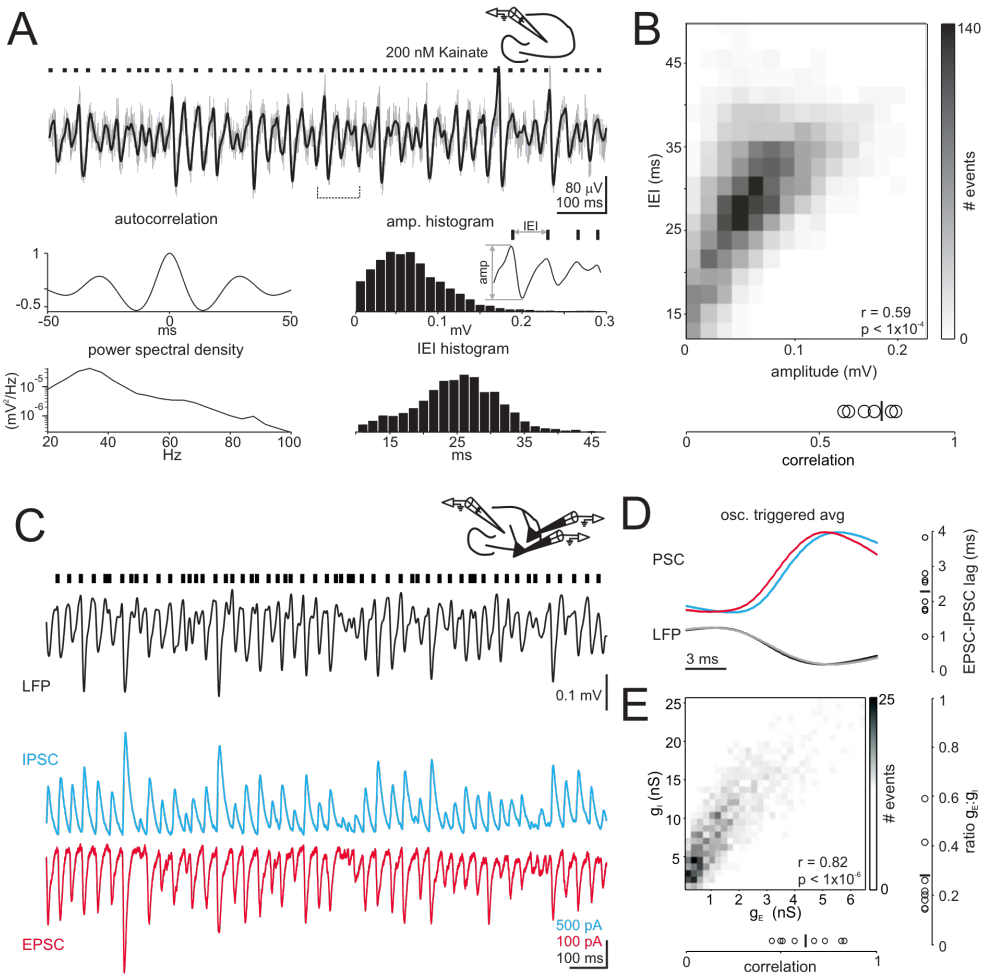

Fig. 3.2 Excitation Instantaneously Balanced by Proportional Inhibition during Each Gamma Oscillation Cycle

(A) (Top) Broadband (gray) and gamma-band filtered (black) LFP recorded in the stratum radiatum of area CA3 in acute hippocampal slice. Raster plot marks the peak of each oscillation cycle. (Bottom, left) Autocorrelation of LFP and power spectral density of gamma-band LFP. (Bottom, right) Histograms of oscillation amplitude and IEI (interevent interval). (Inset) LFP recording illustrating the measurement of peak-to-peak amplitude and IEI (expansion of the recording marked by a horizontal bracket in the top panel). Positivity is up.

(B) (Top) IEI correlated against amplitude of the previous cycle. (Bottom) summary of correlations, n = 6 slices. Vertical bar is the average. Note the correlation between oscillation amplitude and IEI.

(C) Dual patch-clamp recording from two neighboring CA3 pyramidal cells. Oscillations are monitored with an LFP electrode (black, positivity is up). EPSCs (red) and IPSCs (cyan) simultaneously recorded by holding two cells at the reversal potential for inhibition (-3 mV) and excitation (-87 mV) respectively. Note the correlated fluctuations in the amplitude of excitation and inhibition.

(D) (Left) Average time course of EPSC and IPSC (same cell as C) during an oscillation cycle recorded in the LFP i.e. oscillation triggered average. EPSC is inverted for illustration purposes. LFPs recorded simultaneously with EPSCs and IPSCs are shown as black and gray traces respectively. (Right) Summary of EPSC-IPSC lag during an oscillation cycle. Horizontal bar is the average.

(E) (Top) Cycle by cycle correlation between excitatory and inhibitory conductances recorded in the pair shown in C. Summary of correlation between excitation and inhibition (bottom) and ratio of mean excitatory and inhibitory conductances (right) (n = 8 pairs). Vertical and horizontal bars illustrate respective averages.

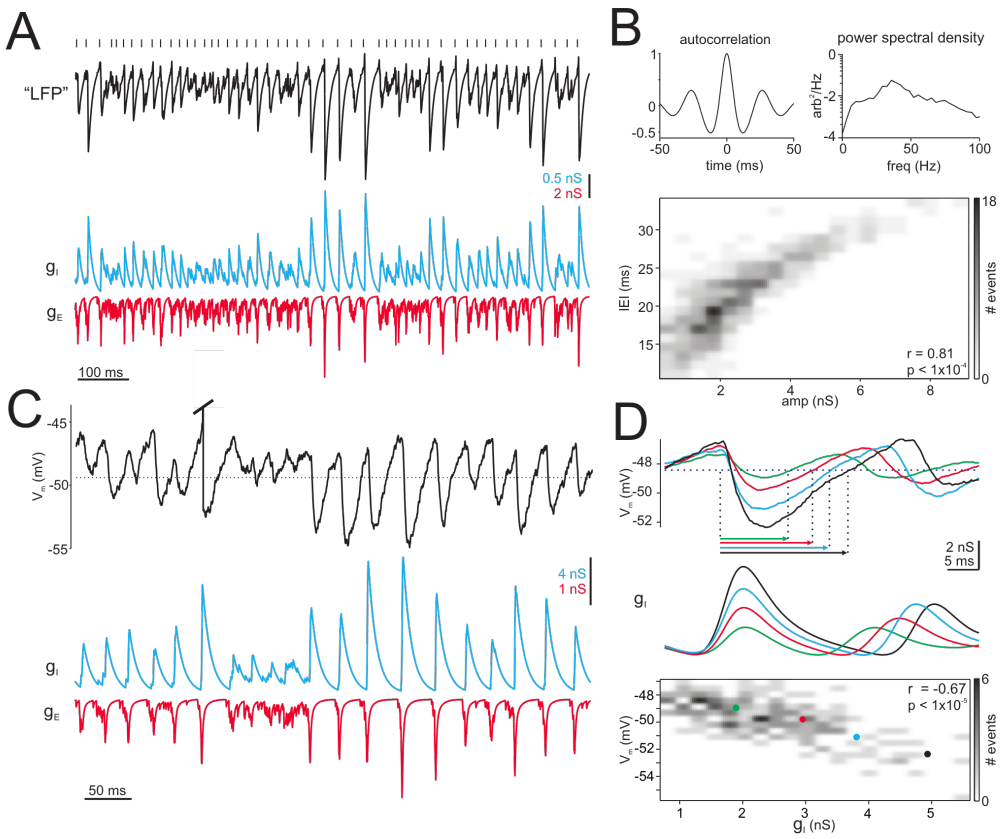

Fig. 3.3 Correlated Amplitude and Frequency in Simple Model of CA3 Circuit

(A) Average excitatory (gE, red) and inhibitory (gI, cyan) synaptic conductance received by model pyramidal cells. LFP (black) is approximated as the sum of the two conductances.

(B) (Top) Autocorrelation and power spectrum of simulated LFP. (Bottom) Interevent interval correlated against amplitude of the previous cycle.

(C) The membrane potential (Vm) of an individual pyramidal cell in modeled circuit (spike truncated), gE (red) and gI (cyan); dotted line illustrates the average Vm.

(D) Oscilllation cycles were binned according to gI amplitude and the oscillation triggered amplitude of Vm computed for each bin (different colors): average time course of gI in four bins of increasing amplitude (middle) and corresponding (color coded) Vm averages (top). The arrows illustrate that it takes longer for Vm to recover to the average potential (horizontal dotted line) after large amplitude cycles. (Bottom) Cycle-by-cycle correlation between Vm hyperpolarization and the gI. Bins in upper panels are illustrated with solid dots of respective colors.

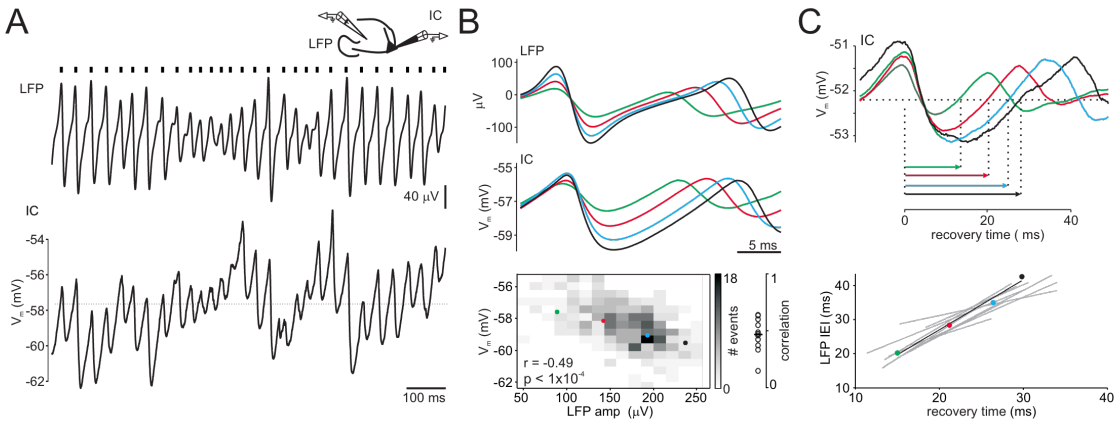

Fig. 3.4 Larger, Longer Hyperpolarization of Pyramidal Cells following Large Amplitude Oscillation Cycles

(A) LFP and simultaneously recorded membrane potential (Vm; whole-cell current clamp configuration: IC) during in vitro gamma oscillations (dotted line is mean Vm). Positivity is up.

(B) Oscillation cycles were binned according to LFP amplitude and the oscillation triggered average (OTA) of Vm computed for each bin (different colors): average time course of LFP in four bins of increasing amplitude (top) and corresponding (color coded) Vm averages (middle). Note that Vm undergoes larger and longer hyperpolarization during large amplitude oscillation cycles. (Bottom, left) Cycle-by-cycle correlation between the peak hyperpolarization and LFP amplitude. Bins in upper panels are illustrated with solid dots of respective colors. (Bottom, right) summary of correlation (n = 11 cells).

(C) (Top) Oscillation cycles were binned according to LFP interevent interval and the OTA of membrane potential computed for each bin (different cell than A and B). Arrows illustrate “recovery time”, i.e. time from onset of oscillation cycle till membrane potential recovers to mean Vm (horizontal dotted line). (Bottom) LFP interevent interval plotted as a function of Vm recovery time. Colored dots and black line correspond to the above cell, other cells shown in grey. Note, mean slope, m = 1.16; sd = 0.3, suggesting that changes in the time for recovery from hyperpolarization in individual cells can account for the entire range of oscillation intervals observed in the LFP.

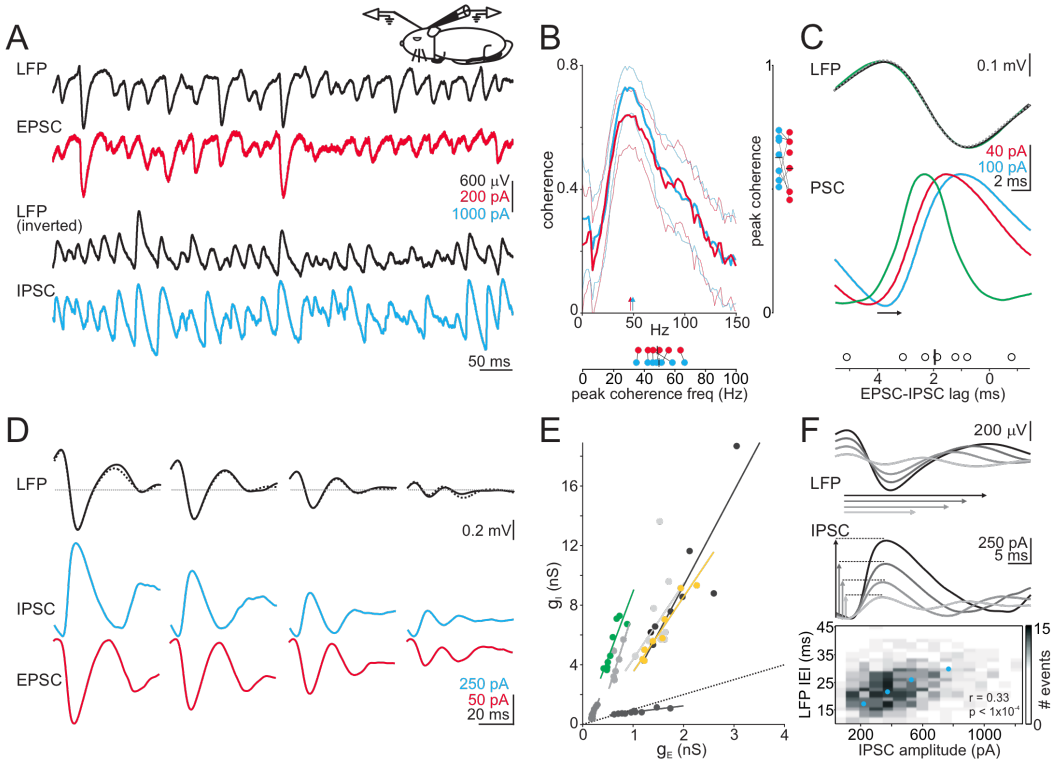

Fig. 3.5 Excitation Balanced by Proportional Inhibition during Gamma Oscillations In Vivo

(A) Whole-cell recording of EPSCs in CA3 cell (red) and simultaneously recorded LFP (black, positivity is up) during gamma oscillations in anesthetized rat. IPSCs (cyan) and inverted LFP recorded from the same cell. Note correlated fluctuations in the amplitude of LFP and synaptic currents.

(B) Coherence between LFP and IPSCs (cyan) or EPSC (red); jack-knifed 95% confidence interval (thin lines); arrows mark peak coherence frequencies. Summary of peak coherence frequency (bottom) and peak coherence (right). Average shown as a vertical or horizontal bar (n = 7 cells).

(C) Oscillation triggered average (OTA) of EPSC (red), IPSC (cyan) and LFP. LFP was recorded simultaneously with EPSCs, IPSC (black and dotted traces respectively). EPSC is inverted for illustration purposes. Overlaid POTH (green, data from Fig 3.1D, aligned to the LFP also in green) illustrates spike timing during oscillation cycle. Note that maximal spiking precedes peak of inhibition. (Bottom) Summary of EPSC-IPSC lag during an oscillation cycle; vertical bar is average.

(D) OTA of EPSCs (red), IPSCs (cyan) computed for four different bins of LFP oscillation amplitude (black; dotted and solid traces were recorded simultaneously with IPSC and EPSCs respectively, same cell as A-C).

(E) Summary of correlation between average inhibitory (gI) and excitatory (gE) conductance in vivo; individual cells are each represented by a different color linear regression. Note, although excitation and inhibition are proportional, the inhibitory conductance is approximately 5 times larger (dotted line is at unity).

(F) OTA of IPSC (middle) computed for four different bins of LFP oscillation interevent interval (top). Vertical arrows illustrate IPSC amplitude and horizontal arrows the correlated changes in the time to the next oscillation event (IEI). (Bottom) IPSC amplitude during an oscillation event correlated with the time to the next oscillation in the LFP (IEI); blue dots correspond to the four OTA shown above.

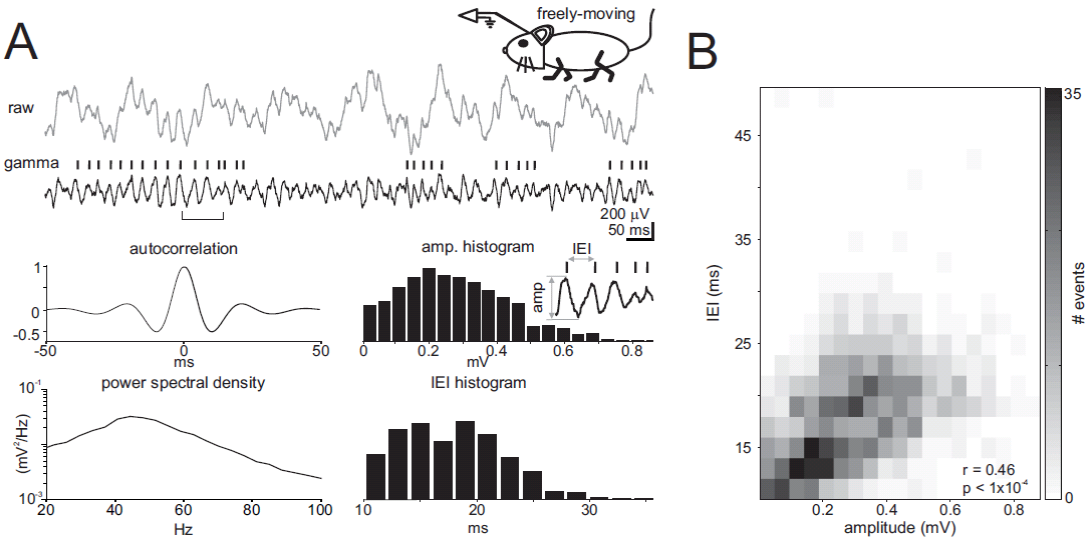

Fig. 3.6 Gamma Oscillation Amplitude Predicts Latency of Next Oscillation Cycle in Awake Freely-moving Rat

(A) (Top) broadband and gamma-band local field potential (LFP, 5-100Hz) recorded in area CA3 of freely moving rat. These data were recorded by S. Leutgeb and D. Schwindel. Raster-plot marks the peak of each oscillation cycle. (Bottom, left) Autocorrelation of LFP and power spectral density of gamma-band LFP. (Bottom, middle) Histograms of oscillation amplitude and IEI. (Inset) LFP (from top panel; time window marked by horizontal bracket) on expanded time-scale to illustrate the measurement of peak-to-peak amplitude and IEI. Positivity is down.

(B) IEI correlated against amplitude of the previous cycle illustrated in 2D histogram. Note the correlation between oscillation amplitude and IEI.

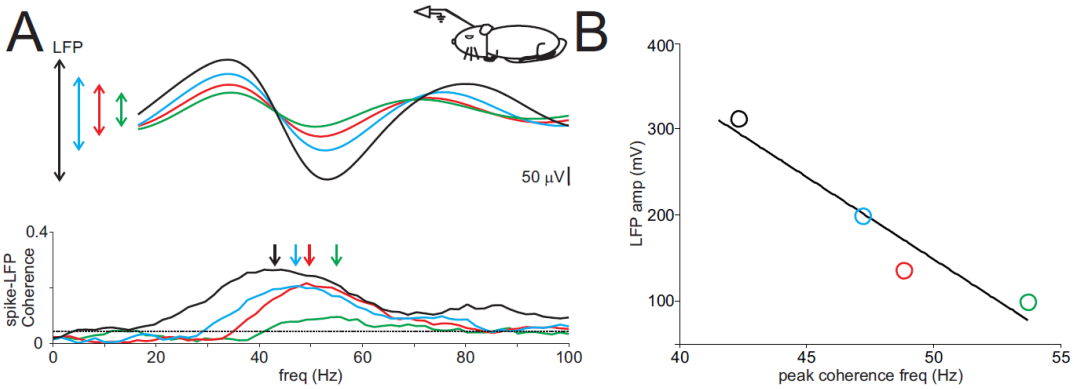

Fig. 3.7 Timing of CA3 Spike Output Covaries with Gamma Oscillation Frequency

(A) Oscillations recorded in the LFP were separated into 4 bins according to amplitude. (Top) The average time course of the LFP oscillation cycles in each bin. (Bottom) Coherence between multi-unit activity and LFP (individually computed for each bin). Arrows illustrate peak coherence frequencies. Coherence is significant at $p > 0.05$ above the dotted horizontal line. Positivity is up.

(B) LFP amplitude vs. peak coherence frequency. Note peak coherence frequency increases as oscillation amplitude decreases.

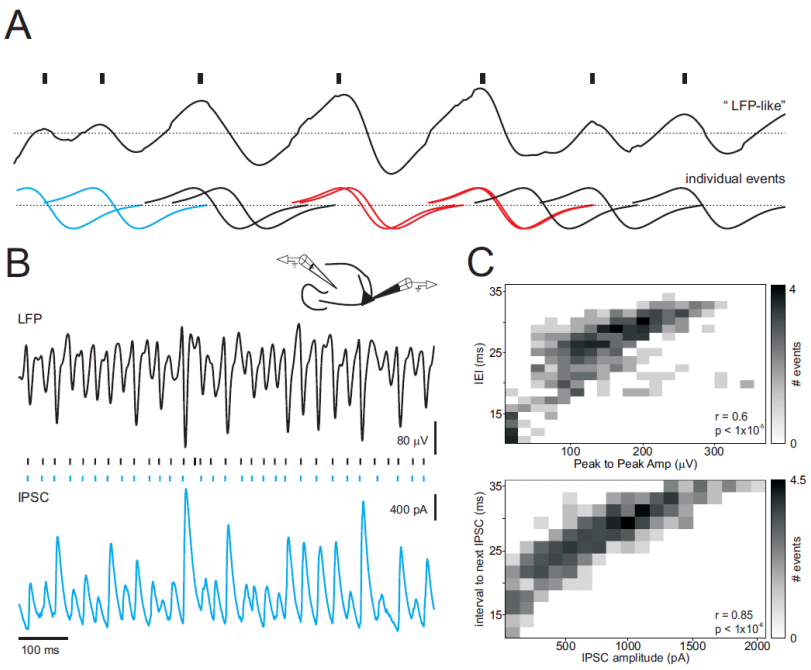

Fig. 3.8 Correlation Between the Amplitude and Interevent Interval of Intracellularly Recorded Oscillation Cycles

(A) Illustration of an LFP-like waveform (top) generated from the superposition of individual events of identical amplitude (bottom). The LFP-like waveform is the results of events that constructively (red) and destructively (cyan) summate. Raster plot marks the peak of each cycle. In this case, neither the amplitude nor the timing of cycles in the LFP reliably report that of the underlying biphasic events (see Appendix). Note, examining the LFP-like waveform and raster plot, one observes a spurious correlation between oscillation amplitude and interevent interval.
(B) Whole-cell recording of IPSCs (cyan) at the reversal potential for excitation and simultaneously recorded LFP (black). Raster plots mark the peak of each oscillation event either intracellularly (cyan) or in the LFP (black). Note, each LFP events correlate with simultaneous inhibitory events. Positivity is up.
(C) (Top) Correlation between LFP amplitude and interevent interval. (Bottom) correlation between IPSC amplitude and the intracellular interevent interval, i.e. the time interval to the next IPSC.

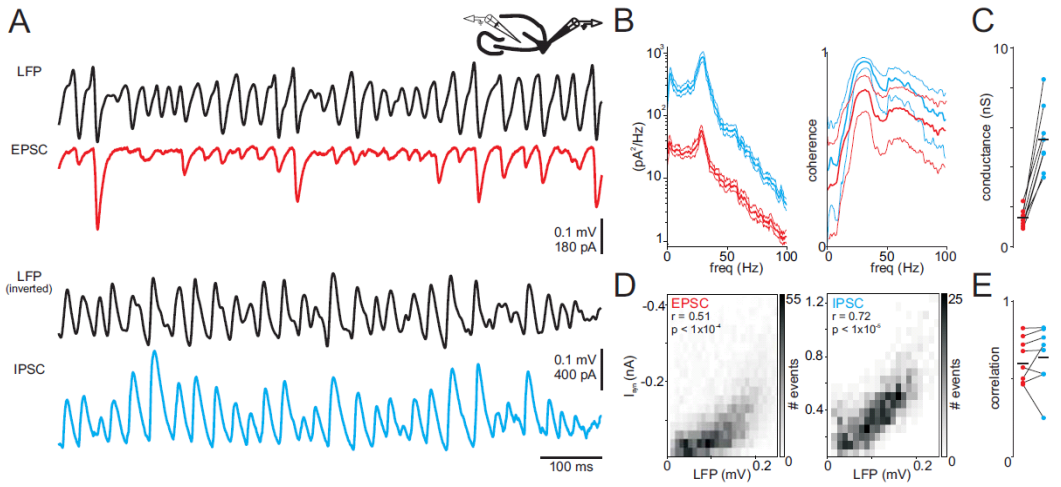

Fig. 3.9 Cycle-by-cycle Fluctuations in Excitatory and Inhibitory Activity Matches Fluctuation in LFP Amplitude

(A) (Top) EPSCs (red) recorded in CA3 pyramidal cell and simultaneous LFP recording. (Bottom) IPSCs (cyan) recorded in same cell and simultaneous LFP recording. Positivity is up.
(B) Power spectra (left) of EPSC and IPSC recordings, and coherence (right) between EPSCs and IPSC and LFP. Thin lines are jack-knifed 95% confidence intervals.
(C) Summary of average excitatory and inhibitory conductance during an individual cycle. Red and cyan dots joined by a line represent conductances recorded in the same cell (n = 8 cells). Notice that inhibition is 3-6 times larger than excitation.
(D) Correlation between LFP amplitude and simultaneously recorded EPSC or IPSC (computed for each oscillation cycle).
(E) Summary of correlation between LFP and EPSC or IPSC (n = 8 cells).

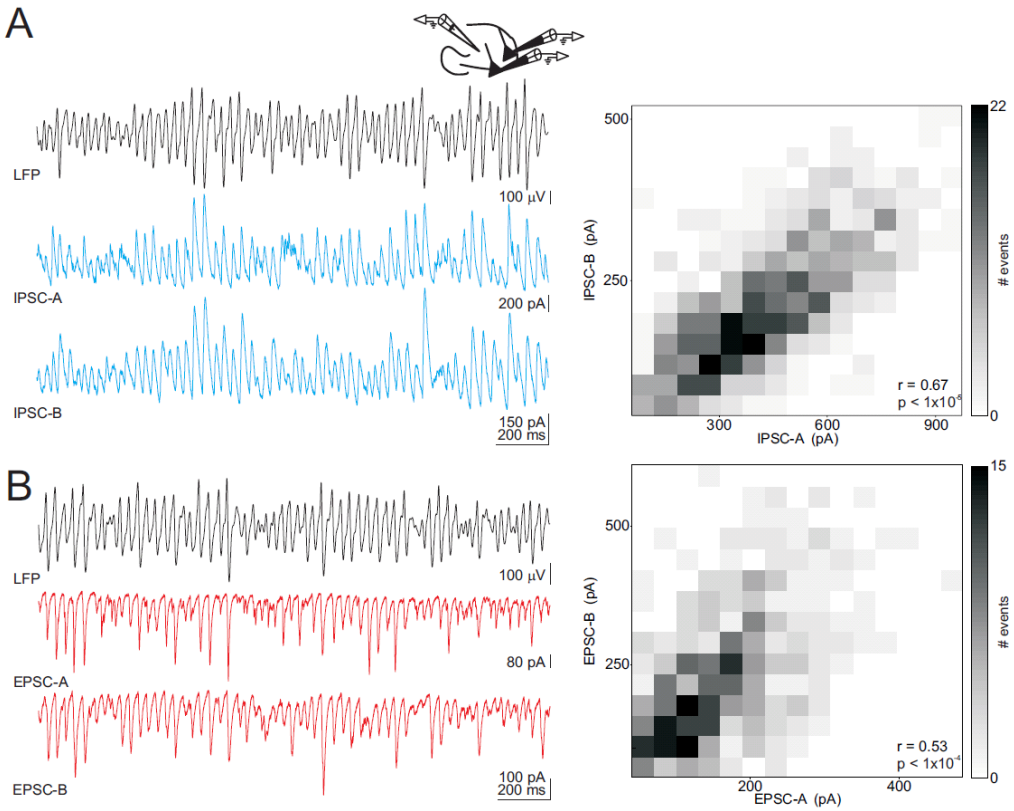

Fig. 3.10 Shared Fluctuations of EPSCs and IPSCs within CA3 Pyramidal Cell Population

(A) (Left) LFP and IPSCs simultaneously recorded in two CA3 pyramidal cells. (Right) 2D histogram illustrating the cycle-by-cycle correlation of the IPSC amplitudes recorded in the two cells.
(B) (Left) Simultaneous recording of LFP and EPSCs in same cells. (Right) 2D histogram illustrating the cycle-by-cycle correlation of the EPSC amplitudes recorded in the two cells. Positivity is up.

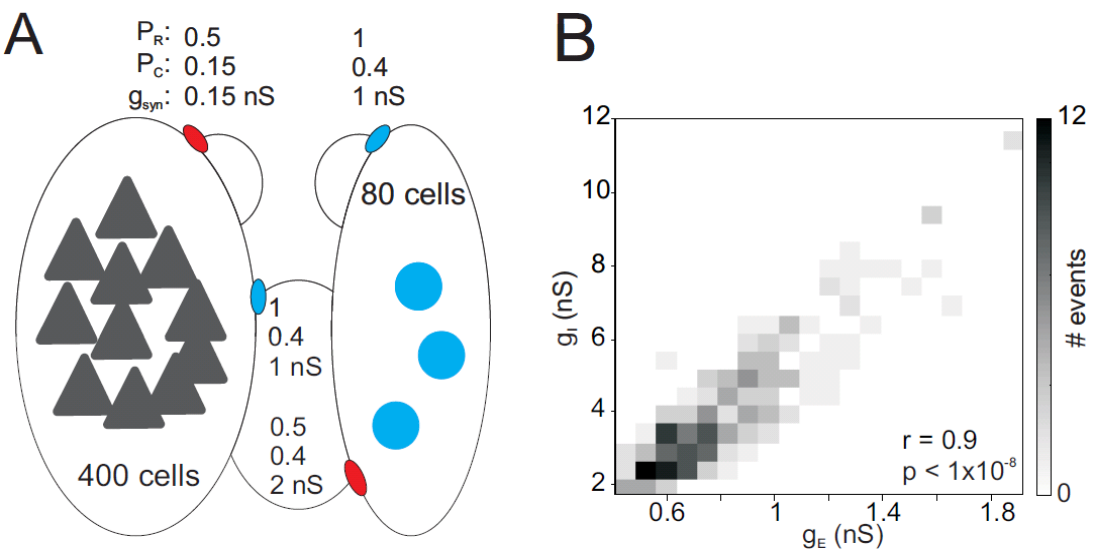

Fig. 3.11 Balanced Excitation and Inhibition in Model of CA3

(A) Schematic illustrating the synaptic properties of the modeled circuit: probability of release (P_R), probability of connection (P_C), average conductance (g_{syn}).

(B) Correlation between the amplitude of excitatory and inhibitory synaptic conductances during each oscillation cycle.

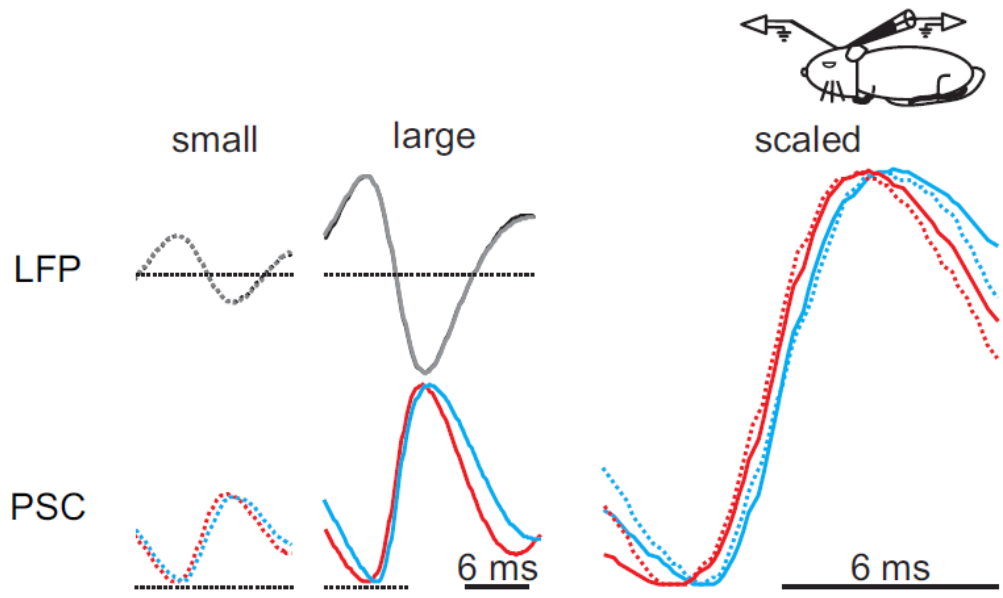

Fig. 3.12 Time-course of Synaptic Currents during Gamma Oscillations In Vivo is Independent of Oscillation Amplitude

(Left) Oscillation triggered average (OTA) of LFP, EPSCs (red, inverted) and IPSCs (cyan) recorded in vivo. (Top) LFP was subdivided into large (right) and small (left) amplitude oscillation cycles (Gray LFP traces recorded simultaneous with IPSCs and black traces with EPSCs; LFP traces are not scaled). (Bottom) OTA of the simultaneously recorded IPSCs and EPSCs (scaled to peak). Note that IPSCs decay slower than EPSCs.

(Right) OTA EPSCs and IPSCs from small (dotted) and large (solid) cycles scaled to peak. Neither EPSC (or IPSC) rise-time, nor EPSC-IPSC lag changes as a function of oscillation amplitude consistent with the spiking data shown in Fig 3.1E. Positivity is up.

Appendix

Correlation between Oscillation Amplitude and Interevent Interval

To test whether the correlation between the amplitude of an oscillation cycle and the latency to the next cycle (R+1) was consistent with a causal link, we assessed the correlation between oscillation amplitude and the latency to the previous cycle (R-1).

We found that this correlation (R-1= 0.27 ± 0.04, n = 12) was substantially weaker than the correlation between the amplitude of event n and the interval to the next event (R+1) for every recording both in vivo and in vitro (data combined). On average R+1 was more than 2 times larger than R-1, and this, in a highly significant manner ($p<5x10-6$).

What could account for the correlation R-1? We have observed that there is a weak correlation between the amplitudes of consecutive events (RAmpli = 0.27 ± 0.05, n = 12). In other words, large amplitude events are more likely to follow large events than smaller ones (and vise versa). This could account some of R-1. In fact, if the amplitude of events n and n-1 are correlated then the amplitude of event n not only predicts the interval to the next event, but also the interval to the preceding event. Indeed, RAmpli accounts for more than 35% of R-1. This was determined by using a partial correlation analysis where the variability in the amplitude of event n (An) and the interval to the previous event (In-1) predicted by the amplitude event n-1 was removed resulting in A'n and I'n-1. The correlation between A'n and I'n-1 was substantially reduced relative to R-1. Importantly, the weak correlation between the amplitudes of

consecutive events (RAmpli) does not confound our finding that the amplitude of event n strongly predicts the interval to the next event (R+1) since the same partial correlation analysis demonstrated a negligible portion of R+1 was accounted for by RAmpli (1.2± 0.8%, n = 12).

In summary we demonstrate that the amplitude of event n correlates significantly better with the interval to event n+1 (R+1) than with the interval to event n-1 (R-1). Furthermore R+1 is not confounded by correlations in the amplitude of consecutive cycles.

Summation of Events within the LFP

Here we address the possibility that the correlation between the amplitude and interevent interval observed in the LFP may be an artifact of superposition, rather than reflecting real changes in the amplitude and timing of neuronal activity. Since the LFP results from the constructive and destructivea superposition of electrical sources and sinks, the LFP could hypothetically result from the superposition of multiple biphasic events of similar peak-to-peak amplitude (Fig 3.8). Depending on their interval, such biphasic events would undergo constructive or destructive summation generating an LFP with events variable apparent amplitude. In this case, however neither the timing nor the amplitude of events in the LFP would reflect the underlying neuronal activity. Accordingly a correlation between the amplitude and interevent interval would not be descriptive of neuronal activity but rather an artifact of superposition.

To address this concern, we using whole-cell configuration to isolate IPSCs by voltage-clamping a CA3 pyramidal cell, in acute slice, at the reversal potential of excitation (Fig 3.8). Because under these conditions there is no driving force for synaptic excitation the recorded synaptic events are purely inhibitory and hence are monophasic. Using this method we found that the amplitude and timing of events observed in the LFP did in fact correspond to that of the recorded synaptic activity. These results confirm that fluctuations in amplitude and interevent interval recorded in the LFP indeed reflect that of the underlying neuronal activity.

What causes the modeled network to generate oscillations that fluctuate in amplitude?

We find that stochasticity, by impacting the number of neurons which synchronously participate in an oscillation cycle, plays a dominant role. Stochasticity in our model takes two forms (i) probability of release (PR) at excitatory synapses, (ii) other sources of stochasticity - represented by a noise current drawn from a Gaussian distribution (with standard deviation x) during each time interval. In fact, the stochasticity caused by probability of release alone (PR = 0.2) in the presence of a negligible amount of current noise (<2 pA) was sufficient to evoke fluctuations in amplitude (almost an order of magnitude) and inter-event interval (instantaneous frequency varied from 28 – 66 Hz). This demonstrates that, at least in our model, sources of “noise” compatible with the

physiological properties of the network can result in oscillations that fluctuate in amplitude and frequency.

Ultimately, however, in the intact CA3 region in vivo external afferents, from the dentate gyrus and the perforant path, are likely to dwarf intrinsic stochasticity as the main cause of amplitude fluctuations. Indeed such external sources are almost certain to play an important role, as gamma coherent oscillation have been observed between hippocampus and entorhinal cortex and CA3 and other hippocampal subfields (Bragin et al., 1995; Chrobak and Buzsaki, 1998; Montgomery and Buzsáki, 2007)

Does the model robustly generate oscillations where changes in amplitude are correlated with interevent interval?

To address this question we independently varied the two forms of stochasticity over approximately two orders of magnitude (x = 1 to 100 pA, PR = 0.05 to 0.9).

At very low levels of stochasticity (x < 2 pA and PR > 0.9) the network exhibits little fluctuations in amplitude (i.e. approximately the same number of neurons participated in each event) and correspondingly little changes in inter-event interval. At very high levels of stochasticity (x > 80 pA or PR < 0.1), on the other hand, synchrony is abolished and the network no longer reliability generated rhythmic activity.

In the vast majority of stochasticity levels (x = 2 pA – 80 pA, PR = 0.1 – 0.9) we found that the model of CA3 generates gamma oscillations that

fluctuate in amplitude and interevent interval. Importantly, not only are there fluctuations, but oscillation amplitude is correlated with interevent interval demonstrating that this correlation is robust to a wide range of different noise levels and probabilities of transmitter release. We conclude that the model robustly generates oscillations where fluctuations in amplitude are correlated with interevent interval over a broad range of stochasticity, spanning almost the entire range of PR, and approximately two orders of magnitude in noise current.

Acknowledgements

This chapter is a reprint of the material as it appears in Instantaneous modulation of gamma oscillation frequency by balancing excitation with inhibition. Atallah BV, Scanziani M. Neuron. 2009 May 28;62(4):566-77. The dissertation author was the primary author of this material.

References

1. Anderson, J. S., Carandini, M., and Ferster, D. (2000). Orientation tuning of input conductance, excitation, and inhibition in cat primary visual cortex. J Neurophysiol 84, 909-926

2. Bartos, M., Vida, I., Frotscher, M., Meyer, A., Monyer, H., Geiger, J. R. P., and Jonas, P. (2002). Fast synaptic inhibition promotes synchronized gamma oscillations in hippocampal interneuron networks. PNAS 99, 13222–13227

3. Bartos, M., Vida, I., and Jonas, P. (2007). Synaptic mechanisms of synchronized gamma oscillations in inhibitory interneuron networks. Nat Rev Neurosci 8, 45-56

4. Bragin, A., Jando, G., Nadasdy, Z., Hetke, J., Wise, K., and Buzsaki, G. (1995). Gamma (40-100 Hz) oscillation in the hippocampus of the behaving rat. J Neurosci 15, 47-60.

5. Bruno, R. M., and Sakmann, B. (2006). Cortex is driven by weak but synchronously active thalamocortical synapses. Science (New York, NY) 312, 1622-1627

6. Buzsaki, G. (2006). Rhythms of the Brain.

7. Buzsaki, G., Leung, L. W., and Vanderwolf, C. H. (1983). Cellular bases of hippocampal EEG in the behaving rat. Brain Res 287, 139-171.
8. Cang, J., and Isaacson, J. (2003). In Vivo Whole-Cell Recording of Odor-Evoked Synaptic Transmission in the Rat Olfactory Bulb. J Neurosci 23, 4108-4116

9. Chrobak, J. J., and Buzsaki, G. (1998). Gamma oscillations in the entorhinal cortex of the freely behaving rat. J Neurosci 18, 388-398.

10. Cobb, S. R., Buhl, E. H., Halasy, K., Paulsen, O., and Somogyi, P. (1995). Synchronization of neuronal activity in hippocampus by individual GABAergic interneurons. Nature 378, 75-78

11. Csicsvari, J., Hirase, H., Czurko, A., and Buzsaki, G. (1998). Reliability and state dependence of pyramidal cell-interneuron synapses in the hippocampus: an ensemble approach in the behaving rat. Neuron 21, 179-189.

12. Csicsvari, J., Jamieson, B., Wise, K. D., and Buzsaki, G. (2003). Mechanisms of gamma oscillations in the hippocampus of the behaving rat. Neuron 37, 311-322

13. Destexhe, A., and Sejnowski, T. J. (2001). Thalamocortical Assemblies

14. Engel, A. K., Fries, P., and Singer, W. (2001). Dynamic predictions: oscillations and synchrony in top-down processing. Nature Rev. Neurosci. 2, 704-716

15. Fell, J., Klaver, P., Lehnertz, K., Grunwald, T., Schaller, C., Elger, C. E., and Fernandez, G. (2001). Human memory formation is accompanied by rhinal-hippocampal coupling and decoupling. Nat Neurosci 4, 1259-1264

16. Ferster, D., and Jagadeesh, B. (1992). EPSP-IPSP interactions in cat visual cortex studied with in vivo whole-cell patch recording. J Neurosci 12, 1262-1274

17. Fisahn, A., Pike, F. G., Buhl, E. H., and Paulsen, O. (1998). Cholinergic induction of network oscillations at 40 Hz in the hippocampus in vitro. Nature 394, 186-189

18. Fries, P., Reynolds, J. H., Rorie, A. E., and Desimone, R. (2001). Modulation of oscillatory neuronal synchronization by selective visual attention. Science 291, 1560-1563

19. Glickfeld, L. L., Roberts, J. D., Somogyi, P., and Scanziani, M. (2009). Interneurons hyperpolarize pyramidal cells along their entire somatodendritic axis. Nature Neuroscience 12, 21-23

20. Glickfeld, L. L., and Scanziani, M. (2006). Distinct timing in the activity of cannabinoid-sensitive and cannabinoid-insensitive basket cells. Nature neuroscience 9, 807-815.
21. Gray, C., and Singer, W. (1989). Stimulus-Specific Neuronal Oscillations in Orientation Columns of Cat Visual Cortex. PNAS 86, 1698-1702

22. Haider, B., Duque, A., Hasenstaub, A. R., and McCormick, D. A. (2006). Neocortical network activity in vivo is generated through a dynamic balance of excitation and inhibition. J Neurosci 26, 4535-4545

23. Hájos, N., Katona, I., Naiem, S. S., MacKie, K., Ledent, C., Mody, I., and Freund, T. F. (2000). Cannabinoids inhibit hippocampal GABAergic transmission and network oscillations. Euro. J Neurosci 12, 3239-3249

24. Hajos, N., Palhalmi, J., Mann, E. O., Nemeth, B., Paulsen, O., and Freund, T. F. (2004). Spike Timing of Distinct Types of GABAergic Interneuron during Hippocampal Gamma Oscillations In Vitro. J Neurosci 24, 9127-9137

25. Hasenstaub, A., Shu, Y., Haider, B., Kraushaar, U., Duque, A., and McCormick, D. A. (2005). Inhibitory postsynaptic potentials carry synchronized frequency information in active cortical networks. Neuron 47, 423-435

26. Horowitz, J. M. (1972). Evoked activity of single units and neural populations in the hippocampus of the cat. Electroencephalogr Clin Neurophysiol 32, 227-240.

27. Jagadeesh, B., Gray, C. M., and Ferster, D. (1992). Visually evoked oscillations of membrane potential in cells of cat visual cortex. Science (New York, NY) 257, 552-554

28. Jones, M. S., and Barth, D. S. (1997). Sensory-evoked high-frequency (gamma-band) oscillating potentials in somatosensory cortex of the unanesthetized rat. Brain Res 768, 167-176

29. Kapfer, C., Glickfeld, L., Atallah, B., and Scanziani, M. (2007). Supralinear increase of recurrent inhibition during sparse activity in the somatosensory cortex. Nature Neuroscience 10, 743-753

30. Katzner, S., Nauhaus, I., Benucci, A., Bonin, V., Ringach, D. L., and Carandini, M. (2009). Local origin of field potentials in visual cortex. Neuron 61, 35-41.

31. Leung, L. S. (1982). Nonlinear feedback model of neuronal populations in hippocampal CAl region. J Neurophysiol 47, 845-868.

32. Leung, L. S. (1992). Fast (beta) rhythms in the hippocampus: a review. Hippocampus 2, 93-98.

33. Leutgeb, J. K., Leutgeb, S., Moser, M.-B., and Moser, E. I. (2007). Pattern separation in the dentate gyrus and CA3 of the hippocampus. Science 315, 961-966

34. Lytton, W. W., and Sejnowski, T. J. (1991). Simulations of cortical pyramidal neurons synchronized by inhibitory interneurons. J Neurophysiol 66, 1059-1079

35. Mann, E. O., Suckling, J. M., Hajos, N., Greenfield, S. A., and Paulsen, O. (2005). Perisomatic feedback inhibition underlies cholinergically induced fast network oscillations in the rat hippocampus in vitro. Neuron 45, 105-117

36. Margrie, T. W., Brecht, M., and Sakmann, B. (2002). In vivo, low-resistance, whole-cell recordings from neurons in the anaesthetized and awake mammalian brain. Pflugers Arch 444, 491-498,

37. Martin, C., Beshel, J., and Kay, L. (2007). An Olfacto-Hippocampal Network Is Dynamically Involved in Odor-Discrimination Learning. J Neurophysiol 98, 2196-2205

38. Miles, R. (1990). Variation in strength of inhibitory synapses in the CA3 region of guinea-pig hippocampus in vitro. J. Physiology 431, 659-676

39. Miles, R., and Wong, R. K. (1984). Unitary inhibitory synaptic potentials in the guinea-pig hippocampus in vitro. J Physiol 356, 97-113.

40. Miles, R., and Wong, R. K. (1986). Excitatory synaptic interactions between CA3 neurones in the guinea-pig hippocampus. J. Physiology 373, 397-418

41. Mitra, P. P., and Pesaran, B. (1999). Analysis of Dynamic Brain Imaging Data. Biophys J 76, 691-708

42. Montgomery, S. M., and Buzsáki, G. (2007). Gamma oscillations dynamically couple hippocampal CA3 and CA1 regions during memory task performance. PNAS 104, 14495-14500

43. Neville, K. R., and Haberly, L. B. (2003). Beta and gamma oscillations in the olfactory system of the urethane-anesthetized rat. J Neurophysiol 90, 3921-3930

44. Okun, M., and Lampl, I. (2008). Instantaneous correlation of excitation and inhibition during ongoing and sensory-evoked activities. Nat Neurosci 11, 535-537

45. Oren, I., Mann, E. O., Paulsen, O., and Hajos, N. (2006). Synaptic currents in anatomically identified CA3 neurons during hippocampal gamma oscillations in vitro. J Neurosci 26, 9923-9934.

46. Penttonen, M., Kamondi, A., Acsady, L., and Buzsaki, G. (1998). Gamma Frequency Oscillation in the Hippocampus of the Rat: Intracellular Analysis in Vivo. European Journal of Neuroscience 10, 718-728

47. Pesaran, B., Pezaris, J. S., Sahani, M., Mitra, P. P., and Andersen, R. A. (2002). Temporal structure in neuronal activity during working memory in macaque parietal cortex. Nat Neurosci 5, 805-811

48. Pouille, F., and Scanziani, M. (2001). Enforcement of temporal fidelity in pyramidal cells by somatic feed-forward inhibition. Science (New York, NY) 293, 1159-1163.

49. Schoffelen, J.-M., Oostenveld, R., and Fries, P. (2005). Neuronal Coherence as a Mechanism of Effective Corticospinal Interaction. Science 308, 111-113

50. Sik, A., Penttonen, M., Ylinen, A., and Buzsaki, G. (1995). Hippocampal CA1 interneurons: an in vivo intracellular labeling study. J Neurosci 15, 6651-6665

51. Silberberg, G., and Markram, H. (2007). Disynaptic inhibition between neocortical pyramidal cells mediated by Martinotti cells. Neuron 53, 735-746

52. Sirota, A., Montgomery, S., Fujisawa, S., Isomura, Y., Zugaro, M., and Buzsáki, G. (2008). Entrainment of neocortical neurons and gamma oscillations by the hippocampal theta rhythm. Neuron 60, 683-697

53. Soltesz, I., and Deschênes, M. (1993). Low- and high-frequency membrane potential oscillations during theta activity in CA1 and CA3 pyramidal neurons of the rat hippocampus under ketamine-xylazine anesthesia. J Neurophysiol 70, 97-116.

54. Song, S., Sjöström, P. J., Reigl, M., Nelson, S., and Chklovskii, D. B. (2005). Highly nonrandom features of synaptic connectivity in local cortical circuits. PLoS Biology 3, e68

55. Steriade, M. (2006). Grouping of brain rhythms in corticothalamic systems. Neuroscience 137, 1087-1106

56. Traub, R. D., Jefferys, J. G. R., and Whittington, M. A. (1997). Simulation of Gamma Rhythms in Networks of Interneurons and Pyramidal Cells. Journal of Comp Neurosci 4, 141-150

57. Traub, R. D., Whittington, M. A., Colling, S. B., Buzsaki, G., and Jefferys, J. G. (1996). Analysis of gamma rhythms in the rat hippocampus in vitro and in vivo. J Physiol 493 (Pt 2), 471-484,

58. Tukker, J. J., Fuentealba, P., Hartwich, K., Somogyi, P., and Klausberger, T. (2007). Cell type-specific tuning of hippocampal interneuron firing during gamma oscillations in vivo. J Neurosci 27, 8184-8189

59. Van Vreeswijk, C., Abbott, L. F., and Ermentrout, G. B. (1994). When inhibition not excitation synchronizes neural firing. J Comp. Neurosci. 1, 313-321

60. Vida, I., Bartos, M., and Jonas, P. (2006). Shunting inhibition improves robustness of gamma oscillations in hippocampal interneuron networks by homogenizing firing rates. Neuron 49, 107-117

61. Wang, X., and Rinzel, J. (1992). Alternating and synchronous rhythms in reciprocally inhibitory model neurons. Neural Comp. 4, 84-97.

62. Wang, X. J., and Buzsáki, G. (1996). Gamma oscillation by synaptic inhibition in a hippocampal interneuronal network model. J Neurosci 16, 6402-6413

63. Wehr, M., and Zador, A. (2003). Balanced inhibition underlies tuning and sharpens spike timing in auditory cortex. Nature 426, 442-446

64. Whittington, M. A., Traub, R. D., and Jefferys, J. G. (1995). Synchronized oscillations in interneuron networks driven by metabotropic glutamate receptor activation. Nature 373, 612-615

65. Womelsdorf, T., Fries, P., Mitra, P., and Desimone, R. (2005). Gamma-band synchronization in visual cortex predicts speed of change detection. Nature 439, 733-736.

66. Womelsdorf, T., Schoffelen, J.-M., Oostenveld, R., Singer, W., Desimone, R., Engel, A., and Fries, P. (2007). Modulation of Neuronal Interactions Through Neuronal Synchronization. Science 316, 1609-1612

Chapter 4. The impact of parvalbumin expressing interneurons on visual processing

Abstract

The tuning of cortical neurons to the specific properties of a sensory stimulus is strongly influenced by the neuronal network they are embedded in. While enormous progress has been made in identifying the various different neuron types that make up the cortical network, still very little is known about the specific role that each individual type plays in shaping tuning properties. Here we address the role of parvalbumin (PV) expressing cells, a large class of inhibitory neurons that target the soma and perisomatic compartment of pyramidal cells, in modulating the response of cortical neurons to visual stimuli. By bi-directionally manipulating the activity of PV cells we show that these neurons sharpen orientation tuning, increase direction sensitivity and regulate the contrast response function of pyramidal cells in the primary visual cortex of the mouse. Our result thus provide a causal relationship between the activity of a select neuron type and specific aspects of cortical sensory processing.

Introduction

Cortical pyramidal neurons are inhibited by a variety of GABAergic interneurons each targeting a specific compartment of the pyramidal cell. Among these different interneurons, those that express parvalbumin (PV) (Celio & Heizmann 1981, Celio 1986) represent up to a half (Gonchar & Burkhalter

1997) of the GABAergic interneuron population in the cortex. PV cells are known to inhibit the somatic and perisomatic compartments of pyramidal cells (Kawaguchi & Kubota 1997) and have been shown to be instrumental in controlling temporal fidelity (Pouille & Scanziani 2001), integration time window (Pouille & Scanziani 2001, Gabernet et al 2005), gain (Pouille et al 2009), and high frequency oscillations (Hasenstaub et al., 2005; Tukker et al., 2007; Bartos et al 2007). Despite key involvement in regulating the dynamics of cortical activity, we do not know, how or even whether, PV cells contribute to the tuning of pyramidal cells to sensory inputs. To address this question we have modulated the activity of PV cells in the visual cortex of PV-Cre mice using optogenetic tools and examined the resulting effect on the response of pyramidal cells to visual stimuli.

Results

We ascertained that Cre expressing cells in the PV-Cre line were positive for PV by crossing PV-Cre mice with a td-tomato reporter line and counter-staining the tissue with antibodies against PV. Indeed, PV antibodies exclusively stained td-tomato expressing neurons. Because the aim of our study is to establish the impact of PV cells on cortical visual responses we initially determined the range of stimuli that best activate these cells. Using two photon laser scanning microscopy we performed targeted loose-patch recordings from td-tomato expressing PV cells in layer 2/3 of the primary visual cortex of anesthetized mice (Fig 4.1A). The spontaneous spike rate of PV cells was 2.5

Hz (sd 2 Hz, range = 0 – 6Hz) and their spike-waveforms had faster kinetics than non-PV cells recorded using the same configuration, consistent with these cells being of the fast spiking type. In response to full field drifting gratings of increasing contrast presented to the contro-lateral visual field, PV cells fired at progressively increasing rates that saturated at around 7 Hz (Fig. 4.1 sd 5 Hz, range 2 – 19 Hz) thus representing, on average, an 3 fold increase in rate as compared to their spontaneous firing. In contrast to non-PV cells, PV cells were only moderately tuned to orientations of the grating (Fig. 4.1C, osi for PV: = 0.10 sd 0.06, range = 0.02 – 0.29, n = 46; and non-PV: 0.40 sd 0.25, range = 0.06 – 0.87, n = 41) (6 orientations presented and 12 directions) (Kerlin et al 2010, Sohya et al 2007), and responded to relatively high spatial frequencies (*mean = 0.13 cycles/deg, sd = 0.17 , range = 0.02 – 0.7*), consistent with the physiological profile of fast spiking cells (Niell & Stryker 2008)

To experimentally control the activity of PV cells we selectively expressed into these neurons the light activated microbial opsins Arch-GFP (in order to suppress activity) or ChR2-tdTomato (in order to increase activity) delivered to the primary visual cortex of adult PV-Cre mice via the AAV viral vector.

To determine the impact of Arch-activation on PV cell firing we performed targeted recordings from Arch expressing layer 2/3 PV cells, as described above, at least two weeks after viral injection and illuminated the exposed cortex (see methods) with a fiber coupled LED (473nm, 0.5-10 mW/mm^2 see methods). Photoactivation of Arch significantly reduced both

spontaneous and visually evoked firing of PV cells. We alternated visual stimuli in the presence or absence of cortical illumination to activate Arch and compared the rate and time-course of firing in PV cells in the two conditions. We insured to only moderately reduce the activity of PV cells by using sub-maximal illumination thereby preventing runaway activity of the cortical network. Cortical illumination started before the visual stimulus (to monitor the effect on spontaneous activity) and ended before the end of the visual stimulus (to determine the kinetics of recovery to visually evoked firing rates). Upon illumination, the suppression of firing was rapid as was the recovery at the end of the illumination (<25 ms). On average visually evoked spiking was reduced by 30% from control levels. The sub-maximal illumination reduced the spontaneous firing rate of targeted Arch expressing PV neurons by 1.3 Hz and the visually evoked firing rate by 2.2 Hz (Fig. 4.2 range 0 – 15 Hz).

How does the reduction in PV cell activity impact the processing of visual information in the cortex? To address this question we compared contrast response function, orientation tuning, direction selectivity of layer 2/3 pyramidal cell with or without suppression of Arch expressing PV cells.

Reducing PV-cell activity lead to an increase in the spike rate in pyramidal cells by approximately 100% (Fig. 4.3, 31/34 cells, mean = 0.7 Hz, sd 0.9 Hz, range = 0 – 3 Hz) and this increase occurred at all contrasts. As a result, the contrast response function of pyramidal cells saturated at higher firing rates, clearly indicating that already under control conditions PV cells impose a cap on the output range of pyramidal cells in response to visual stimuli. Importantly, the

increase in spike rate as a fraction of control was not equal for all orientations but instead more pronounced for the non-preferred orientation of the cell. This biased increase in spike rates towards non-preferred stimuli resulted in a significant broadening of the tuning of pyramidal cells (Fig 4.3A,C,G; 23/34 cells, mean decrease in osi = -0.05, range = -0.3 – 0, significance at $p < 0.02$). Similarly, in cells that showed direction selectivity, the increase in spiking rate was more pronounced for the non-preferred direction leading to a significant decrease in direction selectivity (Fig 4.3B,F; 22/34 cells), mean decrease in dsi = -0.11, range = -0.9 – 0.4, significance at $p < 0.03$)

These data demonstrate that even a moderate (~30%) yet specific decrease in the activity of PV cells leads to a significant increase in the output range of pyramidal cells, to a broadening of the orientation tuning, and a decrease in direction selectivity. Thus, under control conditions PV cells clearly contribute to several aspects of the response properties of pyramidal cells to visual stimuli.

Over what range can PV cell activity modulate cortical processing of visual information? Having established that a decrease in PV cell activity modulates specific aspects of the response properties of pyramidal cells to visual stimulation, we decided to increase PV cell activity and determine whether these same properties are modulated in the opposite manner.

Targeted recordings from ChR2 expressing PV cells demonstrated that illumination of the exposed cortical area leads to an increase in both

spontaneous and visually evoked firing of these neurons. The firing of PV cells was again precisely linked to the onset offset and intensity of illumination.

In opposition to the suppression of PV cell firing described above, their activation reduced evoked spiking rate of pyramidal cell by 50% (0.5 Hz sd 0.3 Hz, range 0-1 Hz). Importantly, these experiments were performed with sub-maximal illumination to generate only moderate excitation of PV cells, and thus to prevent complete silencing of the cortex.

The fractional reduction in firing rate was more prominent for the non-preferred orientation and the non-preferred direction of the pyramidal cell, leading to a sharpening of the orientation tuning (Fig 4.4D; 7/9 cells; mean increase in osi = 0.04 sd 0.06, range= 0 – 0.12, significance at $p < 0.03$) and an increase in direction specificity (Fig. 4.4C; 7/9 cells; mean increase in dsi = 0.11, sd 0.19, range = -0.27 – 0.4, significance at $p < 0.03$).

These results are the mirror image of the results obtained in response to the suppression of PV cells and, taken together, indicate that by increasing or decreasing their firing, PV cells can modulate several properties of pyramidal cell response to visual stimuli over quite a wide range. Specifically, while suppression of PV cells doubles the firing rate of pyramidal cells, their activation can reduce it to 50% resulting in a 4-fold modulation. Similarly, the orientation tuning can be increased or decreased depending on PV cell activity for a total range spanning 0.1 orientation selective units. Finally, direction selective cells can also shift their preference over range of 0.2 depending on the activation or suppression of PV cells. Importantly, the range of PV cell firing explored here is

well within the physiologically reported range in awake behaving mice (Niell & Stryker 2010); furthermore we limited the explored range at both the upper and lower end to prevent runaway activity and complete silencing of the cortex, respectively.

Discussion

Our results demonstrate that a specific type of interneuron that predominantly inhibits the somatic and peri-somatic compartment of pyramidal cells has a major impact on the response properties of pyramidal cells to visual stimuli. On the one hand its activation sharpens the response of pyramidal cells yet limit their output dynamic range to changing contrasts. On the other hand the, suppression of PV cells leads to a broadening of the tuning of pyramidal cells but to an increase in their dynamic range.

What mechanism underlies the increase in firing rate, the broadening in orientation tuning, and the decrease in orientation selectivity?

While these observations demonstrate that the approach allows us to perturb the spontaneous and sensory evoked firing rate of Arch expressing PV cells in layer 2/3 it does not provide a quantitative estimate of the concomitant reduction in inhibition in pyramidal cells. First of all, a reduction in firing rate of PV cells may not necessarily result in a proportional reduction in PV mediated GABAergic conductances due to short term plasticity at the GABAergic synapse; secondly, not all PV cells within the region of interest express Arch;

and thirdly, because PV cells inhibit each other, the reduction in firing rate of the Arch expressing PV cells may actually lead to an increase in the firing rate of non-Arch expressing PV cells and thus to a minimal decrease in inhibition onto pyramidal cells. Furthermore, inactivation of PV cells will also result in an increase in excitation. This results from the fact that cortical pyramidal cells excite and receive excitation from other local pyramidal cells; thus, an increase in firing rate of pyramidal cells in response to PV cell suppression (as observed above) will inevitably lead to an increase in the amount of excitation received by the pyramidal cells themselves.

Further experiments using techniques such as whole-cell voltage clamp will be necessary to directly measure how the activation and suppression of PV cells impacts excitatory and inhibitory synaptic input received by pyramidal cells. These data combined with modeling how these synaptic inputs are integrated to produces spiking will enable us to dissect the subthreshold mechanisms that underlie the changes in pyramidal neuron selectivity.

Independent on the specific mechanism, however, our results illustrate the potential PV neurons have for impacting sensory processing. The known sensitivity of PV neurons to neuromodulators makes them ideal circuit elements to control response properties of pyramidal cells depending on the state of the animal.

Experimental Procedures

Virus Injection

Adult PV-Cre or PV-Cre x tdTomato reporter line mice were anesthetized with 2% isoflorane. Then <1 mm^2 area of skull over V1 (2mm lateral to the midline, 0.2mm rostral of lambda) was thinned and 0.1-0.4mm^2 craniotomy performed with a 20G needle. Virus delivered using a glass micropipette attached to either a Nanoject II (Drummond) or UMP3 (WPI). A 100-250nL of virus (Addgene 18917) (AAV2/1.CAGGS.flex.ChR2.tdTomato.SV40 or AAV2/9.flex.CBA.Arch-GFP.W.SV40 (Addgene 22222) was injected at a depth of 300-600um from the cortical surface over 10minutes. The scalp was sutured and analgesic administered (0.1 mg/kg Buprenex).

In a subset of experiments AAV2/1.CAGGS.flex.ChR2.tdTomato.SV40 was injected in P0-P1 pups. Pups were anesthetized under using a cold pad (0 degress). A beveled glass micropipette, tip 40-60um, was then used to puncture the transparent scalp and skull and a bolus of 3x bolus of 20nL injected at 200 and 400um below the surface of the scalp. No differences in visual physiology were observed between adult and pup injected animals.

In vivo physiology

All procedures were conducted in accordance with the National Institutes of Health guidelines and with the approval of the Committee on Animal Care at UCSD. Recordings were made from mice 2-8 months of age, at least 2 weeks after virus injection. Animals were injected with 5mg/kg chlorprothixene and

1.5g/kg urethane. When the mouse reached a surgical plane of anesthesia (10-20minutes), the animal was secured with a stereotaxic bite bar, eye-lash hairs were cut, and a thin, uniform layer of silicone oil (30,000 centistokes) applied to prevent corneal drying. The scalp was then removed and a head plate attached with dental cement. A ~ 1.5 mm^2 craniotomy performed over primary visual cortex (2mm lateral to the midline, 0.7mm rostral of lambda). Craniotomy was then covered with a thin <1mm layer of 1% agarose and the dura left intact. 2ph imaging was performed with a Sutter MOM, and Coherent Chameleon Laser at 1000-1020nm. Targetted recordings extracellular recordings were performed using 2-4MOhm microelectors filled with 50uM Alexa 488 or Sulfur rhodamine dye in aCSF (142mM NaCl, 5mM KCl, 10mM dextrose, 3.1mM CaCl2 1.3mM MgCl pH 7.4). PV + neurons were targeted based on their exprespressino of tdTomato or eGFP, while pyramidal neurons were targeted using the “shadow-patching” method.

When recordings ended, the animal was sacrificed administering 2.5% isoflorane flowed by decapitation. For histology, mice were intracranially profused with 4% PFA, (0.1M PB buffer). The brain was then extracted and fixed over night in 4 % PFA, rinsed in PBS and sliced (30um) and immunohistology performed.

Visual Stimulation

Stimuli were created using Matlab with Psychophysics Toolbox and displayed with gamma corrected LCD (Dell 30x 40 cm, 75Hz refresh rate)

placed 25cm from the mouse. The preferred spatial frequency (within the range 0.01 and 0.5 cycles/degree) and stimulus size (the while ~75% of neurons preferred fullfield, the remainder fired more robustly when a disc of diameter 7-10 degrees.) was determined for each neuron. Orientation and direction selectivity was then determined using drifting sinusoidal gratings at the preferred spatial frequency, 2-3s duration, temporal frequency 2 Hz, and 12 direction at 100% contrast randomly interleaved. Contrast response curves were determined by presenting the same stimuli at preferred orientations at eight contrast levels logarithmically spanning the range 1% to 100% contrast.

Photostimulation of ChR2 and ARCH

ChR2/ARCH were activated using a 473nm fiber couple LED (1mm diameter, 0.5 NA fiber, Doric lenses) was position approximately 5mm from the cranial window. Trials with and without photo stimulation were interleaved.

Analysis

Spontaneous spike rate was calculated as the average firing rate during a 0.5s period before the presentation of the stimulus. The evoked firing rate was the rate, over the entire stimulus duration, evoked by the preferred grating direction.

Orientation selectivity was calculated as 1- circular variance (Ringach et al 1997). using the average firing rate over the entire duration of the stimulus to

each of the 12 grating directions, Direction selectivity was calculated as (R_{pref} – $R_{pref+180}$)/ (R_{pref} + $R_{pref+180}$).

Contrast response curves were fit with the Naka–Rushton equation (Naka and Rushton, 1966): $R(C) = 1 - g/(1 + (C/C50)^n)$, where *C* is contrast, *g* is the gain, C_{50} is the midsaturation contrast, and *n* is a fitting exponent that describes the shape of the curve.

Statistical significance was determined using the student's t-test.

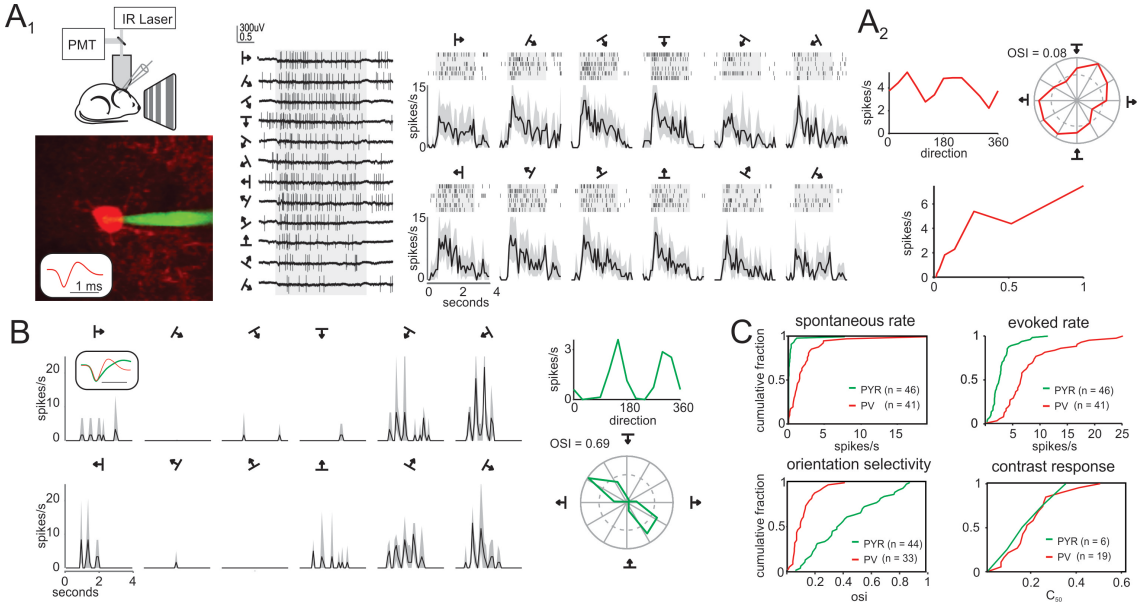

Fig. 4.1 Determining what visual stimuli efficiently activate PV cells

(A_1) Two photon targeted loose-patched recording from PV cell. Inset illustrates PV cell fast spike-waveform. *Middle*, spiking response of cell to each of 12 sine grating directions: raw spike waveforms, and raster-plots and peristimulus time-histograms (PSTH). Gray shaded region denotes PSTH bootstrapped 95% confidence interval.
(A_2) *Top*, same cell's tuning, i.e. average spike rate for 12 grating directions. Illustrated both on cartesian and polar axes, note poor selectivity to orientation. *Bottom*, response to gratings of varying contrasts.
(B) Response properties of non-PV cell illustrated. Note the longer time-course of spike waveform (green) compared to PV cell (red).
(C) Summary of spontaneous and evoked spike rates, orientation selectivity and contrast response function of PV (red) and non-PV (green) cells. Note that PV cells exhibit higher spontaneous and evoked rates, weaker orientation selectivity but similar contrast response C_{50}.

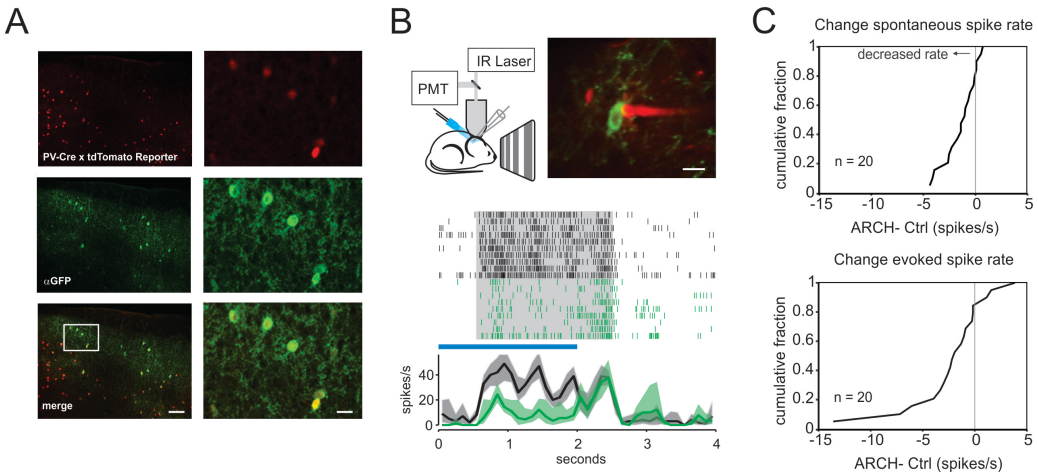

Fig. 4.2 Arch suppresses PV cell spiking

(A) Immunohistology performed on PV-Cre x tdTomato mouse injected with Cre depend Arch-GFP AAV-vector. In red is naive expression of tdTomato in all PV neurons, while in green is the anti-GFP stain. *Right*, detail of same image. Note, all GFP expressing neurons also express tdTomato.

(B) Targeted loose-patch recording from Arch expressing PV cell. Raster plot and PSTH illustrate that visually evoked response of cell is suppressed by blue light. Note rapid recovery of response at offset of blue light.

(C) Summary of Arch suppression spontaneous and stimulus evoked spike rates in n = 20 PV cells.

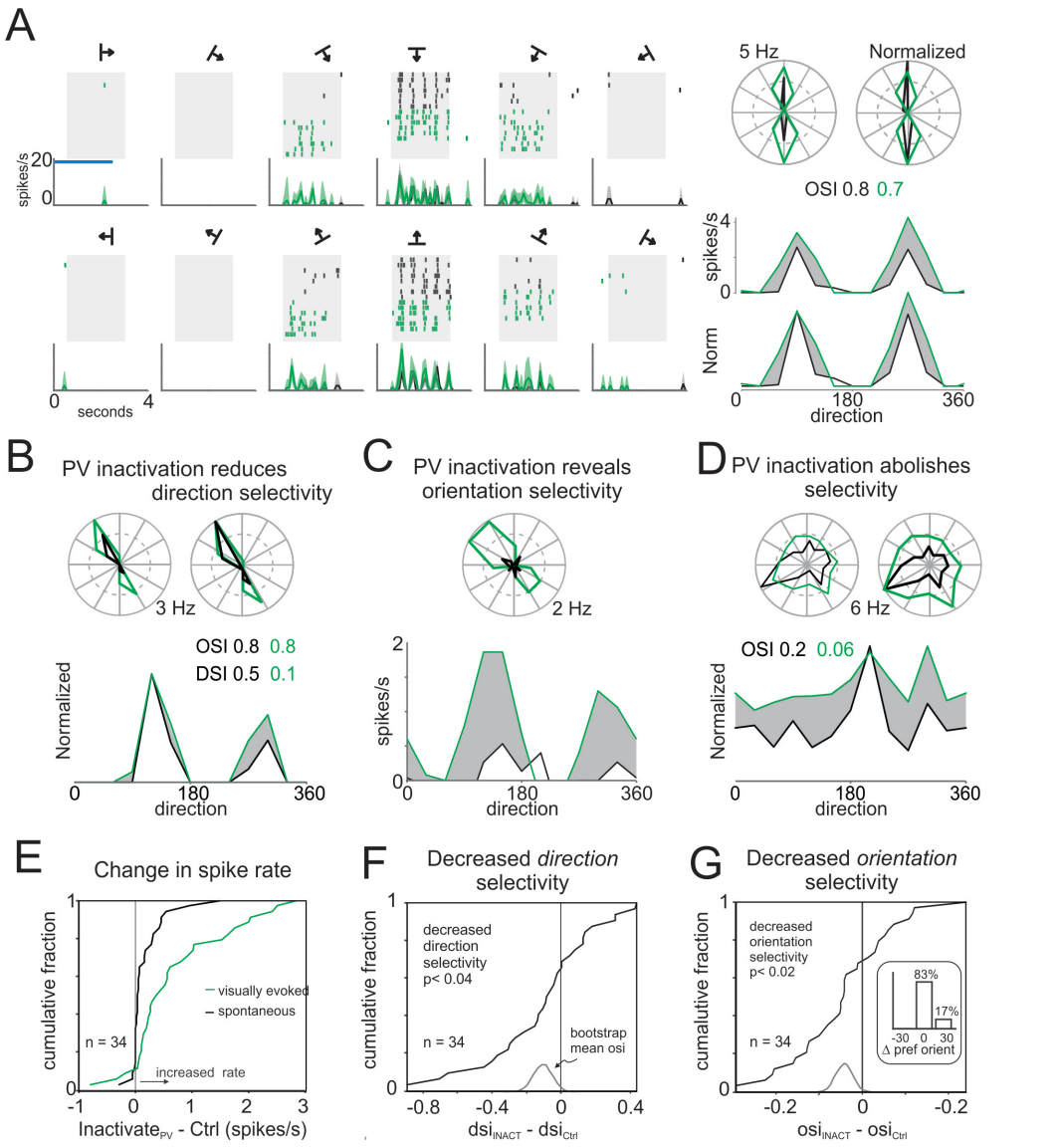

Fig. 4.3 Inactivating PV cells reduces stimulus selectivity in neighboring pyramidal cells

(A) Selectivity of pyramidal cell to gratings during either control (black) or inactivation of PV cells (green). Note increase in response at non-preferred orientations during PV cell inactivation. Polar and Cartesian plots of average stimulus evoked rate. Stimulus selectivity is illustrated by normalizing to the peak response. Shaded region illustrates directions where inactivation disproportionately increased spike rate.

(B) Pyramidal cell where inactivation resulted in decreased direction selectivity

(C) Pyramidal cell that exhibited little-to-no spiking response under control conditions but pronounced, orientation selective response during inactivation.

(D) Pyramidal cell that exhibited orientation selectivity under control conditions but no selectivity when PV cells were inactivated.

(E) Cumulative histogram of change in pyramidal cell spontaneous (black) and visual evoked (green) spike rates (n=34).

(F) Cumulative histogram and bootstrapped mean (grey) of change in direction selectivity between control and inactivation (Arch). Negative values indicated a decrease in selectivity.

(G) Cumulative histogram and bootstrapped mean (grey) of change in orientation selectivity. Inset shows the absolute change in preferred orientation between control and PV inactivation in the subset of cells that had strong (>0.55) orientation selectivity. Note PV inactivation produces less orientation selectivity, but does not rotate a cell's preferred orientation.

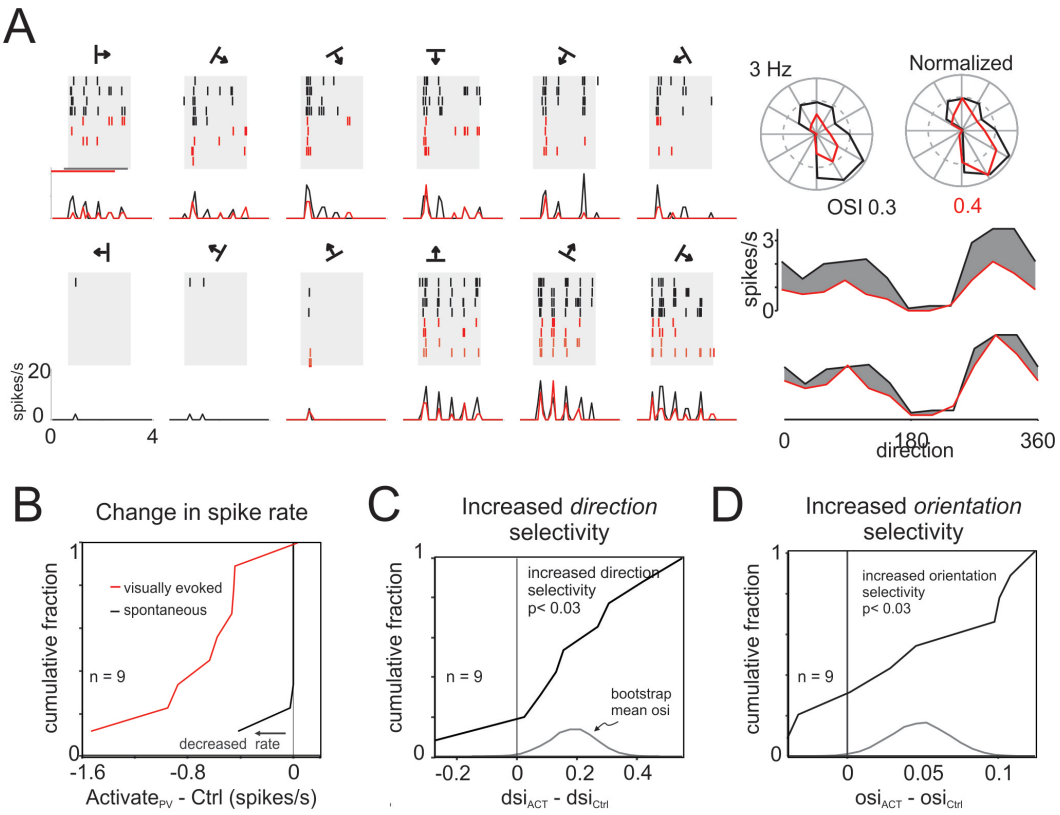

Fig. 4.4 Activating PV cells increases stimulus selectivity in neighboring pyramidal cells

(A) Selectivity of pyramidal cell to gratings during either control (black) or activation of PV cells (green). Note decrease in response at non-preferred orientations during PV cell inactivation. Polar and Cartesian plots of average stimulus evoked rate. Stimulus selectivity is illustrated by normalizing to the peak response. Difference in tuning shown by shaded region.

(B) Cumulative histogram of change in pyramidal cell spontaneous (black) and visual evoked (red) spike rates (n=9). Note the decrease spike rate during PV activation.

(C) Cumulative histogram and bootstrapped mean (grey) of change in direction selectivity between control and PV activation. Positive values indicated an increase in selectivity

(G) Cumulative histogram and bootstrapped mean (grey) of change in orientation selectivity.

Acknowledgements

This chapter consists of material in preparation for publication. All experiments and analysis were performed by B. V. Atallah.

We would like to thank C. Niell for providing his expertise and sharing his code at the initial stages of this project and P. Abelkop for histology.

References

1. Bartos, M., Vida, I., and Jonas, P. (2007). Synaptic mechanisms of synchronized gamma oscillations in inhibitory interneuron networks. Nat Rev Neurosci 8, 45-56

2. Celio M. R. & Heizmann C. W. Calcium-binding protein parvalbumin as a neuronal marker, Nature (1981) 293, 300 – 302

3. Celio M. R. Parvalbumin in most gamma-aminobutyric acid-containing neurons of the rat cerebral cortex, Science (1986) 231, 995-997

4. Gabernet,L.,Jadhav,S.P.,Feldman,D.E.,Carandini,M.&Scanziani,M.Somatosensory integration controlled by dynamic thalamocortical feed-forward inhibition. Neuron 48, 315–327 (2005).

5. Gonchar Y & Burkhalter A, Three distinct families of GABAergic neurons in rat visual cortex. Cereb. Cortex (1997) 7 (4): 347-358

6. Hasenstaub, A., Shu, Y., Haider, B., Kraushaar, U., Duque, A., and McCormick, D. A. (2005). Inhibitory postsynaptic potentials carry synchronized frequency information in active cortical networks. Neuron 47, 423-435

7. Kawaguchi Y & Kubota Y, GABAergic cell subtypes and their synaptic connections in rat frontal cortex. Cereb Cortex. (1997) Sep;7(6):476-86.

8. Kerlin AM, Andermann ML, Berezovskii VK, Reid RC Broadly tuned response properties of diverse inhibitory neuron subtypes in mouse visual cortex. Neuron. 2010 Sep 9;67(5):858-71.

9. Marin-Burgin A, Adesnik H, Atallah BV, Scanziani M. Input normalization by global feedforward inhibition expands cortical dynamic range. Pouille F, Nat Neurosci. 2009 Dec;12(12):1577-85

10. Pouille, F. & Scanziani, M. Routing of spike series by dynamic circuits in the hippocampus. Nature 2004 429, 717–723

11. Tukker, J. J., Fuentealba, P., Hartwich, K., Somogyi, P., and Klausberger, T. Cell type-specific tuning of hippocampal interneuron firing during gamma oscillations in vivo. J Neurosci 2007 27, 8184-8189

12. Niell CM, Stryker MP Highly selective receptive fields in mouse visual cortex. J Neurosci. 2008 Jul 23;28(30):7520-36

13. Niell CM, Stryker MP Modulation of Visual Responses by Behavioral State in Mouse Visual Cortex. Neuron 2010 Feb 25; 65(4):472-9.

14. Ringach DL, Sapiro G, Shapley R A subspace reverse-correlation technique for the study of visual neurons. Vision Res 1997 37:2455–2464

15. Sohya K, Kameyama K, Yanagawa Y, Obata K, Tsumoto T. GABAergic neurons are less selective to stimulus orientation than excitatory neurons in layer II/III of visual cortex, as revealed by in vivo functional Ca2+ imaging in transgenic mice. J Neurosci. 2007 Feb 21;27(8):2145-9.